

Discovery of Novel Material Models Through Symbolic Regression

Entdeckung neuartiger
Materialmodelle mittels symbolischer
Regression

Von der Fakultät für Maschinenwesen der
Rheinisch-Westfälischen Technischen Hochschule
Aachen zur Erlangung des akademischen Grades
eines Doktors der Ingenieurwissenschaften
genehmigte Dissertation

vorgelegt von
Rasul Abdusalamov

Berichter/in: Univ.-Prof. Dr.-Ing. (RUS) Mikhail Itskov
Prof. Dr. Laura De Lorenzis

Tag der mündlichen Prüfung: 14. April 2025

Diese Dissertation ist auf den Internetseiten der Universitätsbibliothek online
verfügbar.

RWTH Aachen University
Lehr- und Forschungsgebiet Kontinuumsmechanik
Eifelschornsteinstr. 18
52062 Aachen, Germany

Bericht Nr. 14 (2025)
ISBN: 978-3-9821703-3-6
D 82 (Diss. RWTH Aachen University, 2025)

Herausgeber:
Univ.-Prof. Dr.-Ing. (RUS) Mikhail Itskov

© Rasul Abdusalamov
Lehr- und Forschungsgebiet Kontinuumsmechanik
RWTH Aachen
Eifelschornsteinstr. 18
52062 Aachen, Germany

All rights reserved. No part of this publication may be reproduced, stored in a retrieval system, or transmitted, in any form or by any means, electronic, mechanical, photocopying, recording or otherwise, without prior written permission of the author.

Printed in Germany.

Abstract

This work presents a comprehensive investigation into the application of symbolic regression for the discovery of novel material models. The introduction provides an overview of the motivation behind this work and a discussion of the current limitations of the state of the art.

The fundamental principles of symbolic regression are presented in detail, including an overview of genetic programming and an explanation of the concept behind the novel method of deep symbolic regression. A continuum mechanical framework is established to provide a foundation for the subsequent analysis. This includes general principles and constitutive equations, as well as practical considerations for the implementation.

Benchmark tests are conducted using both artificial and experimental data to evaluate the performance of various models. These tests include the evaluation of the incompressible generalized Mooney-Rivlin model and nearly incompressible formulations. Moreover, the work is validated on classical data sets, including multi-axial and biaxial loading of vulcanized rubber. Novel interpretable formulations of strain energy functions that are able to characterize experimental data with extreme high accuracy are presented. Furthermore, the work is extended to the evaluation of a temperature-dependent thermoplastic polyester elastomer. A detailed overview of the influences of data set sizes, the benefits of interpretable models, and performance with respect to interpolation and extrapolation capabilities is provided.

Furthermore, the rediscovery of the Mullins effect is explored through the use of artificial data generated by the Ogden-Roxburgh model, with the objective of assessing the capabilities of this approach. Additionally, a temperature-dependent filled silicone data set is analyzed. Extreme sparse data conditions are tested, and the performance of the presented methodology is evaluated.

The approach is extended to microstructural modeling of aerogels. Consequently, novel microstructure-based formulations for the characterization of silica aerogels as an example of aggregated and κ -carrageenan aerogels as an example of open-porous cellular-like microstructures are introduced.

In the final analysis, the impact of hydration effects in polyamide aerogels on material properties are modeled. The work concludes with a summary of the key findings and implications for future research in this domain.

Zusammenfassung

Diese Arbeit stellt eine umfassende Untersuchung der Anwendung der symbolischen Regression für die Entdeckung neuer Materialmodelle dar. Die Einführung gibt einen Überblick über die Motivation für diese Arbeit und eine Diskussion über die derzeitigen Schwächen des gegenwärtigen Forschungsstandes.

Die grundlegenden Prinzipien der symbolischen Regression werden vorgestellt, einschließlich eines Überblicks über die genetische Programmierung und einer Erklärung des Konzepts hinter der neuartigen Methode der tiefen symbolischen Regression. Die nachfolgende Analyse basiert auf der Entwicklung eines kontinuumsmechanischen Konzepts, welches allgemeine Prinzipien, konstitutive Gleichungen sowie praktische Überlegungen zur Implementierung umfasst.

Es werden Referenztests durchgeführt, bei denen sowohl künstliche als auch experimentelle Daten verwendet werden, um die Leistungsfähigkeit zu bewerten. Diese Tests umfassen die Bewertung des inkompressiblen verallgemeinerten Mooney-Rivlin-Modells und nahezu inkompressibler Formulierungen. Darüber hinaus wird die Arbeit an klassischen Datensätzen validiert, einschließlich der multiaxialen und biaxialen Belastung von vulkanisiertem Kautschuk. Es werden neuartige interpretierbare Formulierungen von Dehnungsenergiefunktionen vorgestellt, die in der Lage sind, experimentelle Daten mit extrem hoher Genauigkeit zu charakterisieren. Darüber hinaus wird die Arbeit auf die Auswertung eines temperaturabhängigen thermoplastischen Polyesterelastomers erweitert. Ein detaillierter Überblick über die Einflüsse von Datensatzgrößen, die Vorteile interpretierbarer Modelle und die Leistungsfähigkeit hinsichtlich Interpolations- und Extrapolationseigenschaften wird vorgestellt. Darüber hinaus wird die Wiederentdeckung des Mullins-Effekts durch die Verwendung künstlicher Daten untersucht, die mit dem Ogden-Roxburgh-Modell erzeugt wurden. Zusätzlich wird ein temperaturabhängiger Datensatz von gefülltem Silikon analysiert. Die Leistungsfähigkeit der vorgestellten Methodik wird anhand von extrem kleinen Datensätzen untersucht.

Der Ansatz wird auf die mikrostrukturelle Modellierung von Aerogelen erweitert. Infolgedessen werden mikrostrukturbasierte Formulierungen für Silicat-Aerogelen als Beispiel für aggregierte und κ -carrageenan Aerogelen als Beispiel für offene porige zelluläre Mikrostrukturen vorgestellt.

Schließlich werden die Auswirkungen von Hydratationseffekten in Polyamid-Aerogelen auf die Materialeigenschaften modelliert. Am Ende erfolgt eine Zusammenfassung der wichtigsten Ergebnisse und Schlussfolgerungen.

List of Own Publications

Below is a list of all my publications and conference presentations that I have given during my time at the Department of Continuum Mechanics at RWTH Aachen University.

Articles

Peer-Reviewed Journal Articles

- I. **Abdusalamov, Rasul**, Weise, Jendrik, and Itskov, Mikhail. “Rediscovering the Mullins effect with deep symbolic regression”. In: *International Journal of Plasticity* 179 (2024), p. 104037
 - II. Pandit, Prakul, **Abdusalamov, Rasul**, Itskov, Mikhail, and Rege, Ameya. “Deep reinforcement learning for microstructural optimisation of silica aerogels”. In: *Scientific Reports* 14.1 (2024), p. 1511
 - III. **Abdusalamov, Rasul**, Kaplunov, Julius, and Itskov, Mikhail. “Discovering asymptotic expansions for problems in mechanics using symbolic regression”. In: *Mechanics Research Communications* 133 (2023), p. 104197
 - IV. **Abdusalamov, Rasul**, Hillgärtner, Markus, and Itskov, Mikhail. “Automatic generation of interpretable hyperelastic material models by symbolic regression”. In: *International Journal for Numerical Methods in Engineering* 124.9 (2023), pp. 2093–2104
 - V. **Abdusalamov, Rasul**, Scherdel, Christian, Itskov, Mikhail, Milow, Barbara, Reichenauer, Gudrun, and Rege, Ameya. “Modeling and Simulation of the Aggregation and the Structural and Mechanical Properties of Silica Aerogels”. In: *The Journal of Physical Chemistry B* 125.7 (2021), pp. 1944–1950
 - VI. **Abdusalamov, Rasul**, Pandit, Prakul, Milow, Barbara, Itskov, Mikhail, and Rege, Ameya. “Machine learning-based structure–property predictions in silica aerogels”. In: *Soft Matter* 17 (2021), pp. 7350–7358
-

Conference Proceedings

- I. Xiong, Weibo, **Abdusalamov, Rasul**, and Itskov, Mikhail. “Mesoscopic structure modeling of silica aerogels using cluster-cluster aggregation”. In: *PAMM* (2024)
- II. Xiong, Weibo, **Abdusalamov, Rasul**, Itskov, Mikhail, Milow, Barbara, and Rege, Ameya. “Analysis of the microstructural connectivity and compressive behavior of particle aggregated silica aerogels”. In: *PAMM* (2024)
- III. **Abdusalamov, Rasul**, Itskov, Mikhail, Kaplunov, Julius, and Prikazchikov, Danila. “Adjustment of micro-structure parameters of aggregated structures for dynamic modeling of silica aerogels”. In: *Mechanics of High-Contrast Elastic Solids: Contributions from Euromech Colloquium 626*. Springer, 2023
- IV. Pandit, Prakul, **Abdusalamov, Rasul**, Itskov, Mikhail, Milow, Barbara, and Rege, Ameya. “Data-driven inverse design and optimisation of silica aerogel model networks”. In: *PAMM* 23.1 (2023)
- V. **Abdusalamov, Rasul**, Hillgärtner, Markus, and Itskov, Mikhail. “Hyperelastic material modelling using symbolic regression”. In: *PAMM* 22.1 (2023)
- VI. **Abdusalamov, Rasul**, Pandit, Prakul, Itskov, Mikhail, Milow, Barbara, and Rege, Ameya. “Predictive modeling and simulation of silica aerogels by using aggregation algorithms”. In: *PAMM* 21.1 (2021)
- VII. **Abdusalamov, Rasul**, Itskov, Mikhail, Milow, Barbara, and Rege, Ameya. “Analysis of the fractal properties of silica aerogels using diffusion-limited aggregation”. In: *PAMM* 20.1 (2021)

Conference Presentations

- I. **Abdusalamov, Rasul**, Itskov, Mikhail, Milow, Barbara, Reichenauer, Gudrun, and Rege, Ameya. Investigation of the fractal properties of aerogels by diffusion-limited aggregation models. August 28th – 30th, 2019. *8th GACM Colloquium on Computational Mechanics For Young Scientists From Academia and Industry*.
 - II. **Abdusalamov, Rasul**, Pandit, P., Itskov, M., Milow, Barbara, and Rege, Ameya. Predictive modeling and simulation of silica aerogels by using aggregated structures. March 15th – 19th, 2021. *91st Annual Meeting of the International Association of Applied Mathematics and Mechanics*.
-

- III. **Abdusalamov, Rasul**, Pandit, Prakul, Itskov, Mikhail, Milow, Barbara, and Rege, Ameya. Mechanical and morphological analysis of silica aerogels using a reinforcement learning approach. June 5th – 9th, 2022. *8th European Congress on Computational Methods in Applied Sciences and Engineering*.
 - IV. **Abdusalamov, Rasul**, Hillgärtner, Markus, and Itskov, Mikhail. Automatically Generated Hyperelastic Models Using Symbolic Regression. July 4th – 8th, 2022. *11th European Solid Mechanics Conference*.
 - V. **Abdusalamov, Rasul**, Hillgärtner, Markus, and Itskov, Mikhail. Automatically generated hyperelastic models using symbolic regression. August 15th - 19th, 2022. *92nd Annual Meeting of the International Association of Applied Mathematics and Mechanics*.
 - VI. **Abdusalamov, Rasul**, Hillgärtner, Markus, Chandrasekaran , Rajesh, Vu , Khiêm Ngoc, and Itskov , Mikhail. Advanced material modeling with user subroutines. October 11th – 12th, 2022. *16th LS-DYNA Forum*.
 - VII. **Abdusalamov, Rasul**, and Itskov, Mikhail. Symbolic regression for automated hyperelastic material modelling. March 30th – 31st, 2023. *6th International Conference on Numerical and Symbolic Computation Developments and Applications*.
 - VIII. **Abdusalamov, Rasul**, József, Kalmár, and Itskov, Mikhail. Modeling the Effect of Hydration in Polyamide Aerogels Using Deep Symbolic Regression. May 10th - 12th, 2023. *1st International Seminar on Modelling, Simulation, and Machine Learning for the Rapid Development of Porous Materials*.
 - IX. **Abdusalamov, Rasul**, Kaplunov, Julius, and Itskov, Mikhail. Discovering Asymptotic Expansions of Physical Problems Using Symbolic Regression. May 30th – June 2nd, 2023. *93rd Annual Meeting of the International Association of Applied Mathematics and Mechanics*.
 - X. **Abdusalamov, Rasul**, Chandrasekaran, Rajesh, and Itskov, Mikhail. Microstructural characterization in aerogel modeling through Deep Symbolic Regression. March 4th – 6th, 2024. *2nd International Seminar on Modelling, Simulation, and Machine Learning for the Rapid Development of Porous Materials*.
 - XI. **Abdusalamov, Rasul**, and Itskov, Mikhail. Modeling of Softening Behavior by Deep Symbolic Regression. May 29th – 31st, 2024. *19th European Mechanics of Materials Conference*.
-

- XII. **Abdusalamov, Rasul**, Kaplunov, Julius, and Itskov, Mikhail. Discovery of asymptotic expansions of mechanical problems using symbolic regression. July 21st – 26th, 2024. *16th World Congress on Computational Mechanics and 4th Pan American Congress on Computational Mechanics*.
-

Acknowledgment

I would like to express my deepest gratitude to all those who have supported and guided me throughout the journey of completing this work. First and foremost, I am grateful to Prof. Mikhail Itskov for his guidance, insightful discussions, and unwavering support. His expertise and encouragement have been instrumental in the successful completion of this thesis. Thank you for the trust you have placed in me and for the responsibility and opportunities you have given me for my personal growth.

I would like to express my sincere gratitude to all my co-authors for their joint efforts and contributions, which have greatly enriched this research. In particular, I would like to thank Prof. Julius Kaplunov and Danila Prikazchikov for their constructive feedback, fruitful discussions, and academic guidance. Prof. Julius Kaplunov, thank you for inviting me to Keele University and for your countless visits to our department, during which I learned a great deal about asymptotics. I would also like to express my gratitude to József Kalmár for providing the data set utilized in the final chapter of this work.

My sincere appreciation goes to my first friends in the department, Ameya Rege, Rajesh Chandrasekaran, and Markus Hillgärtner, whose camaraderie made the early days enjoyable and memorable. A special mention goes to my former students who are now valued colleagues: Weibo Xiong and Prakul Pandit. Their dedication and motivation have been inspiring. I am also grateful to my colleagues Vu Ngoc Khiêm, Xuefeng Tang, Nirav Shah and Michał Rajski for their support, stimulating conversations, and shared experiences that made our working environment productive and enjoyable. I will never forget the many game nights we had. Additionally, I would like to thank my former students Jendrik Weise, Pablo Margono, Siddharth Srivastava, Teresa Rodriguez Sanchez, Rylan Peroz and Abhishek Setty for their hard work and their valuable contributions. You supported me in all my projects, contributed to ideas and were valuable discussion partners. I am indebted to our secretaries Eva-Maria Kunert and Anika Bartz for their administrative support which ensured smooth progress throughout my research endeavors.

On a personal note, I owe an immense debt of gratitude to my wife Dagmara for her unwavering love, patience, and encouragement. To my daughter Lina for being a constant source of joy since the day she was born. Lastly, but just as important, I would like to thank my siblings, Sulejman and Khava, as well as my parents, Isa and Zarga, for their unconditional love, support, and belief in me. Their encouragement over the last years has been a cornerstone in achieving this milestone.

To all those mentioned above and many others who indirectly contributed, thank you from the bottom of my heart. This accomplishment would not have been possible without your collective support.

Aachen, August 2024
Rasul Abdusalamov

Contents

1	Introduction	1
1.1	Motivation	4
1.2	State of the Art	5
1.2.1	Classical Constitutive Modeling Approaches	5
1.2.2	Data-Driven Modeling Approaches	7
2	Basics of Symbolic Regression	11
2.1	Genetic Programming	13
2.1.1	Initialization and Selection	15
2.1.2	Evolution and Termination	15
2.2	Deep Symbolic Regression	19
2.2.1	Reinforcement Learning Based Approach	19
2.2.2	Constraints and Reward Function	21
3	Continuum Mechanical Framework	25
3.1	Constitutive Equations	25
3.2	Remarks on Implementation	27
4	Benchmark Tests Using Artificial Data	31
4.1	Incompressible Generalized Mooney-Rivlin Model	31
4.1.1	Performance of gplearn	33
4.1.2	Performance of DSO	37
4.1.3	Conclusion	37
4.2	Nearly Incompressible Mooney-Rivlin Model	40
4.3	Influence of Train-Test Data Splits	41
4.4	Remarks on Stretch-Based Ogden Model	42
5	Benchmark Tests Using Experimental Data	47
5.1	Multi-Axial Loading of Vulcanized Rubber	47
5.2	Stretch-Based Model Identification	58
5.3	Biaxial Loading of Vulcanized Rubber	60
5.4	Temperature-Dependent Thermoplastic Polyester Elastomer	65
6	Rediscovering the Mullins Effect	71
6.1	Benchmark Tests Using Ogden-Roxburgh Model	74
6.2	Temperature-Dependent Filled Silicone	80

7	Microstructural Aerogel Modeling	87
7.1	Modeling of Silica Aerogels Using Aggregated Structures . . .	92
7.1.1	Diffusion-Limited Cluster-Cluster Aggregation	94
7.1.2	FE-Based Microstructure Analysis	97
7.1.3	Silica Aerogel Modeling	103
7.2	Open-Porous Cellular-Like Aerogels	104
7.2.1	Laguerre-Voronoi Tessellation	106
7.2.2	FE-Results and Data Set Analysis	106
7.2.3	Open-Porous Cellular-Like Aerogel Modeling	107
8	Hydration Effects in Polyamide Aerogels	113
8.1	Experimental Characterization	114
8.2	Hydration Effect Modeling	116
9	Conclusion	119
	List of Figures	XVII
	Bibliography	XXI
A	Introduction to Tensor Calculus	i
B	Foundations of Continuum Mechanics	v

1 Introduction

We are at the very beginning of time for the human race. It is not unreasonable that we grapple with problems. But there are tens of thousands of years in the future. Our responsibility is to do what we can, learn what we can, improve the solutions, and pass them on.

R. P. FEYNMAN

Over the past decade, the field of artificial intelligence (AI) has significantly impacted the process of solving research problems in science and engineering. A significant contributing factor to this transformation has been the explosion in quantity and quality of available data. Advances in computing, imaging techniques, and the development of fast and high-precision electronic components have contributed to the acceleration of this change. This exponential growth in data is challenging traditional approaches and enabling the development of innovative solutions in many research areas. It is now possible to collect and analyze vast amounts of data with high accuracy and speed. In materials science, techniques such as scanning electron microscopy (SEM), atomic force microscopy (AFM), and X-ray diffraction (XRD) are generating data sets of unprecedented detail, leading to new insights into microstructural properties and a better understanding of the macroscopic properties of materials. One particular area where innovative methodologies have demonstrated considerable potential is in the field of materials modeling. The modeling of materials involves the application of computational techniques for the prediction of material properties and behaviors under diverse conditions. In the past, this has been accomplished through the use of physical models based on established theories regarding the properties of different materials. However, these models frequently depend on simplifications and assumptions that can restrict their precision. In contrast, data-driven (DD) approaches permit the determination of physical relationships directly from experimental data, eliminating the necessity for simplifying assumptions [14]. This is particularly advantageous for the development of constitutive equations that describe the relationship between specified inputs and outputs. The combination of large data sets and machine learning techniques allows for the development of more accurate and comprehensive models of material behavior that better reflect the complexity of real-world conditions. Consequently, a novel research area has emerged in the field of solid mechanics, namely the identification of constitutive

models using DD methods. These novel methods may be referred to as DD approaches, as they are solely focused on the identification of material laws driven by experimental or numerical observations. In contrast to traditional classical modeling, these approaches are based on advanced computational techniques, including machine learning, reinforcement learning, and other statistical methods. A visual representation of the classification of constitutive modeling into classical and data-driven approaches can be viewed in Figure 1.1.

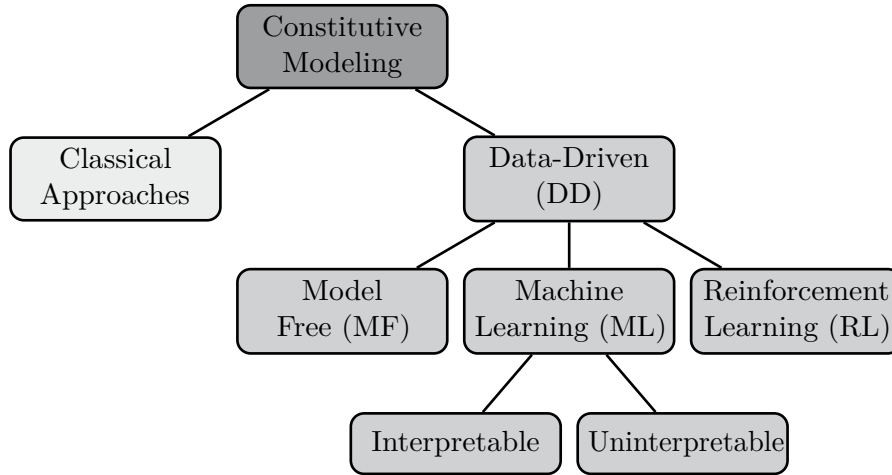


Fig. 1.1: Classification of constitutive modeling, including classical and data-driven approaches. Data-driven approaches are further subdivided into three categories: model-free (MF), machine learning (ML), and reinforcement learning (RL). Within the ML category, approaches are distinguished based on their interpretability. An alternative classification scheme is presented in [14].

Model-free approaches integrate an experimental material observation directly into the solution of a mechanical problem, avoiding any analytical linkage in the constitutive relationship. This approach was initially proposed by Kirchdoerfer and Ortiz, and the fundamental premise is to derive the solution to a boundary value problem through a collection of material observation pairs, relying solely on discrete observations [15]. Consequently, the solution is inherently linked to the provided data set, thereby eliminating potential errors and uncertainties since no experimental information is lost. The relaxed problem is solved by minimizing a distance function to the data set in phase space, taking into account the given constraints introduced by conservation laws.

One of the most effective tools in the domain of DD methods is machine learning (ML). A specific application is the utilization of artificial neural networks (ANNs), which belongs to the category of uninterpretable approaches, given that an ANN is a "black box". ML approaches are applicable to both classification and regression problems. They are capable of making predictions

by adjusting the weights and biases of the ANN. The analysis of complex data sets can facilitate the discovery of relationships that may not be immediately apparent when employing traditional analytical methods. These approaches frequently demonstrate efficacy in addressing high-dimensional and nonlinear problems, provided that a sufficiently large data set is available. In the early 2000s, Shen et al. presented an initial approach to constitutive modeling [16]. With regard to interpretable methodologies, two distinct approaches have emerged: sparse and symbolic regression. Although the respective names suggest a certain degree of similarity, the underlying functionalities of the two approaches are, in fact, entirely distinct.

Symbolic regression (SR) is an algorithmic technique that seeks to identify a mathematical function that optimally represents the relationship between input and output data. In contrast to polynomial regression, this approach does not require the specification of a particular model structure. Instead, it allows for the use of mathematical functions, such as exponential and angular, to identify an expression that is both accurate and parsimonious. A significant benefit of this approach is that it is not subjected to potential biases inherent in human decision-making. Symbolic regression frequently employs genetic programming to identify the optimal solution, with roots tracing back to the initial investigations of the 1970s [17]. In sparse regression, the objective is to identify the most parsimonious model that balances accuracy with model complexity, thereby avoiding overfitting. In contrast to symbolic regression, a crucial initial step involves the selection of a set of arbitrary candidate functions, which may include polynomial, trigonometric, and other types of functions. These functions serve as a library from which the sparse regression algorithm (often a sequential threshold least-squares algorithm) automatically selects the terms that most accurately interpret the data while maintaining parsimony, or a minimal number of terms. The objective is to approximate the desired functional relationship between input and output variables. The method employs a sparse regularization technique to enforce sparsity in the model, such as L_1 regularization, also known as Lasso (least absolute shrinkage and selection operator) or, more generally, L_p regularization with $0 < p \leq 1$. This statistical method was first introduced in the late 1980s as a means of solving optimization problems [18].

Moreover, reinforcement learning (RL) methods have been introduced in recent years for the purpose of material modeling [19]. Reinforcement learning (RL) is a closed-loop machine learning technique that employs an interaction-based learning approach, dating back to the early days of machine learning [20]. An agent can perform actions within an environment, thereby modifying the state of that environment, and receive feedback in the form of a reward. During this process, the agent interacts with the environment in an effort to adjust, identify, and learn the most suitable actions for maximizing the received reward signal. Consequently, in the most challenging case, the selected action may even influence subsequent rewards in the future. This results in a fundamental

challenge in reinforcement learning: the trade-off between exploration (identifying new actions to maximize reward) and exploitation (using known actions to maximize reward).

The methods presented in this initial introduction each have distinct advantages and disadvantages. Consequently, the following sections will clarify the objective behind this work by providing a comprehensive analysis of the limitations of these approaches. Section 1.1 will underscore the benefits for using symbolic regression as a superior technique for identifying material models. In addition, an examination of the current state of the art in constitutive modeling, including both data-driven methods and classical models, will be provided in Section 1.2.

1.1 Motivation

The process of identifying, calibrating, and developing material models is often regarded by researchers as more of an art than a science. This viewpoint is for example illustrated in the book *Mechanics of Solid Materials* by Jean Lemaitre and Jean-Louis Chaboche [21]. The field of material modeling presents a number of challenges, particularly with regard to the selection of appropriate functions and the accurate determination of their numerical coefficients. This complexity is a result of the lack of standardized processes and clear guidelines for achieving these objectives. Consequently, researchers must navigate a complex landscape that requires a combination of creativity and technical expertise to effectively model material behavior. Classical phenomenological approaches necessitate an iterative strategy in which theoretical insights are continuously refined through empirical validation. A notable limitation of classical modeling is its susceptibility to human bias during the identification of suitable material models. Consequently, this process is not always grounded in the scientific method, and requires substantial research experience to identify effective models.

To address this limitation, one of the primary objectives of this work is to develop an unbiased and reliable strategy for the accurate identification of material models. The objective of this work is to mitigate the impact of subjective influences and enhance the robustness and reproducibility of material model identification through SR. The aim of this thesis is to examine the potential of SR as a tool for constitutive material modeling and to assess its capabilities in this context. The initial focus will be on identifying hyperelastic, incompressible, and nearly incompressible material models. A primary objective is to identify strain energy functions that already satisfy the fundamental principles of material theory. Accordingly, a continuum mechanical framework will be integrated with SR, incorporating the extensive theoretical research conducted over the past decades. The efficacy of SR in this context will be substantiated through the utilization of classical benchmark tests with artificial

data. The evaluation will encompass both interpolation and extrapolation capabilities. Moreover, it is crucial to assess the efficacy of SR in identifying novel material models from well-documented experimental data sets, as well as from a temperature-dependent data set. Another objective of this research is to expand the applicability of SR to damage modeling, with a particular focus on the Mullins effect observed in rubber-like materials. Furthermore, the research will contribute to the understanding and modeling of microstructural phenomena in aerogels. The primary objective is to elucidate the influence of microstructural characteristics on macroscopic properties and to generate innovative material models that incorporate these effects. Of particular interest is the modeling of hydration effects in polyamide aerogels, with the aim of gaining a deeper understanding of the manner in which microstructural changes affect the overall behavior of the material.

1.2 State of the Art

The following section provides a concise overview of the current state of the art in constitutive modeling. It discusses both classical constitutive and data-driven modeling approaches, which have gained significant attention in recent years.

1.2.1 Classical Constitutive Modeling Approaches

The earliest known applications of classical constitutive modeling approaches can be traced back to the early 1940s, when Mooney demonstrated that Hooke's law was insufficient for accurately describing the stress-strain behavior of elastomeric materials [22]. As a result, the field of nonlinear elasticity theory was subsequently developed. This theory is capable of accommodating large strain nonlinear responses and is based on the Helmholtz free energy per unit reference volume, which is a scalar function that relates strain energy to deformation. Over time, numerous material models have been formulated to predict the mechanical behavior of hyperelastic materials, which is of crucial importance for applications in engineering components and systems.

One of the earliest models developed is the neo-Hookean model. In the incompressible case, the strain energy Ψ is given by

$$\Psi = \frac{1}{2}k_B T m (I_C - 3) = C(I_C - 3), \quad (1.1)$$

where k_B is the Boltzmann's constant, T is the absolute temperature, and m denotes the number of polymer chains per unit volume. Therefore, the constant C represents a single material parameter. It should be noted that in the case of the nearly incompressible formulation, it is necessary to determine the bulk modulus, represented by the parameter κ , as an additional material

parameter. One of the major advantages of this approach is its simplicity and ease of use. However, this simplicity comes at a cost as the approach is limited in its accuracy in predicting complex deformations and does not accurately capture the behavior under different loading conditions.

The eight-chain model, as proposed by Arruda and Boyce, has been demonstrated to yield accurate predictions under uniaxial tension (UT) and pure shear (PS) loading conditions [23]. The strain energy for this model is given by the following equation

$$\Psi = k_B T N m \left(\sqrt{\frac{\mathbf{I}_C}{3N}} \mathcal{L}^{-1} \sqrt{\frac{\mathbf{I}_C}{3N}} + \ln \frac{\mathcal{L}^{-1} \sqrt{\frac{\mathbf{I}_C}{3N}}}{\sinh \mathcal{L}^{-1} \sqrt{\frac{\mathbf{I}_C}{3N}}} \right) - C, \quad (1.2)$$

where \mathcal{L}^{-1} is the inverse Langevin function, N is the number of chain segments, while C is a constant such that the energy is zero in the reference state. This model is micro-mechanically inspired and based on statistical mechanics, which describes the deformation behavior of polymer chains. Nevertheless, the model shows a reduced level of accuracy in predicting equibiaxial tension (EBT) and is based on a number of assumptions regarding chain deformations.

The extended tube model substantially enhances the predictive capabilities for UT, PS, and EBT loading cases by integrating non-Gaussian statistics and an additional inextensibility parameter δ [24]. In its formulation, it includes contributions from both chain cross-linking and entanglement effects, and is given by

$$\begin{aligned} \Psi &= \Psi_c + \Psi_{ph} \\ &= \frac{G_c}{2} \left\{ \frac{(1 - \delta^2)(\mathbf{I}_C - 3)}{1 - \delta^2(\mathbf{I}_C - 3)} + \ln [1 - \delta^2(\mathbf{I}_C - 3)] \right\} \\ &\quad + \frac{2G_e}{\beta^2} \sum_{i=1}^3 (\lambda_i^{-\beta} - 1). \end{aligned} \quad (1.3)$$

In this case, the strain energy is decomposed into two distinct contributions, the additional energy of the constrained fluctuations of the polymer chain junctions, which is represented by Ψ_c , and the energy of the phantom-like network, which is described by Ψ_{ph} . It should be noted that the contribution of the phantom-like network is described by an Ogden model. In order to apply this model to a given material, it is necessary to determine the material constants G_c , G_e , β and δ . The disadvantages of this approach are the complex calibration process and the high computational cost and time required for numerical simulations.

More recent developments include the formulation of a micro-mechanical model based on analytical network averaging of the tube model, which employs a closed-form expression of the exact Rayleigh distribution function for non-

Gaussian chains [25]. The strain energy for this model is given by

$$\begin{aligned}\Psi &= \Psi_c(I_C) + \Psi_t(II_C) \\ &= \mu_c \kappa n \ln \frac{\sin\left(\frac{\pi}{\sqrt{n}}\right) \left(\frac{I_C}{3}\right)^{\frac{q}{2}}}{\sin\left(\frac{\pi}{\sqrt{n}}\right) \left(\frac{I_C}{3}\right)^{\frac{q}{2}}} + \mu_t \left[\left(\frac{II_C}{3}\right)^{\frac{1}{2}} - 1 \right],\end{aligned}\quad (1.4)$$

where Ψ_c is defined as the strain energy of the ideal network, while Ψ_t represents the strain energy due to topological constraints. The parameters μ_c , κ , n , q , and μ_t are all material constants to be determined. While this material model provides highly accurate results for experimental data, a notable drawback is the sophisticated calibration procedure and the substantial expert knowledge necessary for optimal deployment.

In recent years, numerous additional material models have been introduced, frequently concentrating on highly specialized materials and delineating particular effects. Each of these approaches raises a number of concerns. Firstly, it is challenging to calibrate these material models, as several material parameters are required. Secondly, a significant limitation of many models is their restricted predictive accuracy in specific loading scenarios. This is attributable to the nature of the input data selected, as well as the assumptions made during the model development process. Third, for use in commercial finite element (FE) solvers, a significant investment of time is required for the implementation of each specific model as a user material model. Therefore, it is evident that a more sophisticated approach is necessary, capable of generating specific material models while maintaining a reasonable computation time without the need for extensive expert knowledge. Furthermore, the approach must be implementable for practical use in industrial applications.

1.2.2 Data-Driven Modeling Approaches

Some of these shortcomings can be circumvented by employing DD techniques for the modeling of the complex inelastic behavior of rubber-like materials. The following section provides a brief overview of the advantages and disadvantages of model-free and reinforcement learning approaches. A more comprehensive analysis is presented for CANNs and sparse regression, which have been the subject of increased interest from the scientific community.

Despite the fact that model-free modeling approaches have been employed in a variety of applications, including the modeling of nonlinear elasticity [26], the modeling of fracture mechanics [27], the modeling of multiscale behavior [28], and the modeling of computational plasticity [29], the practical utilization of these approaches in industrial applications remains a significant challenge. This issue arises from the fact that the results obtained are directly correlated with the data used. Consequently, it is challenging to obtain results that

are fully unique, as the data dependency affects the prediction. Moreover, model-free methodologies result in models that are not easily interpretable and offer only limited insight into the underlying physical processes that govern the material behavior. Furthermore, integrating such a methodology into a commercial FE solver represents a significant challenge.

RL techniques have been utilized for the identification of hyperparameters in self-designing neural networks based on elasto-plastic constitutive laws [30], the identification of microstructure-based traction-separation laws [31], and the identification of growth evolution laws of arteries [32]. The primary disadvantage of RL approaches is the necessity of a preliminary training phase, which limits their suitability for practical applications. The high sample complexity, which is a consequence of the necessary interactions between the agent and the environment, presents a significant challenge to effective learning. Moreover, the "black box" nature of RL models presents a challenge in gaining physical insights. Furthermore, the issue of knowledge transfer remains, as RL models may not generalize effectively, thereby limiting the transferability of a material model to a new material.

The ANN approach initially proposed by Shen et al. was subsequently enhanced by Linka et al. through the development of invariant-based constitutive artificial neural networks (CANNs) [33]. Moreover, an extension of the CANNs was conducted through the direct incorporation of the polyconvexity condition [34], as well as through an approach based on physically constrained symbolic models [35]. Additionally, Fuhg and Bouklas have proposed a probabilistic machine learning approach for data-driven isotropic and anisotropic constitutive models [36]. A preliminary investigation into the prediction of inelastic effects in cross-linked polymers using neural networks was presented by Ghaderi et al. [37]. The application of neural network constitutive models to nonlinear electro-elastic finite element analysis has been explored [38], as well as the potential of sparsification techniques for physics-augmented neural networks in enabling interpretable model discovery [39]. Although artificial neural networks offer significant advantages in model discovery, they are not without limitations. First and foremost, they are regarded as "black boxes," which presents a significant challenge to interpretation. The training of such models requires a significant computational effort, and the high complexity of the resulting models can hinder further applications, such as FE simulations. A recent approach by Linka and Kuhl seeks to address these limitations through the introduction of a new CANN architecture family for automated model discovery. This novel method addresses the shortcomings of the "black box" nature of the neural network by providing a straightforward interpretation of the neural network weights (see Figure 1.2). The primary concept proposes a CANN architecture with two hidden layers, which approximate the free energy function ψ as a function of the scalar-valued invariants $I_{\mathbf{F}}$, $II_{\mathbf{F}}$, $III_{\mathbf{F}}$ and $IV_{\mathbf{F}}$ of the deformation gradient \mathbf{F} . In the initial hidden layer, each of the invariants are developed as power terms. In the subsequent layer, thermodynamically

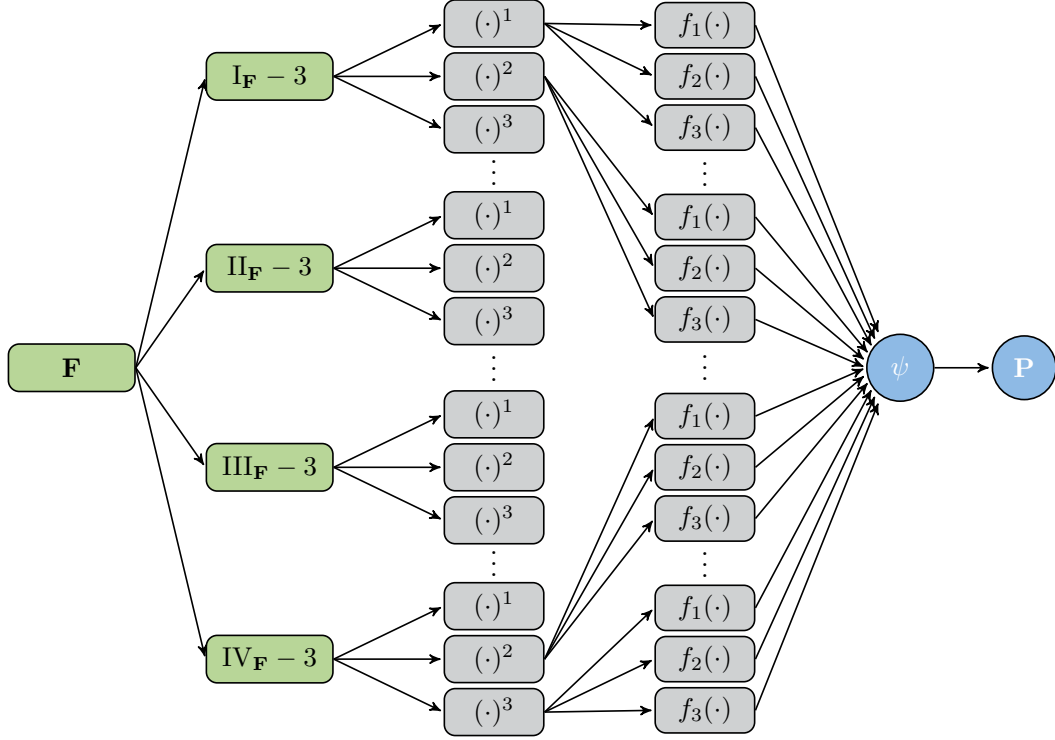


Fig. 1.2: Illustration of the CANNs architecture with two hidden layers, as described in [40]. The inputs of the CANN are the invariants $\mathbf{I}_{\mathbf{F}}$, $\mathbf{II}_{\mathbf{F}}$, $\mathbf{III}_{\mathbf{F}}$ and $\mathbf{IV}_{\mathbf{F}}$ of the deformation gradient \mathbf{F} . The purpose of the CANN is to approximate the free energy function ψ . In the first hidden layer, power terms of these invariants up to the third order are computed. In the second hidden layer, thermodynamically admissible activation functions $f_i(\cdot)$ are applied to these power terms.

admissible activation functions, represented by $f_i(\cdot)$ are applied to these powers. Consequently, the free strain energy ψ is given by

$$\psi = \sum_{i=1}^4 \sum_{k=1}^3 \sum_{\ell=1}^3 w_{2,m} f_{\ell} \left(w_{1,m} \tilde{I}_i^k \right) \quad \text{with} \quad m = 9(i-1) + 3(k-1) + \ell, \quad (1.5)$$

where the invariants \tilde{I}_i are given by $\tilde{I}_1 = \mathbf{I}_{\mathbf{F}} - 3$, $\tilde{I}_2 = \mathbf{II}_{\mathbf{F}} - 3$, $\tilde{I}_3 = \mathbf{III}_{\mathbf{F}} - 1$ and $\tilde{I}_4 = \mathbf{IV}_{\mathbf{F}} - 1$, respectively. The choice of activation functions is typically constrained to the identity function or the exponential function. It is important to note that this CANN has precisely two weight vectors. Consequently, the primary objective of the neural network is to identify the optimal coefficients for the linear combination of these terms. Although this approach enhances interpretability, it essentially represents a process of adjusting the weights and biases. An alternative approach could have been to employ a conventional nonlinear optimization scheme. Furthermore, it is crucial to underscore that the proposed methodology does not lead to the discovery of novel models. In contrast, its fundamental objective is to identify the most suitable combination

of terms from a given set of functions that is most closely aligned with the underlying data.

An alternative methodology for data-driven automatic discovery of constitutive laws was proposed by Flaschel et al. utilizing sparse regression based on displacement and global force data [41]. This work was further extended by the introduction of physically consistent deep neural networks, which were employed for the discovery of both isotropic and anisotropic hyperelastic constitutive laws [42]. Recently, this approach has been extended through the creation of novel libraries of material models based on formal grammars [43] as well as for the discovery of plasticity models [44]. The primary concept is the utilization of a feature library, denoted by the vector $\mathbf{Q} : \mathbb{R}^3 \rightarrow \mathbb{R}^{n_f}$. The feature library is a set of n_f nonlinear functions that depend on the invariants of the isochoric right Cauchy-Green tensor $\mathbf{I}_{\bar{\mathbf{C}}}$, $\mathbf{II}_{\bar{\mathbf{C}}}$, and J . It serves as a basis for a linear combination of a strain energy density function, which is given by

$$\Psi = \mathbf{Q}(\mathbf{I}_{\bar{\mathbf{C}}}, \mathbf{II}_{\bar{\mathbf{C}}}, J) \cdot \boldsymbol{\theta}, \quad (1.6)$$

where the vector $\boldsymbol{\theta} \in \mathbb{R}^{n_f}$ is used to group the unknown coefficients associated with each element of the library. The library \mathbf{Q} is defined as follows:

$$\begin{aligned} \mathbf{Q} = & \left[(\mathbf{I}_{\bar{\mathbf{C}}} - 3)^i (\mathbf{II}_{\bar{\mathbf{C}}} - 3)^{j-i} : j \in \{1, \dots, N\}, i \in \{0, \dots, j\} \right] \\ & \oplus \left[(J - 1)^{2k} : k \in \{1, \dots, M\} \right] \oplus [\ln(\mathbf{II}_{\bar{\mathbf{C}}}/3)] , \end{aligned} \quad (1.7)$$

where the initial contribution represents Mooney-Rivlin terms, the second list of elements corresponds to the volumetric terms, and the final component is a single logarithmic feature. The operator \oplus represents a simple vector concatenation. The vector of unknown constants, denoted by $\boldsymbol{\theta}$, is determined through a minimization problem for a particular linear equation system derived from a weak form. Although this approach is valuable in its emphasis on a parsimonious selection of terms through the Lasso operator, a notable criticism is that it has limited potential for discovering new material models. The resulting model will inherently be incapable of exceeding the predictive capacity offered by all possible combinations within the feature library. The purpose of this approach is to identify the optimal coefficients for a minimal subset of terms derived from the feature library. Therefore, the challenge of discovering genuinely novel models remains unresolved within the current state of the art. The proposed methods are effective in identifying optimal models with accurately calibrated coefficients. A rigorous and empirically-grounded approach to the discovery of novel material models has yet to be presented. The following chapters will examine how symbolic regression can serve as a potential alternative approach to address this challenging task.

2 Basics of Symbolic Regression

Make everything as simple as possible, but not simpler.

A. EINSTEIN

In general, regression analysis is a statistical technique that seeks to establish mathematical relationships between one or more independent variables and a single dependent variable. Typically, an initial model structure is provided, comprising a set of parameters that are optimally fitted to a given data set. One of the most common examples is linear regression. Nevertheless, the assumption of a linear relationship between inputs and outputs entails a number of limitations. The linear regression model is unable to capture complex nonlinear patterns in the data. Furthermore, the technique is based on the assumption of homoscedasticity, which may not be applicable in real-world scenarios, potentially leading to unreliable estimates. Furthermore, linear regression is susceptible to the influence of outliers and leverage points. Such factors have the potential to bias the model's parameter estimates and thereby negatively impact its predictive accuracy.

Symbolic regression (SR) represents a novel interpretable machine learning algorithm, a unique form of regression analysis that operates independently of a pre-specified initial model. It employs an iterative search through a comprehensive set of mathematical expressions with the objective of identifying the most suitable mathematical formula for describing the relationship between the specified inputs and the desired output. In contrast to polynomial regression, this approach permits the use of mathematical functions such as exponential, logarithmic, and angular functions. The objective is to identify an expression that is both accurate and simple. Figure 2.1 illustrates the iterative evolution of an expression through a genetic algorithm using SR, which is employed to describe the provided data set in the most optimal manner. Consequently, the method is highly independent of any potential human bias or lack of domain knowledge. The result is an algebraic equation. One of the most significant advantages is that the learned models are provided as a "white box," which permits straightforward interpretation. This presents an opportunity to gain insight into the fundamental characteristics of the acquired model.

The earliest research on SR can be traced back to the 1970s [17, 45, 46], during which the primary objective was to rediscover empirical laws by employing iterative data-driven heuristics to derive mathematical expressions. Subsequently, further advances in SR were explored by Koza [47–49], who

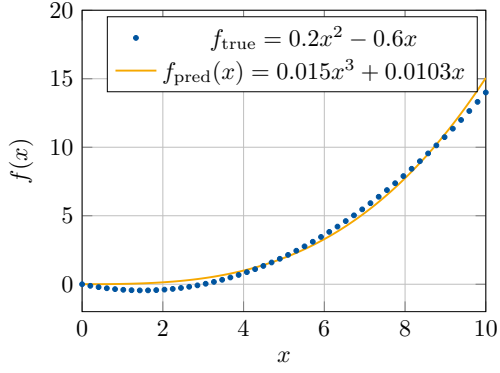
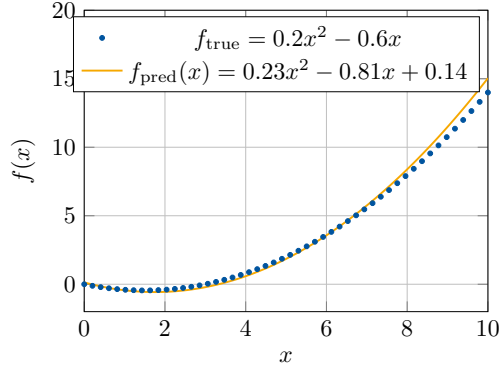
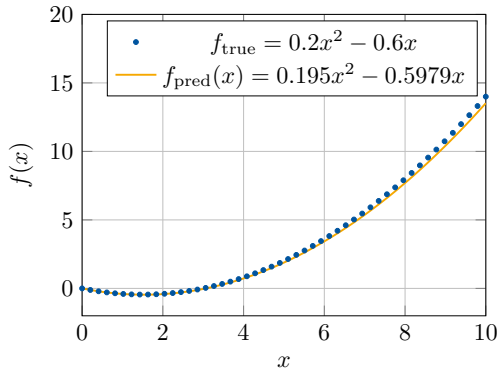
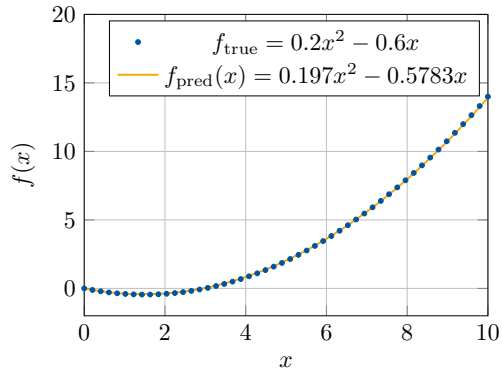
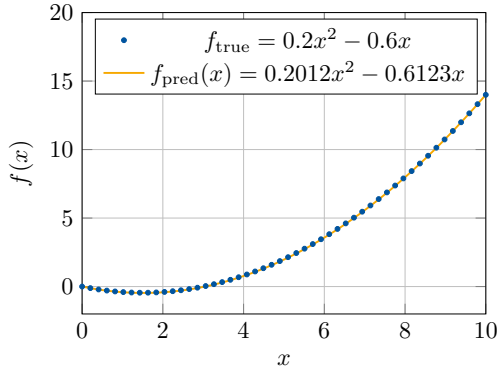
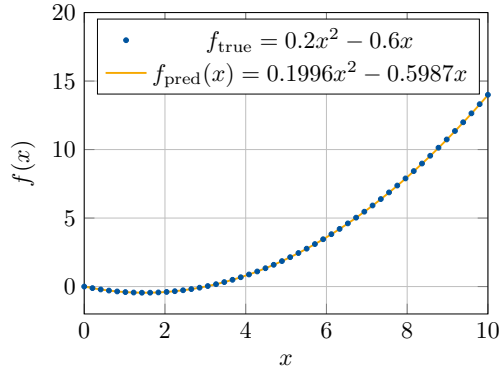
(a) Generation 1, Fitness = 3.25×10^{-1} (b) Generation 3, Fitness = 2.45×10^{-1} (c) Generation 5, Fitness = 1.41×10^{-1} (d) Generation 7, Fitness = 0.27×10^{-1} (e) Generation 9, Fitness = 0.19×10^{-1} (f) Generation 10, Fitness = 0.05×10^{-1}

Fig. 2.1: Visualization of the iterative evolution of an expression over 10 generations, utilizing the `gplearn` package. The underlying true data was generated using the function $f_{\text{true}} = 0.2x^2 - 0.6x$. After 10 generations, the model successfully identifies the underlying function, achieving a fitness value of 0.05×10^{-1} .

proposed the use of genetic programming (GP) to discover symbolic models by encoding mathematical expressions as computational trees. GP has also

been studied since the 1970s and is based on the idea of iterative evolution of an initial population of individuals through time [50–52]. An overview of the interpretable scientific discovery and its historical development is provided in [53].

A number of libraries exist for SR, beginning with a symbolic regression framework known as `gplearn` that is based on GP [54]. One of the most promising approaches is the deep symbolic optimization (DSO) framework proposed by Petersen et al., which introduces a novel method combining recurrent neural networks for the prediction of algebraic equations [55]. This approach produces a "white box" model using a "black box". Additionally, a number of other libraries are available, including `AlFeynman`, which employs a recursive divide-and-conquer approach [56], `Operon`, which incorporates a non-linear least squares constant optimization method, and the Bayesian symbolic regression framework (BSO), which utilizes the Markov Chain Monte Carlo method. A comprehensive examination of the advantages and limitations of a diverse list of libraries is provided in [57].

In Section 2.1 a brief introduction to genetic programming is presented. GP is utilized in both the `gplearn` and the DSO package. For further details on GP, the interested reader is referred to [48, 58, 59], among others. Furthermore, the concepts of deep symbolic regression and its application for this work is summarized in Section 2.2. The two packages will be employed throughout this work for the identification of strain energy functions based on the continuum mechanical framework presented in Chapter 3. A comparison of their respective performances will be presented in Chapter 4. This chapter presents an edited version of the fundamental concepts introduced in my previous publications [1, 3, 4].

2.1 Genetic Programming

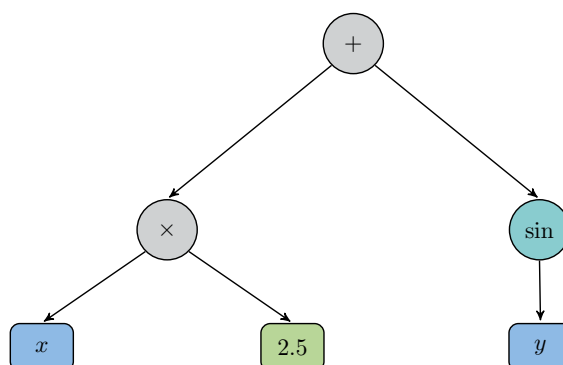
Mathematical expressions, such as strain energy functions, can be represented graphically as a rooted tree. Such trees are frequently designated as computational graphs, calculation trees, or expression trees and are traversed from the root. There are multiple methods for establishing a traversal from a tree. One method for generating an expression tree in a sequence while maintaining a one-to-one correspondence between the tree and its traversal is to evaluate each vertex within the tree, with the children on the left side evaluated after the vertex itself and the children on the right side evaluated subsequently (depth-first, left-to-right). An exemplar of a calculation tree is illustrated in Figure 2.2, where the function $f(x, y) = 2.5x + \sin y$ is visualized. The traversal for this tree is consequently $+$, \times , x , 2.5 , \sin , and y , relating to the mathematical expression of $f(x, y)$. Vertices that are not succeeded are referred to as external or terminal. Such vertices contain either one of the independent arguments (inputs) or constants. Vertices that are not succeeded

are referred to as internal. Such vertices represent mathematical operators and basic functions that connect the subsequent vertices. It should be noted that operators can be classified as either unary or binary.

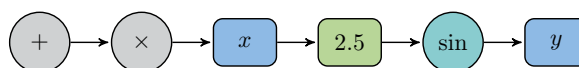
Expression:

$$f(x, y) = 2.5x + \sin y$$

Tree:



Traversal:







Legend:  : Operator  : Function  : Constant  : Argument

Fig. 2.2: Illustration of an expression tree representing the function $f(x, y) = 2.5x + \sin y$. The traversal of this tree is given with $+$, \times , x , 2.5 , \sin , and y .

A GP algorithm is typically divided into four distinct phases: initiation, selection, evolution, and termination. In the initial phase, a preliminary set of expressions is randomly generated from a predefined set of mathematical operations, independent arguments, and functions. In the selection phase, the initial set of expressions is assessed in a tournament. In this manner, random subsets are formed, and the most fit individual within each subset is identified. In the subsequent phase, the most fit individuals are subjected to mutation. A variety of mutation types are available, including crossover, subtree, point, and hoist mutations. The termination phase marks the end of the evolutionary process, and a winning candidate is identified. Each of the four phases is discussed in greater detail below. Readers interested in further details are referred to [60, 61], as well as the documentation of `gplearn` [54].

2.1.1 Initialization and Selection

In the initialization phase, the genetic algorithm generates a population set of random mathematical expressions based on a user-defined list of allowed basic operators (e.g., addition, multiplication, subtraction, and division), mathematical functions (e.g., exponential, logarithmic, angular, etc.), the predefined independent arguments, and numerical constants. The initial population, also referred to as the first generation of expressions, is created through a random sampling process. Given the random nature of the selection process, it is probable that the chosen equations will not be suited to the intended purpose. Two potential hyperparameters for optimization are the initial program depth and the population size. Subsequently, the selection and evolution phases are repeated for a user-defined number of generations.

The subsequent generation of mathematical expressions must be formulated in accordance with the previous generation. A tournament is conducted to identify the expression that will undergo further evolution. The preceding generation is randomly divided into subsets, within which the individuals compete against one another. For each subset, the individual exhibiting the optimal fitness level (i.e., the one that most accurately represents the underlying data) is selected as the basis for the subsequent generation. A crucial hyperparameter is the size of the tournament, which represents the number of individuals engaged in competition at any given time. This parameter exerts a considerable influence on the speed of the process, as it determines the number of individuals that are eliminated. Moreover, the diversity of subsequent generations is influenced by the number of individuals considered, which is directly proportional to the size of the tournament. An alternative method of selection is the fitness proportionate method, which is based on the likelihood of the selection of any individual related to its fitness on the provided data.

2.1.2 Evolution and Termination

The core concept of evolution is to explore novel regions within the search space by combining advantageous characteristics from diverse individuals. In the literature on genetic programming, numerous potential forms of evolution have been identified. This discussion will provide a brief overview of the most significant mutations, including the crossover, subtree, point, and hoist mutations.

Crossover

A crossover mutation results in the formation of a new individual through the combination of genetic material derived from a parent and a donor. Accordingly, two distinct tournaments must be conducted, as illustrated in Figure 2.3. In the initial stage, the original parent is selected, and a random subtree is chosen

for replacement. Similarly, within the second winner, referred to as the donor, a subtree is selected for replacement. Subsequently, the substituted element from the donor is integrated into the original parent, thereby generating a novel entity for the subsequent generation. From a mathematical perspective, this can be conceptualized as a process of replacing a randomly selected term within one expression with a term randomly chosen from the second expression.

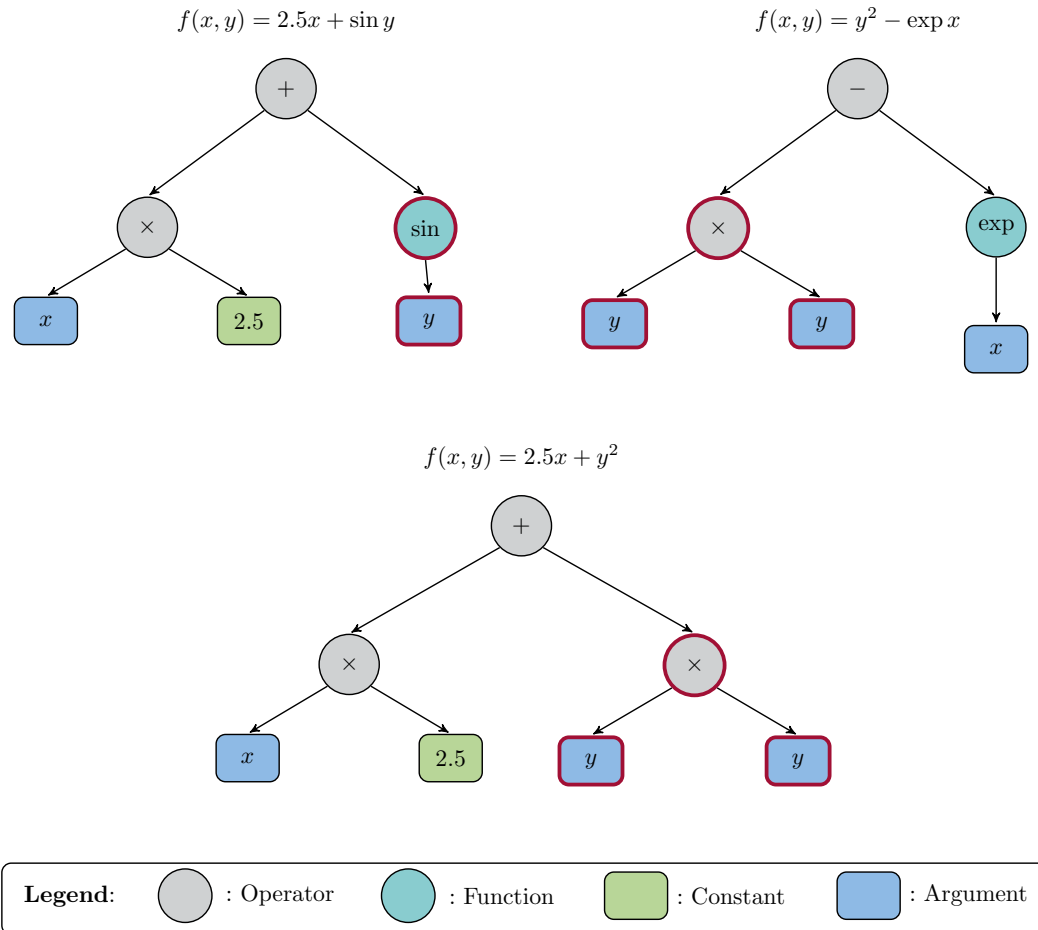


Fig. 2.3: Example of a crossover mutation where the parent $f(x, y) = 2.5x + \sin y$ and the donor $f(x, y) = y^2 - \exp x$ are used to create a new individual $f(x, y) = 2.5x + y^2$. Hereby, the randomly selected subtree term $\sin y$ of the parent is replaced with the randomly selected subtree term y^2 of the donor.

Subtree Mutation

Subtree mutation is a process that is closely related to crossover, but it requires only the original parent. In order to determine the winner of a given tournament, a random subtree is selected. In contrast to the previous method, which relied on a donor, the missing replacement is randomly generated (see

Figure 2.4). From a mathematical perspective, this can be represented as the replacement of a randomly selected term in an expression with a new term. This mutation permits the reintroduction of operators, mathematical functions, and arguments that may have become extinct over the evolutionary time, thereby preventing premature convergence. Consequently, the diversity of the population is broadened, and new regions of the search space can be investigated by introducing minor alterations to the new individuals.

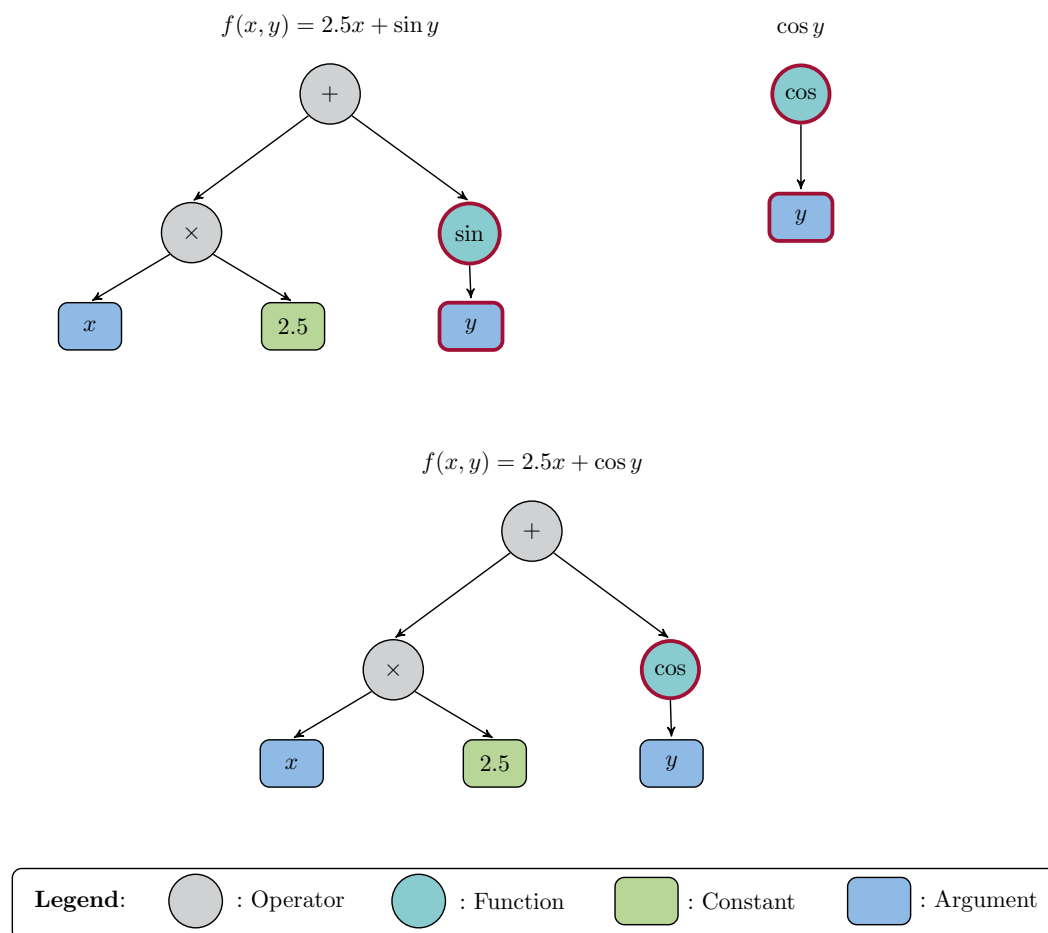


Fig. 2.4: Example of a subtree mutation for the tournament winner $f(x, y) = 2.5x + \sin y$, the random subtree $\sin y$ is selected to be substituted with a new random subtree given by the expression $\cos y$. The new created individual is $f(x, y) = 2.5x + \cos y$.

Point Mutation

A point mutation is a process whereby the winner of a tournament is replaced with a node that has been randomly selected from a set of similar nodes. This process is illustrated in Figure 2.5. It is of significant importance that functions and operators are replaced by functions and operators with an identical number

of arguments. In this process, constants and arguments are replaced by other constants and arguments. From a mathematical perspective, this approach is analogous to replacing a single random operator, function, input, or constant with another. Point mutation makes it possible to reintroduce operators and mathematical functions that may have become extinct, thereby enhancing the diversity of the population.

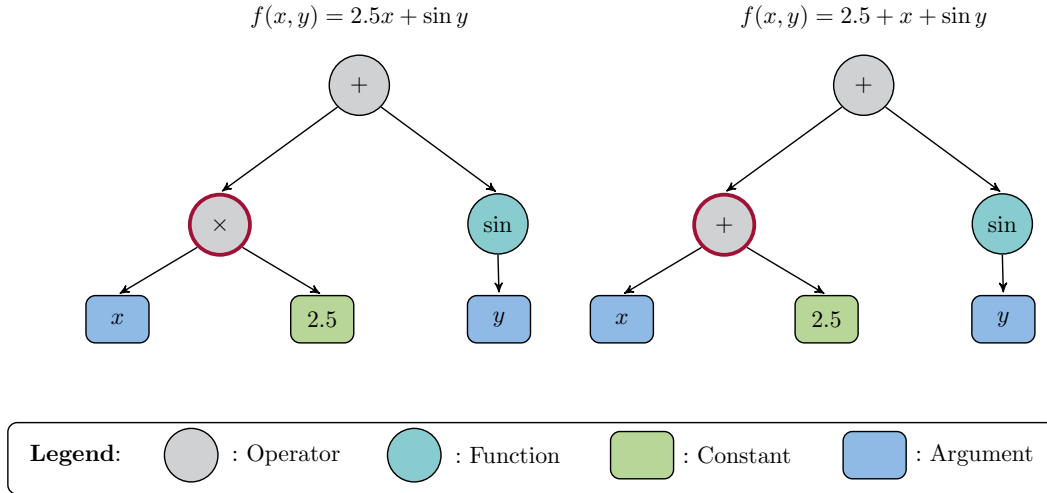


Fig. 2.5: Example of a point mutation for the tournament winner $f(x, y) = 2.5x + \sin y$, where the multiplication operator is replaced by an addition operator to create the new individual given by the expression $f(x, y) = 2.5 + x + \sin y$.

Hoist Mutation

In the case of the hoist mutation, the objective is to create a more parsimonious representation of an existing solution by replacing a randomly selected subtree with a subtree of the original tree (see Figure 2.6). This is mathematically equivalent to replacing a random term with one of its subterms, thereby shortening the overall equation. This approach helps to mitigate issues such as bloat, whereby the resulting solutions become unnecessarily large without significantly improving performance. Consequently, this can contribute to the overall computational efficiency.

The evolution process can be terminated either when the maximum number of generations has been reached or when the specified fitness threshold has been exceeded. Both are hyperparameters that can be optimized through the application of appropriate algorithms. The combination of fitness-based selection criteria (for selecting individuals for the next round) and evolutionary strategies (that randomly change or mix individuals) is designed to enhance the overall fitness of the entire population over time. Although the method ensures the generation of syntactically accurate mathematical expressions, it does not guarantee the reproduction of a deterministic solution on each random

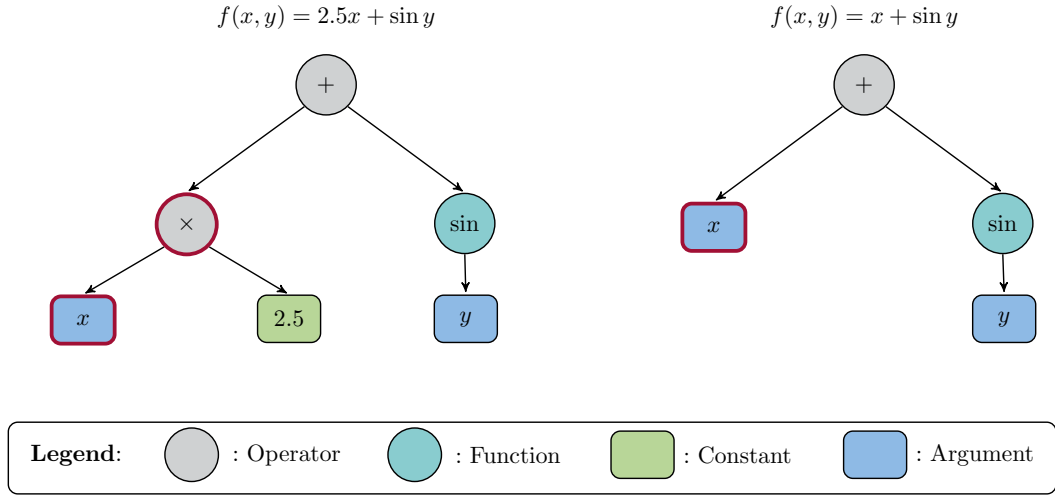


Fig. 2.6: Example of a hoist mutation for the tournament winner $f(x, y) = 2.5x + \sin y$, where the subtree given by the expression $2.5x$ is replaced by the argument x resulting in a new individual given by the expression $f(x, y) = x + \sin y$.

execution, nor does it ensure the discovery of the optimal solution. Therefore, a high maximum number of generations is useful for identifying a suitable candidate. Nevertheless, this has a direct impact on the computational cost.

2.2 Deep Symbolic Regression

The deep symbolic regression package developed by Peterson et al. represents a novel method that employs a recurrent neural network (RNN) to predict a mathematical expression based on a sampled distribution through a risk-seeking policy gradient [62]. The framework is based on a reinforcement learning approach, which will be discussed in further detail below. Furthermore, an overview of the search space constraint and the reward function is provided.

2.2.1 Reinforcement Learning Based Approach

Reinforcement learning is a closed-loop machine learning technique that employs an interaction-based learning approach. An agent is capable of undertaking actions within an environment wherein the state of that environment is subject to change, and the agent receives feedback in the form of rewards. During this process, the agent interacts with the environment and attempts to adapt, identify, and learn the most appropriate actions to maximize the received reward signal. In the most challenging case, the selected action may even influence future rewards. The DSO framework makes use of this concept. In this manner, each expression tree is transformed into a sequence, referred to as a traversal, which corresponds to the environment of the reinforcement

learning task (see Figure 2.7). The node values of the traversal are referred to as tokens, which represent either operations, functions, constants, or arguments. The recurrent neural network, which serves as the agent, is trained iteratively on a hierarchical input containing information about the entire expression tree. The traversal is decomposed into observations about siblings and parents, which are fed directly into the RNN. The next element of the traversal, corresponding to the action, is sampled based on a probability distribution function. A reward function is formulated based on the performance of the sampled expression on the given data set.

In accordance with the explanations provided in [62], the detailed process of the RL algorithm is described for the strain energy function $\Psi(I_C, II_C) = I_C + 0.5 \ln(II_C)$, which depends on the invariants I_C and II_C . This process is illustrated in Figure 2.7 and proceeds as follows:

1. In each epoch, a batch of expressions is sampled according to the following steps:
 - i. The initialization phase requires the sampling of an initial token, which represents the root of the expression tree, from a library that contains all the necessary operations, functions, constants, and arguments. The sampling of the token is based on a predefined probability distribution. This initial step does not specify any information about parent or sibling relationships. To illustrate, in the context of the function $\Psi(I_C, II_C) = I_C + 0.5 \ln(II_C)$, the first sampled token in the first iteration represents the addition operator $+$.
 - ii. Subsequent token sampling requires the updating of observations based on the previous token, the updating of the weights of the RNN, and the sampling of the next token. One of the advantages of this approach is that search space constraints can be incorporated directly into the sampling process. This may be achieved by introducing a prior into the probability distribution function. One such a priori constraint on the search space is that all children of an operator cannot be constants, given that they would otherwise be reduced to another constant. For example, in the second iteration of the subsequent sampling step, the addition operator is designated as the parent with an arity of two. Since there are no siblings, no additional information is specified. This results in the sampling of the first input I_C as the next token. The next sampled expression in the third iteration could be the multiplication operator \times for the term $0.5 \ln(II_C)$ which would have an arity of two.
 - iii. This iterative process continues until all nodes in the tree have been assigned a terminal node status, which is either a constant or an input variable. In this manner, each token within the expression

for function $\Psi(I_C, II_C)$ is sampled in a stepwise manner until an expression is identified.

2. Once the expressions have been generated, the reward is calculated (in this case) using the normalized root mean square error. A risk-seeking policy gradient is implemented with the objective of maximizing the performance of a specified fraction of the best samples. Thus, the best case performance is prioritized at the potential expense of lower worst case and average performance.

Furthermore, a prior is embedded within the sampled probability distribution. The prior is a valuable tool for constraining the search space, for example, by limiting specific sampling sequences. Furthermore, the DSO package offers a constant optimization option. Despite the increased time requirement and the potential for overfitting, this approach allows for a significantly higher rate of expression recovery. Once a prior has been sampled, the corresponding symbolic expression is instantiated and evaluated.

The benefit of this procedure is that it generates a "white box" model based on a "black box" model. When applied to experimental data, this approach has demonstrated substantial robustness [57]. The DSO package offers an extensive set of configurable hyperparameters, allowing the user to conduct experiments tailored to their specific needs and objectives. All hyperparameters may be configured via the `config.json` file. This file can be imported directly or specified through a PYTHON script. One crucial hyperparameter is `function_set`, which defines the tokens to be sampled during optimization. Another essential parameter is `n_samples`, which determines the total number of samples generated for the optimization process. Furthermore, the parameter `prior` enables the configuration of priors and constraints on the search space, while `max_length` sets the maximum traversal length. Specific hyperparameters, including `epsilon` for adjusting the risk factor in the policy gradient and `learning_rate`, have been maintained at their default values for this study. Additionally, the general layer structure controlled by the number of layers `num_layers` in the RNN has remained unchanged from the default settings. Additionally, the GP hyperparameters, including the number of generations `generations` and the tournament size `tournament_size`, as well as the mutation probabilities `p_crossover` and `p_mutate`, can be specified. The `seed` parameter can be utilized in the experiment configuration to regulate the random number generator.

2.2.2 Constraints and Reward Function

In order to ensure the efficient and effective management of the search space, a number of constraints have been included to limit its size to a manageable extent. In particular, constraints are imposed on the pre-specified minimum and maximum length of the expression tree, the set of allowed operators and

functions, and the set of allowed input variables and constants. In addition, a priori constraints are imposed, including that the children of an operator should not all be constants, that the child of a unary operator should not be the inverse of this operator, or that the children of trigonometric operators should not be other trigonometric operators. The fitness measure is estimated based on the normalized root mean square error (NRMSE), which can be calculated using the following formula:

$$\text{NRMSE} = \frac{1}{\sigma_y} \sqrt{\frac{1}{N} \sum_{i=1}^N [y_i - f(\mathbf{x}_i)]^2}, \quad (2.1)$$

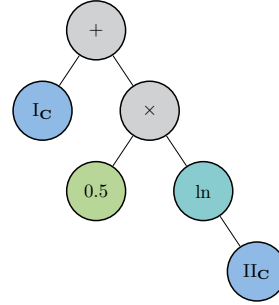
where (\mathbf{x}_i, y_i) for $i = 1, \dots, N$ is the provided data set, N is the data set size, $f(\cdot)$ is the currently evaluated function and σ_y is the standard deviation of the target values y_i . The NRMSE is employed directly in a bounded reward signal R^2 through the application of a squashing function, which is defined by

$$R^2 = \frac{1}{1 + \text{NRMSE}}. \quad (2.2)$$

Expression:

$$\Psi(I_C, \Pi_C) = I_C + 0.5 \ln(\Pi_C)$$

Graphical Tree:



Traversal:

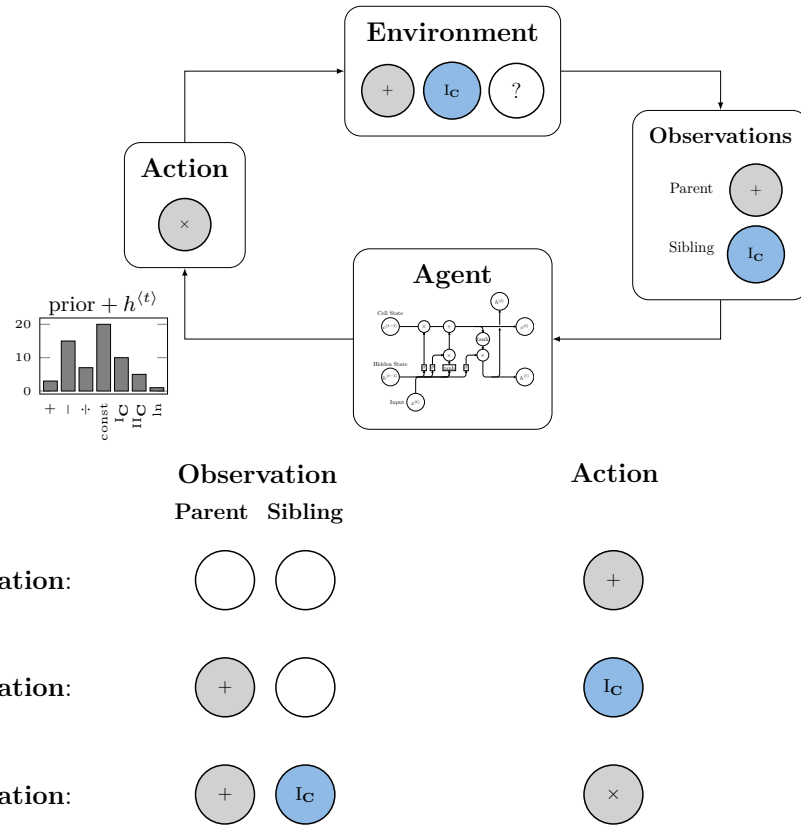


Fig. 2.7: Visualization of the deep symbolic regression process. The environment consists of a traversal of tokens where the last entry is sampled through the RNN environment. The neural network receives observations of the sibling and parent of the current token as inputs. The agent's output is a probability distribution function, which is used to sample the next action.

3 Continuum Mechanical Framework

Men pass away, but their deeds abide.

A.-L. CAUCHY

The following chapter provides a short overview of the continuum mechanical theory and the fundamental assumptions that serve as the foundation for this work. The interested reader is directed to the following foundational literature in this field: Truesdell and Noll [63], Müller [64], Holzapfel [65], Liu [66], Bertram [67], Haupt [68] and Itskov [69]. Moreover, the continuum mechanical framework for isotropic hyperelastic strain energy functions is discussed in detail in Section 3.1. Furthermore, in Section 3.2 some remarks on the implementation are presented. The fundamental concepts of continuum mechanics have been previously presented in my published work [1, 4].

3.1 Constitutive Equations

A strain energy function $\Psi(\mathbf{C})$ of an isotropic hyperelastic material can also be expressed in terms of the principal invariants $\text{I}_{\mathbf{C}}$, $\text{II}_{\mathbf{C}}$ and $\text{III}_{\mathbf{C}}$ of the right Cauchy-Green tensor $\mathbf{C} = \mathbf{F}^T \mathbf{F}$. In addition to the invariants, the strain energy may also be a function of other variables, including temperature, strain rate, damage, and loading history parameters. Accordingly, the first Piola-Kirchhoff stress tensor \mathbf{P} can be expressed as follows:

$$\begin{aligned} \mathbf{P} &= 2\mathbf{F} \frac{\partial \Psi(\mathbf{C})}{\partial \mathbf{C}} \\ &= 2 \left[\left(\frac{\partial \Psi}{\partial \text{I}_{\mathbf{C}}} + \text{I}_{\mathbf{C}} \frac{\partial \Psi}{\partial \text{II}_{\mathbf{C}}} \right) \mathbf{F} - \frac{\partial \Psi}{\partial \text{II}_{\mathbf{C}}} \mathbf{F} \mathbf{C} + \text{III}_{\mathbf{C}} \frac{\partial \Psi}{\partial \text{III}_{\mathbf{C}}} \mathbf{F}^{-T} \right]. \end{aligned} \quad (3.1)$$

It should be noted that the influence of the material is determined exclusively by the blue colored terms. The invariants $\text{I}_{\mathbf{C}}$, $\text{II}_{\mathbf{C}}$ and $\text{III}_{\mathbf{C}}$ of \mathbf{C} are given by

$$\text{I}_{\mathbf{C}} = \text{tr } \mathbf{C} \quad \text{II}_{\mathbf{C}} = \frac{1}{2} \left[(\text{tr } \mathbf{C})^2 - \text{tr } (\mathbf{C}^2) \right] \quad \text{and} \quad \text{III}_{\mathbf{C}} = \det \mathbf{C}. \quad (3.2)$$

It is required that the function $\Psi(\mathbf{C})$ satisfies the conditions of the energy and stress-free natural state at $\mathbf{F} = \mathbf{I}$. These conditions can be formulated as

follows:

$$\Psi(\mathbf{I}) = 0 \quad \text{and} \quad \left. \frac{\partial \Psi(\mathbf{C})}{\partial \mathbf{C}} \right|_{\mathbf{C}=\mathbf{I}} = \mathbf{0}. \quad (3.3)$$

In the case of nearly incompressible behavior, it is possible to multiplicatively decompose the deformation gradient into a volumetric $\hat{\mathbf{F}} = J\mathbf{I}$ and an isochoric part $\bar{\mathbf{F}} = J^{-1/3}\mathbf{F}$ according to Richter [70], where $J = \det \mathbf{F} = \sqrt{\text{III}_{\mathbf{C}}}$. Consequently, the principal invariants of the isochoric right Cauchy-Green tensor $\bar{\mathbf{C}} = \bar{\mathbf{F}}^T \bar{\mathbf{F}}$ take the form

$$\text{I}_{\bar{\mathbf{C}}} = J^{-2/3} \text{I}_{\mathbf{C}}, \quad \text{II}_{\bar{\mathbf{C}}} = J^{-4/3} \text{II}_{\mathbf{C}} \quad \text{and} \quad \text{III}_{\bar{\mathbf{C}}} = 1. \quad (3.4)$$

Accordingly, the first Piola-Kirchhoff stress tensor can be expressed as

$$\begin{aligned} \mathbf{P} = & 2 \left(\frac{\partial \Psi}{\partial \text{I}_{\bar{\mathbf{C}}}} + \text{I}_{\bar{\mathbf{C}}} \frac{\partial \Psi}{\partial \text{II}_{\bar{\mathbf{C}}}} \right) J^{-2/3} \mathbf{F} - 2 \frac{\partial \Psi}{\partial \text{III}_{\bar{\mathbf{C}}}} J^{-4/3} \mathbf{F} \mathbf{C} \\ & + J \left(\frac{\partial \Psi}{\partial J} - \frac{2}{3J} \frac{\partial \Psi}{\partial \text{I}_{\bar{\mathbf{C}}}} \text{I}_{\bar{\mathbf{C}}} - \frac{4}{3J} \frac{\partial \Psi}{\partial \text{II}_{\bar{\mathbf{C}}}} \text{II}_{\bar{\mathbf{C}}} \right) \mathbf{F}^{-T}. \end{aligned} \quad (3.5)$$

In the case of incompressible materials, for which the constraint $J = 1$ is imposed, the constitutive equation will take the following form:

$$\begin{aligned} \mathbf{P} = & 2\mathbf{F} \frac{\partial \Psi(\mathbf{C})}{\partial \mathbf{C}} - p\mathbf{F}^{-T} \\ = & 2 \left[\left(\frac{\partial \Psi}{\partial \text{I}_{\mathbf{C}}} + \text{I}_{\mathbf{C}} \frac{\partial \Psi}{\partial \text{II}_{\mathbf{C}}} \right) \mathbf{F} - \frac{\partial \Psi}{\partial \text{III}_{\mathbf{C}}} \mathbf{F} \mathbf{C} \right] - p\mathbf{F}^{-T}, \end{aligned} \quad (3.6)$$

where an additional hydrostatic pressure p can be determined from equilibrium and boundary conditions. Depending on the case, Equation 3.1, Equation 3.5 or Equation 3.6 are used for determining a strain energy formulation based on experimental or artificially created strain-stress data. In this context, only the derivatives of the strain energy density function with respect to the invariants are material-specific and will be utilized to identify an optimal expression of the strain energy function.

If it is assumed that the volumetric and isochoric responses are independent, a further additive decomposition of the strain energy function can be achieved by

$$\Psi(\mathbf{C}) = \bar{\Psi}(\text{I}_{\bar{\mathbf{C}}}, \text{II}_{\bar{\mathbf{C}}}) + \underbrace{\kappa \hat{\Psi}(J)}_{=U(J)}, \quad (3.7)$$

where κ is the bulk modulus that can be determined for isotropic materials based on the Young's modulus E and Poisson's ratio ν using the following

equation:

$$\kappa = \frac{E}{3(1 - 2\nu)}. \quad (3.8)$$

For the volumetric strain energy $\hat{\Psi}(J)$, numerous reliable formulations that satisfy the conditions in Equation 3.3 and convexity conditions have been proposed. Some of these formulations are listed in Table 3.1 (see [71] for further details).

Tab. 3.1: Reliable formulations of various volumetric strain energy functions.

Formulation for $\hat{\Psi}(J)$	
$\frac{1}{2}(J - 1)^2$	
$J - \ln J - 1$	[72]
$(J^{2p} + J^{-2p} - 2)^k, p \geq \frac{1}{2}, k \geq 1$	[71]
$(J - 1)^k, k \geq 1$	[71]

Moreover, it is likewise feasible to calculate alternative stress measures, including the second Piola-Kirchhoff stress tensor \mathbf{S} and the Cauchy stress tensor $\boldsymbol{\sigma}$ through the application of the following transformations:

$$\mathbf{S} = \mathbf{F}^{-1}\mathbf{P} \quad \text{and} \quad \boldsymbol{\sigma} = \frac{1}{J}\mathbf{P}\mathbf{F}^T. \quad (3.9)$$

It is also possible to decompose the second Piola-Kirchhoff stress into an isochoric component $\bar{\mathbf{S}}$ and a volumetric part $\hat{\mathbf{S}}$. For a strain energy function as given in Equation 3.7 both components can be determined using

$$\bar{\mathbf{S}} = \underbrace{2 \frac{\partial \bar{\Psi}(\bar{\mathbf{C}})}{\partial \bar{\mathbf{C}}}}_{=\bar{\mathbf{S}}} : \underbrace{J^{-2/3} \left[\mathbf{J}^S - \frac{1}{3} \mathbf{C} \odot \mathbf{C}^{-1} \right]}_{=\bar{\mathbf{P}}} \quad \text{and} \quad \hat{\mathbf{S}} = \frac{dU}{dJ} J \mathbf{C}^{-1}, \quad (3.10)$$

where $\bar{\mathbf{P}}$ is known as the isochoric projection tensor, $\mathbf{J}^S = (\mathbf{I} \otimes \mathbf{I})^S$ is the super-symmetric identity tensor and $\bar{\mathbf{S}}$ is the fictitious second Piola-Kirchhoff stress, see [69] for further details. The tensor $\bar{\mathbf{S}}$ can be calculated with

$$\bar{\mathbf{S}} = 2 \left(\frac{\partial \bar{\Psi}}{\partial \mathbf{I}_{\bar{\mathbf{C}}}} + \mathbf{I}_{\bar{\mathbf{C}}} \frac{\partial \bar{\Psi}}{\partial \Pi_{\bar{\mathbf{C}}}} \right) \mathbf{I} - 2 \frac{\partial \bar{\Psi}}{\partial \Pi_{\bar{\mathbf{C}}}} \bar{\mathbf{C}}. \quad (3.11)$$

3.2 Remarks on Implementation

In order to establish a framework that is capable of combining the continuum mechanical theory described in Section 3.1 with the concepts of symbolic

regression and genetic programming discussed in Chapter 2, it is necessary to incorporate the relevant constitutive equations. The available packages are designed to identify a direct mathematical relationship between inputs and an output. In the context of continuum mechanics, the inputs (e.g., the components of the deformation gradient) are not the direct arguments of the first Piola-Kirchhoff stress tensor \mathbf{P} . To perform the fitting, the strain energy density function must be identified based on the derivatives with respect to the invariants. Additionally, the strain energy density function cannot be obtained from experimental data, therefore only a stress value resulting from the differentiation can be utilized to assess the model performance.

The equations given in Section 3.1 are generally valid for isotropic hyperelastic nearly-incompressible as well as incompressible materials depending on the invariants $I_{\bar{\mathbf{C}}}$, $II_{\bar{\mathbf{C}}}$ and J . It is evident that this approach can be straightforwardly applied to generalized invariants. Consequently, only the strain energy density and its derivatives with respect to the invariants are material-dependent, and no material-specific modifications are required for proper alignment with symbolic regression. The utilization of this continuum mechanical framework with a symbolic regression extension offers a number of advantages:

1. The strain energy function obtained by symbolic regression is automatically in accordance with the material objectivity condition, as it is formulated in terms of objective invariants.
2. As the invariants are employed as input arguments, the user has the option to include only isotropic or anisotropic models within predefined symmetry classes.
3. In comparison to other data-driven models that directly relate a deformation tensor to a stress tensor, the scalar-valued strain energy function is obtained as an interpretable model. It is thus possible to determine completely novel models using SR based on the specified data.
4. Finite element codes provide programming interfaces in which material models can be implemented directly by the user. In certain instances, such as when utilizing the UHYPER or UMAT subroutine in ABAQUS, the strain energy density and its derivatives with respect to the invariants are necessary. These equations can be deduced with relative ease.

In addition to the invariants, the strain energy density functions permit dependence on any number of additional parameters, including, e.g., temperature or a specific concentration of material constituents. A schematic representation of the general process, incorporating both the invariants and $i = 1, \dots, n$ additional parameters κ_i is provided in Figure 3.1.

The strain energy is calculated on the basis of the stress-strain data obtained

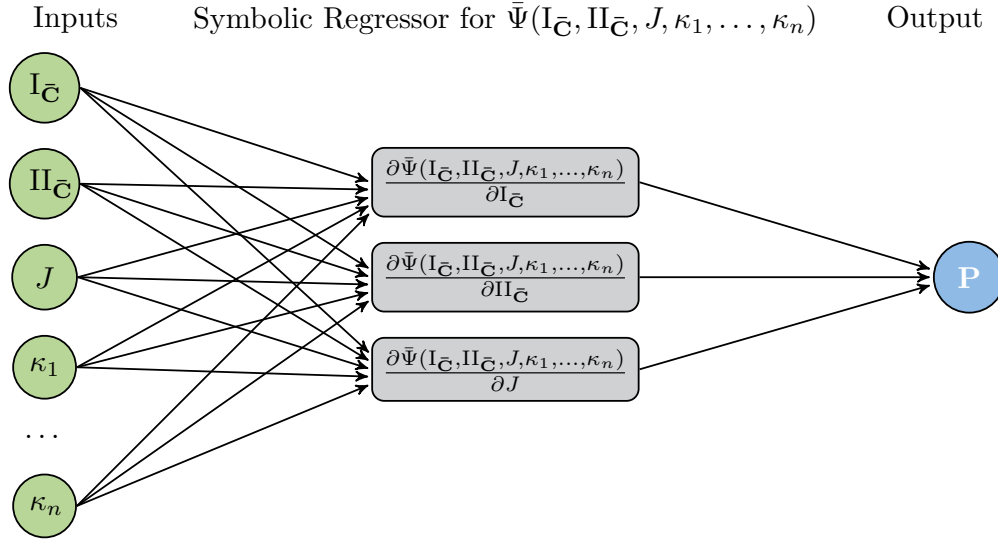


Fig. 3.1: Illustration of the symbolic regression procedure for novel model discovery. The inputs to the process include the invariants $I_{\bar{\mathbf{C}}}$, $II_{\bar{\mathbf{C}}}$, and J as well as additional parameters $\kappa_1, \dots, \kappa_n$. The output is the first Piola-Kirchhoff stress tensor \mathbf{P} . The symbolic regressor is tasked with deriving the strain energy function, where derivatives are computed with respect to the invariants and subsequently evaluated for the fitting.

from the primary loading subjected to different loading conditions. For this purpose, a user-defined loss function must be defined that calculates the derivatives of the strain energy function with respect to the specified invariants. The differentiation is performed numerically using the finite difference scheme. In order to conduct a comparison and validate the results, it is also possible to implement reverse-mode algorithmic differentiation by incorporating it into the call tree. This approach is currently 60.00 % less numerically effective than the numerical differentiation, with no noticeable improvement in the quality of the output. The primary reason for this is the implementation of the execution function for each expression within the DSO package. To further accelerate the process, several operations are vectorized using Numpy broadcasting. The loss function is evaluated based on the provided stress response and stresses calculated by Equation 3.1, Equation 3.5 or Equation 3.6. In this regard, the initial Piola-Kirchhoff stress tensor, as expressed in these formulas, appears to be highly advantageous, as it permits a direct comparison with the experimental stress response.

In the comparison with experimental or artificially created stress data, only derivatives of the strain energy functions are relevant. Consequently, the condition (3.3)₁ can be easily satisfied by a straightforward correction of the resulting expression by a constant. The fulfillment of (3.3)₂ is a direct consequence of the inclusion of the point $\mathbf{P} = \mathbf{0}$ at $\mathbf{F} = \mathbf{I}$ within the data set used for the search of the strain energy function. The basis functions for the strain

energy are provided in the following form: ["add", "sub", "n2", "mul", "div", "sqrt", "exp", "log"]. To enhance the reliability of the outcome, the final evaluation stage features a filter that rounds all decimal numbers to the second digit, thereby significantly simplifying the expressions that have been determined.

4 Benchmark Tests Using Artificial Data

All models are wrong, but some are useful.

G. E. P. Box

This chapter assesses the efficacy of the proposed framework through the implementation of a series of benchmark tests. It is crucial to evaluate the quality of the automatically generated material models through their ability to accurately interpolate and extrapolate data, as well as to assess the uniqueness or multiplicity of the obtained solutions. Furthermore, it is essential to determine the influence of data set size and input variables on the proper material characterization and the accuracy of the generated models.

Accordingly, the primary performance comparison is conducted using artificial data generated through the incompressible generalized Mooney-Rivlin model in three distinct complexity scenarios in Section 4.1. The advantage of utilizing artificial test data is that all evaluations are conducted within a controlled setting with known parameters, thereby ensuring the reliability and reproducibility of the results. Furthermore, the absence of noise in the data allows for a pure assessment of the model's theoretical performance, prior to the consideration of real-world factors that may introduce additional uncertainties. To identify the optimal framework for model identification, the evaluation is conducted using the `gplearn` and the `DSO` package. Furthermore, the performance of the presented approach is evaluated for the nearly incompressible Mooney-Rivlin model with two distinct implementations of the volumetric strain energy contributions in Section 4.2. An additional analysis in Section 4.3 discusses the impact of two different test-train splits. Finally, a benchmark using the stretch-based Ogden model is presented in Section 4.4. The proposed benchmarks for the Mooney-Rivlin models have been the subject of independent investigation in my previous publications [1, 4].

4.1 Incompressible Generalized Mooney-Rivlin Model

In this section, the two packages presented in Chapter 2, namely `gplearn` and `DSO`, will be evaluated on three different cases of complexity for a known

constitutive model. The advantages and disadvantages of both packages are examined in detail. The efficacy of symbolic regression can be effectively evaluated due to the prior availability of the ideal solution.

An appropriate constitutive model for this purpose is the incompressible generalized Mooney-Rivlin model [22, 73]. The model can be applied to a diverse range of rubber-like materials, serving as a reference point for evaluating the efficacy of both approaches in determining the expression of the strain energy function. The strain energy function Ψ_{gMR} for the generalized incompressible Mooney-Rivlin model is given by:

$$\Psi_{\text{gMR}} = \sum_{i=1}^3 \left[c_{i0} (\text{I}_{\mathbf{C}} - 3)^i + c_{0i} (\text{II}_{\mathbf{C}} - 3)^i \right], \quad (4.1)$$

where c_{i0} and c_{0i} represent material constants. In order to examine the effects of varying degrees of model complexity, a random sampling of the values of these constants was conducted, resulting in three cases of increasing model complexity. The values are randomly generated between 0.00 MPa and 1.00 MPa and are presented in Table 4.1 for the `gplearn` and `DSO` frameworks. The inputs for both frameworks are the first and second invariants $\text{I}_{\mathbf{C}}$ and $\text{II}_{\mathbf{C}}$ (since $J = 1$). The resulting output is the component P_{11} of the first Piola-Kirchhoff stress tensor.

Tab. 4.1: Randomly sampled material parameters between 0.00 MPa and 1.00 MPa for the generalized incompressible Mooney-Rivlin model for the `gplearn` and the `DSO` framework. Three cases of complexity are considered for both frameworks.

	Case	c_{10} [MPa]	c_{20} [MPa]	c_{30} [MPa]	c_{01} [MPa]	c_{02} [MPa]	c_{03} [MPa]
gplearn	1	0.48	-	-	0.12	-	-
	2	0.87	0.86	-	0.98	0.43	-
	3	0.91	0.57	0.79	0.88	0.21	0.70
DSO	1	0.63	-	-	0.39	-	-
	2	0.95	0.66	-	0.51	0.62	-
	3	0.73	0.43	0.1	0.99	0.97	0.32

In accordance with the methodology outlined Chapter 3, the material responses under uniaxial tension (UT), pure shear (PS), and equibiaxial tension (EBT) have been calculated for the three complexity cases as presented in Table 4.1. In all cases, a total of five formulations of the strain energy function were identified. This is a necessary step resulting from the randomized sampling process involved in GP, which has the potential to affect the efficacy of the population initialization procedure. Consequently, the mean response and standard deviation are calculated for each strain value of all five models. It

should be noted that only 50 data points were calculated for each of these loading cases. In order to assess the quality of the interpolation of the resulting expressions of the strain energy function, only the data within the strain interval between 0.00 % and 100.00 % were used for fitting, with an additional 80.00 % for training and 20.00 % for testing. The data in the strain interval between 100.00 % and 150.00 % are used to assess the extrapolation capacity of the resulting expressions.

4.1.1 Performance of `gplearn`

This section presents an evaluation of the performance of the `gplearn` package. The utilized hyperparameters, such as the number of generations or the population sizes, are listed in Table 4.2 for all cases of complexity. Figure 4.1 depicts the fitness plotted over generations, while Figure 4.2 illustrates the first Piola-Kirchhoff stress as a function of strain for all three loading cases. The default fitness in `gplearn` is the mean absolute error (MAE), which is calculated as follows:

$$\text{MAE} = \frac{1}{N} \sum_{i=1}^N |f(\mathbf{x}_i) - y_i| , \quad (4.2)$$

where N is the number of predicted values, $f(\mathbf{x}_i)$ is the prediction based on the inputs \mathbf{x}_i and y_i are the true values.

As the number of generations increases, the resulting fitness value exhibits a notable improvement for all five samples. As this is an evolutionary algorithm, the optimal strain energy function is not retained and may continue to mutate. In all cases, the maximum number of generations has been set to 50. It is noteworthy that the fitness begins to plateau as this limit is approached. It can be observed that differing initializations result in a diverse range of fitness values. The fitness value may be improved by increasing both the initial population size and the number of generations. As a consequence, this results in a considerable computational burden. It should be noted that the parameters presented in Table 4.2 were manually optimized and derived from general recommendations, without the additional step of hyperparameter optimization. Accordingly, it is plausible that optimizing the hyperparameters may result in a further reduction in fitness and the eventual generation of more accurate models.

In Figure 4.2 the mean responses for UT, PS, and EBT, along with the corresponding 6σ intervals, are illustrated. Here, σ represents the standard deviation. In the first complexity scenario, the accuracy of the obtained results is notably high in both the interpolation and extrapolation domains. However, as the complexity of the model increases, the precision of the approximation decreases. As the complexity of the models increases, the confidence interval widens for strains above 100.00 %, indicating a higher level of uncertainty. This

is due to the fact that an increase in model complexity leads to a greater number of terms in the polynomial function provided in Equation 4.1. The number of terms that must be identified is inversely proportional to the probability of their rapid discovery. The averaged predictions in the strain region between 0.00 % and 100.00 % are in close agreement with the corresponding provided responses. Moreover, based on the derived expressions, it can be concluded that the model is not unique for the highest complexity case.

A notable finding is that in the second complexity scenario, the pure shear response in the extrapolation region appears to diverge from the actual response. The mean response, as well as the confidence interval, indicates that the identified models overestimate the stresses. This suggests that the precise expressions have not been identified in all five samples, and that only an approximate model has been discovered for the interpolation region. In the third complexity case, the confidence interval in the extrapolation region for the PS and UT responses is notably larger, while the mean response remains relatively accurate. This is attributable to the occurrence of an outlier expression that was unable to accurately predict the stresses.

In theory, a perfect fit can be achieved with a very high number of generations and a high population size. Despite the limited number of data points utilized in the fitting process, the resulting accuracy is remarkably high. It is evident that the approach exhibits superior performance in the interpolation domain compared to the extrapolation region, which aligns with the established concept that the greater the magnitude of extrapolation, the larger the associated error, leading to wider confidence intervals.

Tab. 4.2: List of specified values of hyperparameters used in the `gplearn` package, categorized according to three different complexity cases.

Inputs	Case 1	Case 2	Case 3
population_size	1000	7500	15000
generations	50	50	50
stopping_criteria	0.001	0.001	0.001
p_crossover	0.7	0.7	0.6
p_subtree_mutation	0.15	0.15	0.15
p_hoist_mutation	0.1	0.1	0.1
p_point_mutation	0.05	0.05	0.15
max_samples	0.9	0.9	0.9
parsimony_coefficient	0.003	0.003	0.0005

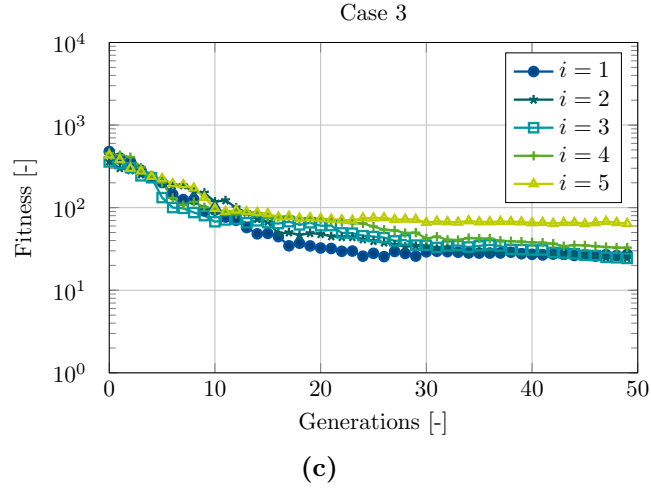
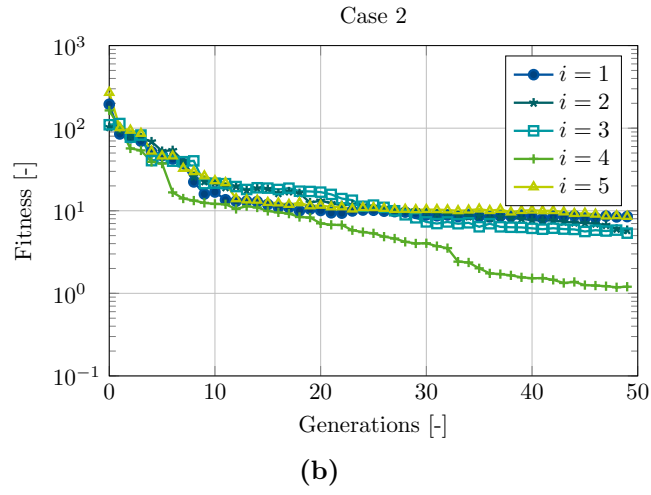
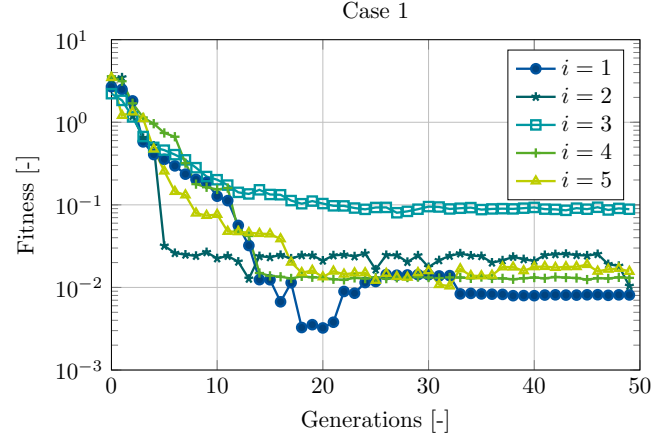


Fig. 4.1: Visualization of the fitness evolution over the number of generations for the incompressible generalized Mooney-Rivlin model across all five samples i . The comparison includes all three complexity cases as described in Table 4.1.

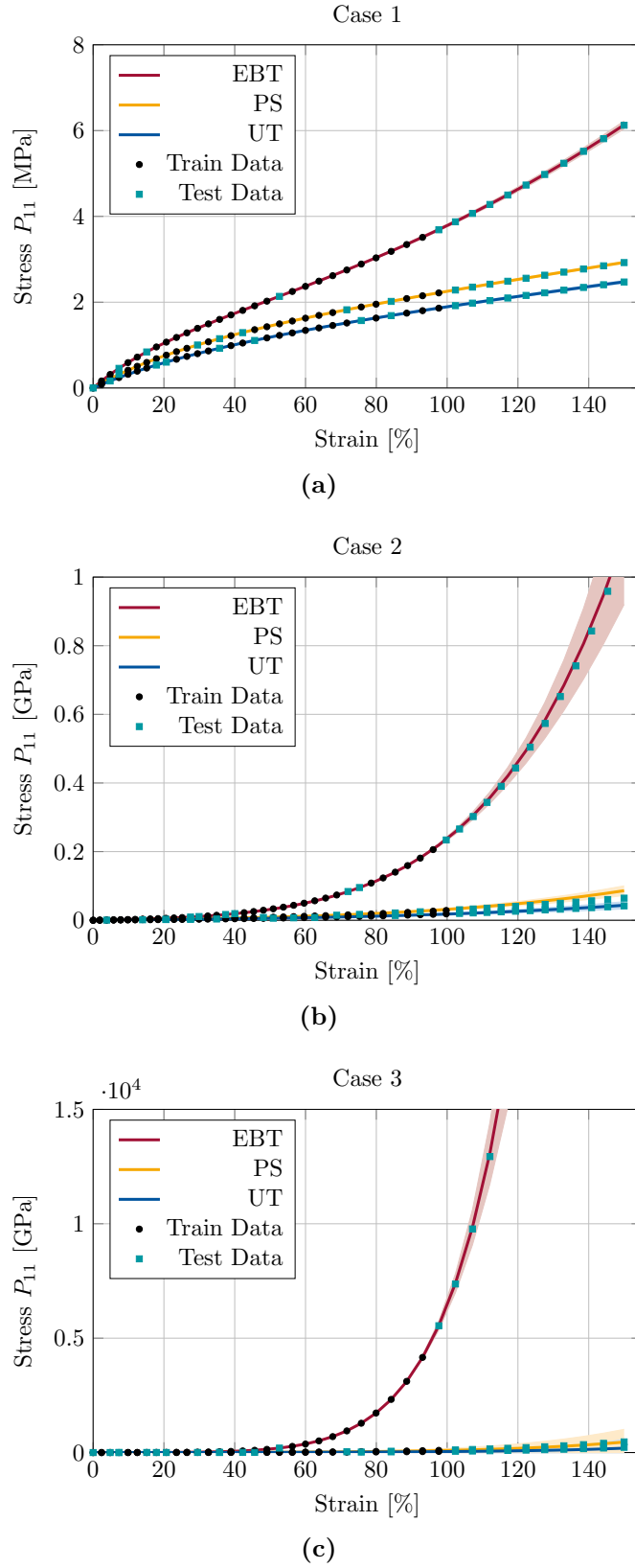


Fig. 4.2: Mean stress-strain response of all models obtained using `gplearn`, with corresponding train and test data (UT, PS and EBT) based on the generalized Mooney-Rivlin model. Shaded areas indicate 6σ confidence intervals.

4.1.2 Performance of DSO

The performance of the strain energy functions identified by DSO can be observed in Figure 4.3, where the resulting stress-strain curves are plotted along with the training and test data. As in the previous example, five expressions of the strain energy function are determined. The visualized predictions correspond to the average response of all five resulting models. In addition, the 6σ confidence intervals are shown in these plots as colored enclosures of the curves.

An interesting observation is that the recovery rate of the underlying strain energies is 100.00 % for the first two cases and 0.00 % for the last case, despite the fact that all models have an R^2 score exceeding 99.98 %. The 0.00 % recovery rate in combination with a R^2 score nearly to 100.00 % indicates that the derived expressions are approaching an alternative formulation of the strain energy function, which is plausible given the high nonlinearity of the problem, particularly in the last complexity case of the generalized Mooney-Rivlin model. For a discussion of such nonuniqueness, for example in the context of the Ogden model, the reader is directed to [74]. Nevertheless, close approximations can be identified that accurately describe the data sets generated by these models. It is also noteworthy that the extrapolation quality of the underlying models is excellent despite the limited number of training data points. The confidence interval is negligible in all cases, except for the last case under UT, which is also reflected in the high R^2 scores. Therefore, the proposed framework demonstrates robust performance by extrapolating and interpolating the sparse data provided for all three complexity cases and three different loading conditions.

4.1.3 Conclusion

The two symbolic regression frameworks demonstrate high efficacy in interpolating and extrapolating stress responses under the incompressible generalized Mooney-Rivlin model. Nevertheless, the results of this preliminary benchmark analysis indicate that the DSO approach consistently outperforms `gplearn`. The confidence intervals are consistently smaller in all complexity cases, indicating that the DSO package is more effective at generalizing predictions when presented with unseen test data. In terms of computational efficiency, `gplearn` demonstrates a slight advantage due to the application of the constant optimization process within the DSO package. Nevertheless, the DSO package provides an additional benefit through the implementation of a genetic programming loop optimizer. In this manner, the approach combines the methodologies of both recurrent neural networks and genetic programming, thereby establishing a mixed approach for exploring and deriving potential expressions for the strain energy.

The highest-performing expressions, as identified for both frameworks, are pre-

sented in Table 4.3. Both approaches demonstrate high accuracy in identifying the underlying model, particularly in the simplest complexity scenario. However, as the complexity of the models increases, both frameworks demonstrate a notable decline in the recovery rate. This can be attributed to the high degree of nonlinearity and existence of multiple solutions. It is noteworthy that the constants c_{i0} and c_{0i} exhibit only marginal discrepancies in their decimal digits when compared to the original values.

Tab. 4.3: Best performing expressions for the generalized incompressible Mooney-Rivlin model, obtained using the `gplearn` and `DSO` frameworks, across all three complexity cases. Additionally, the mean absolute error (MAE) and R^2 scores are provided.

	Case	Strain energy	MAE \ R^2
gplearn	1	$\Psi_{\text{gMR}} = 0.48\text{I}_{\text{C}} + 0.12\text{II}_{\text{C}} - 0.01$	0.01
	2	$\Psi_{\text{gMR}} = \text{I}_{\text{C}} (0.11\text{I}_{\text{C}}\text{II}_{\text{C}} + 0.02\text{II}_{\text{C}} - 1) - \text{II}_{\text{C}}(0.23\text{I}_{\text{C}} + 0.02) \exp(-.30\text{II}_{\text{C}}) + 0.11\text{II}_{\text{C}} \exp(-.74\text{II}_{\text{C}}) + \exp(\text{I}_{\text{C}} - 1.75\text{II}_{\text{C}})$	1.20
	3	$\Psi_{\text{gMR}} = \exp(413.40 \exp(-1.79\text{II}_{\text{C}})) \left(0.20\text{I}_{\text{C}}^2\text{II}_{\text{C}}^2 - 0.95\text{I}_{\text{C}}^2\text{II}_{\text{C}} + 1.11\text{I}_{\text{C}}^2 - 0.48\text{I}_{\text{C}}\text{II}_{\text{C}}^2 + 2.27\text{I}_{\text{C}}\text{II}_{\text{C}} - 2.66\text{I}_{\text{C}} + 0.29\text{II}_{\text{C}}^2 - 1.36\text{II}_{\text{C}} + 1.60 \right)$	24.28
DSO	1	$\Psi_{\text{gMR}} = 0.63\text{I}_{\text{C}} + 0.39\text{II}_{\text{C}} + 0.39$	1.00
	2	$\Psi_{\text{gMR}} = 0.66\text{I}_{\text{C}}^2 - 3.01\text{I}_{\text{C}} + 0.62\text{II}_{\text{C}}^2 - 3.21\text{II}_{\text{C}} + 1$	1.00
	3	$\Psi_{\text{gMR}} = \frac{\text{I}_{\text{C}} (0.09\text{I}_{\text{C}}^2 \ln(\text{I}_{\text{C}}) + 0.07\text{II}_{\text{C}})}{(0.25\text{II}_{\text{C}} - 0.22)^{-1} 0.77\text{II}_{\text{C}}} + \frac{\text{II}_{\text{C}} (\text{II}_{\text{C}} - 2.67) (\text{II}_{\text{C}} - 2.43)}{(0.25\text{II}_{\text{C}} - 0.22)^{-1} 0.77\text{II}_{\text{C}}}$	1.00

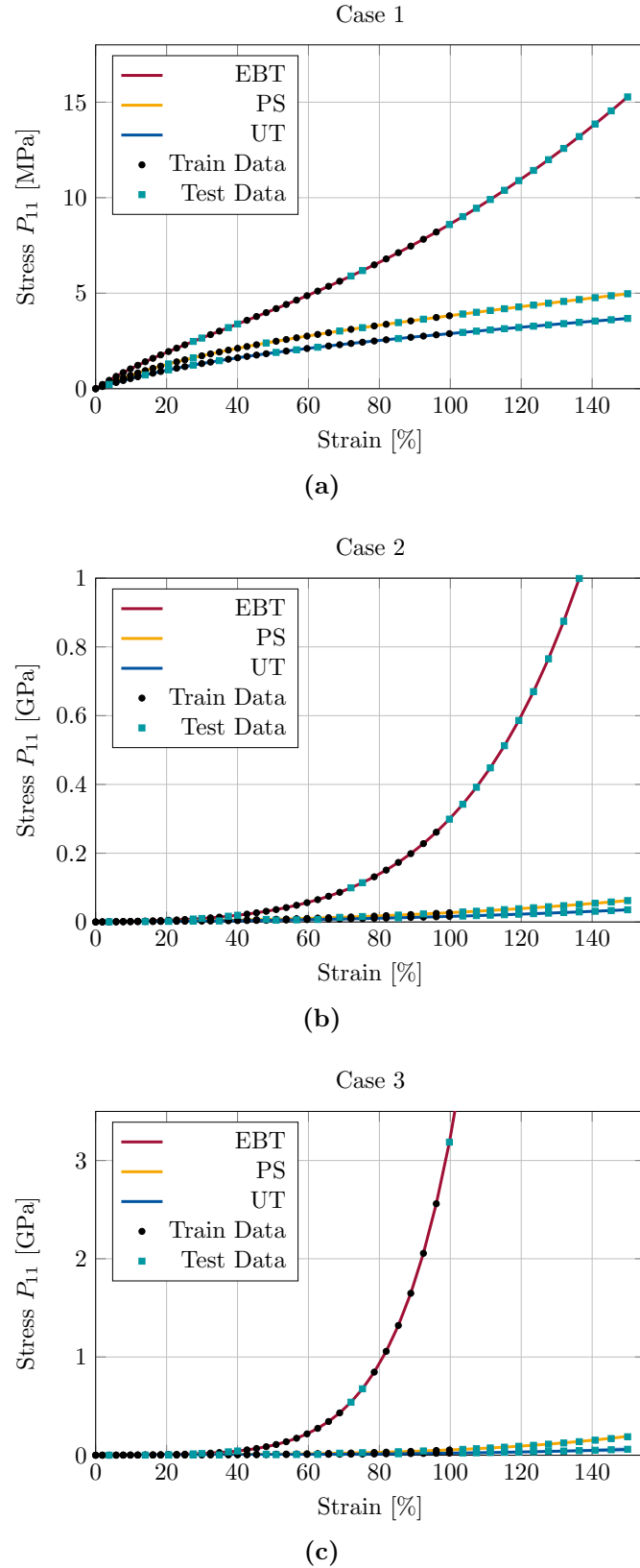


Fig. 4.3: Mean stress-strain response of all models obtained using DSO, with corresponding train and test data (UT, PS and EBT) based on the generalized Mooney-Rivlin model. Shaded areas indicate 6σ confidence intervals.

4.2 Nearly Incompressible Mooney-Rivlin Model

The volumetric-isochoric split of the strain energy function, as described in Equation 3.7, is a crucial tool, particularly for FE simulations. Consequently, it is worthy of a dedicated investigation. In this section, two distinct volumetric functions will be evaluated. The analysis is conducted exclusively with the DSO package. The isochoric component of the strain energy for the Mooney-Rivlin model is represented by

$$\bar{\Psi}_{\text{gMR}} = c_{10} (\text{I}_{\bar{\mathbf{C}}} - 3) + c_{01} (\text{II}_{\bar{\mathbf{C}}} - 3) . \quad (4.3)$$

The same constants as in the first complexity case for the DSO package, as referenced in Table 4.1, are utilized for the following analysis. In regard to the volumetric response, a classical quadratic function in J is applied, in addition to an expression proposed by Miehe [72]. The resulting formulations are as follows:

$$\hat{\Psi}_1 = \frac{1}{2} \kappa_1 (J - 1)^2 \quad \text{and} \quad \hat{\Psi}_2 = \kappa_2 (J - \ln J - 1) . \quad (4.4)$$

The constants $\kappa_1 = 50.00$ MPa and $\kappa_2 = 65.00$ MPa are defined in such a way that the equibiaxial tension response of the two volumetric energies is equal at a strain of 150.00 %. Once more, a total of five strain energy functions are sampled, and the mean stress-strain responses of all models with the corresponding training and test data for UT, PS, and EBT for the two different volumetric strain energy functions are presented in Figure 4.4. The colored enclosures surrounding the curves illustrate the 6σ confidence intervals associated with the predictions. It is evident that the stress-strain response is accurately described for both formulations in the interpolation region. However, for the second formulation, a larger confidence interval is visible for the EBT response in the extrapolation region. As with the previously discussed case, this result indicates that the selected volumetric contributions are not unique formulations for describing the stress-strain data.

In both instances, the values of the R^2 score exceeded 99.70 % for all five models obtained using the DSO package. It is noteworthy that the recovery rate of the volumetric functions is 60.00 % for the first formulation and 0.00 % for the second. Therefore, only approximate solutions have been identified. In the applied procedure, both the isochoric and volumetric strain energies were simultaneously sought. A reasonable alternative for numerical applications would be to directly specify a numerically stable volumetric strain energy and identify only the isochoric contribution. Furthermore, it is notable that the isochoric components are correctly identified for four out of the five samples in the first formulation. In the second case, the isochoric components could not be fully recovered.

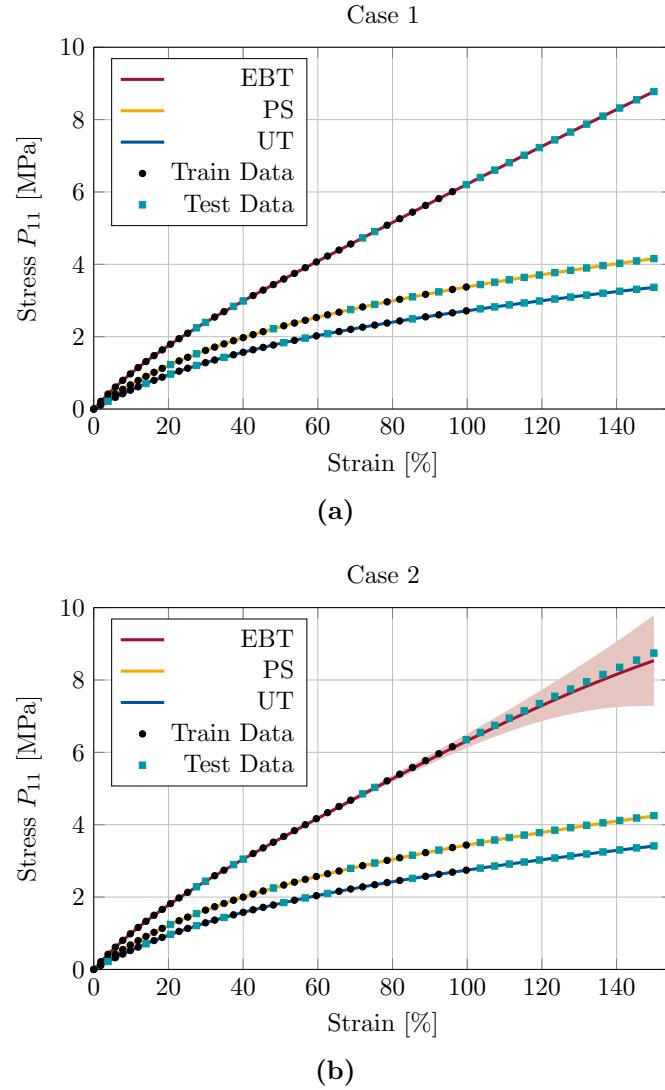


Fig. 4.4: Mean stress-strain response of all five models obtained using DSO, alongside the corresponding training and test data for UT, PS and EBT for the two different volumetric strain energy functions in Equation 4.4. Shaded areas indicate 6σ confidence intervals.

4.3 Influence of Train-Test Data Splits

The following section examines the reliability of the approach utilizing the DSO package across various test-train splits. To this end, a split with 70 to 30.00 % and 60 to 40.00 % of train and test data, respectively, are compared. The results for each complexity scenario are presented in Figure 4.5 and Figure 4.6. In all cases, the achieved R^2 scores exceed 99.98 %. Even for the case of 60 to 40.00 % train-test split, all models capture the underlying material behavior well. Furthermore, the recovery rates remain consistent across different levels of complexity for both split cases where in the first two and the last case

the recovery rates are 100% and 0%, respectively. Furthermore, it is evident that in the case of the 60 to 40.00 % train-test split, the confidence interval exhibits a notable expansion within the range of strains exceeding 100.00 %, suggesting an overfitting of the data within the interpolation region. The outcome may be anticipated, given the restricted quantity of training data. In conclusion, the preliminary investigation indicates that the framework demonstrates exceptional performance even in circumstances of extreme data scarcity.

4.4 Remarks on Stretch-Based Ogden Model

As introduced in Chapter 3, while the proposed framework uses invariants, it is also feasible to evaluate performance using a stretch-based formulation. A particularly reliable model developed by Ogden has gained wide acceptance in industrial FE software and has demonstrated excellent performance [75]. The basic premise of this model is to describe the strain energy function in terms of the principal stretches λ_i , expressed as

$$\Psi(\lambda_1, \lambda_2, \lambda_3) = \sum_{i=1}^N \frac{\mu_i}{\alpha_i} (\lambda_1^{\alpha_i} + \lambda_2^{\alpha_i} + \lambda_3^{\alpha_i} - 3), \quad (4.5)$$

where N , μ_i , and α_i are material constants. A notable limitation of this approach is that already for $N = 3$ a total of six material parameters are required. The Ogden model adheres to the Valanis-Landel assumption [76], which states that the strain energy of an isotropic material can be represented by a single, continuously differentiable function ω by

$$\Psi(\lambda_1, \lambda_2, \lambda_3) = \omega(\lambda_1) + \omega(\lambda_2) + \omega(\lambda_3). \quad (4.6)$$

To ensure that the conditions of zero energy and stress-free state in the reference configuration are met, this function must satisfy the following criteria:

$$\omega(1) = 0 \quad \text{and} \quad w'(1) = 0.$$

In the following, the Valanis-Landel assumption is used to identify a strain energy function using the DSO framework. It should be noted that the basis list of functions has been augmented with the incorporation of the power function ["pow"] for this example. The function ω is determined and expressed as the sum of the three principal stretches, thereby defining the strain energy Ψ . A benchmark analysis is conducted using the Ogden model with the specified material parameters $N = 1$, $\mu_1 = 0.63$ MPa, and $\alpha_1 = 1.71$. In this case, a train-test split of 80.00 % to 20.00 % is implemented for the strain range up to 100.00 %. An additional region is investigated for strains up to 150.00 % for assessing the extrapolation capabilities. Given that the results are once

more dependent on the arbitrary initialization of the generated expressions, five samples are selected for analysis. Figure 4.7 depicts the stress-strain response in addition to the training and test data for the identified strain energy functions. The visual representation of the predictions depicts the mean response of all five models, accompanied by an additional 6σ confidence interval, which is illustrated as colored enclosures around the curves. Table 4.4 provides a list of the identified models. It is noteworthy that the recovery rate was 100.00 %, with the R^2 scores exceeding 99.99 %. This illustrates that the presented approach operates with high accuracy even when provided with a limited number of data points. It can therefore be concluded that a stretch-based formulation is similarly viable for identifying strain energy functions.

Tab. 4.4: Recovered functions ω for the Ogden model, along with their corresponding R^2 scores.

Case	Function ω	R^2
1	$\omega(\lambda) = 0.37\lambda^{1.71} - 0.37$	1.00
2	$\omega(\lambda) = 0.37\sqrt{\lambda^{3.42}}$	1.00
3	$\omega(\lambda) = 0.37 \left(\lambda^4 \sqrt{\lambda^2} \right)^{1.14}$	1.00
4	$\omega(\lambda) = 0.37\lambda^{1.71}$	1.00
5	$\omega(\lambda) = \frac{1}{4} \ln \left(2.46^{1.64\sqrt{\lambda^{3.42}}} \right)$	1.00

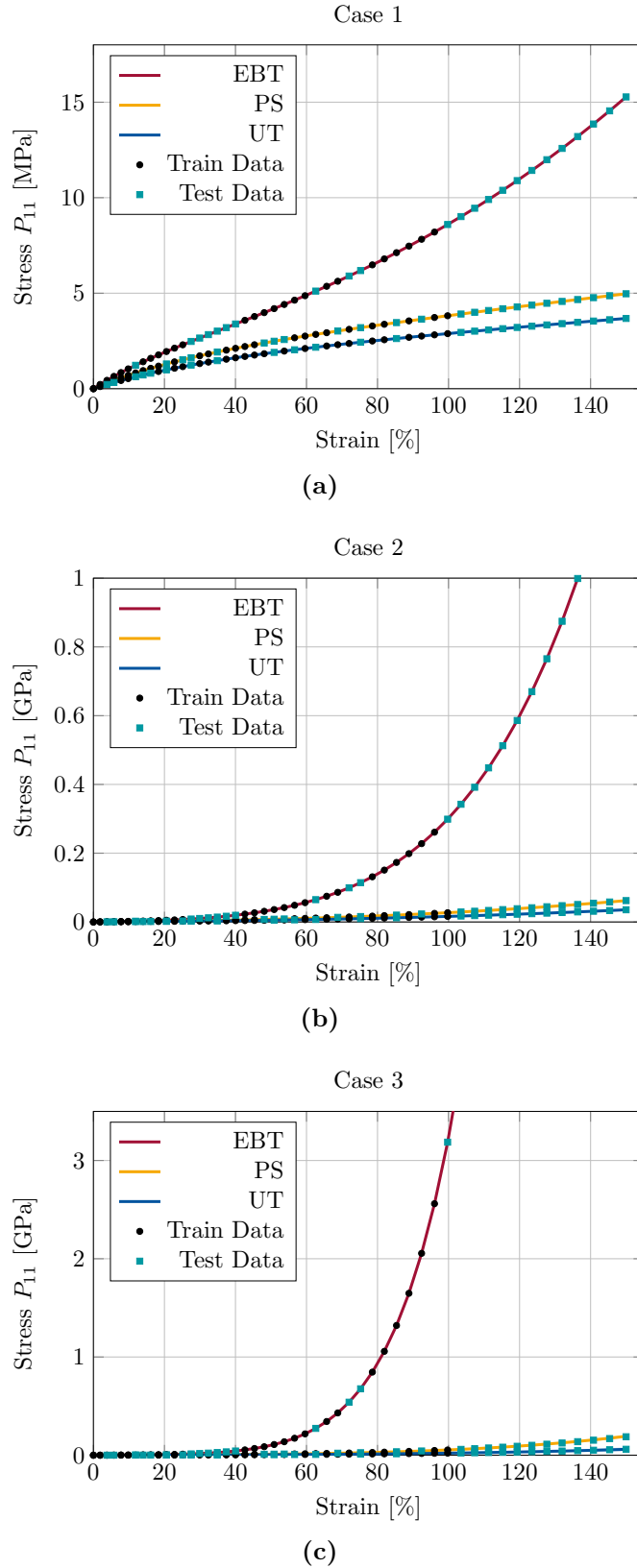


Fig. 4.5: Mean stress-strain response of all models using DSO, with corresponding train and test data (UT, PS, EBT) based on the generalized Mooney-Rivlin model for a 70.00 %/30.00 % train-test split. Shaded areas indicate 6σ confidence intervals.

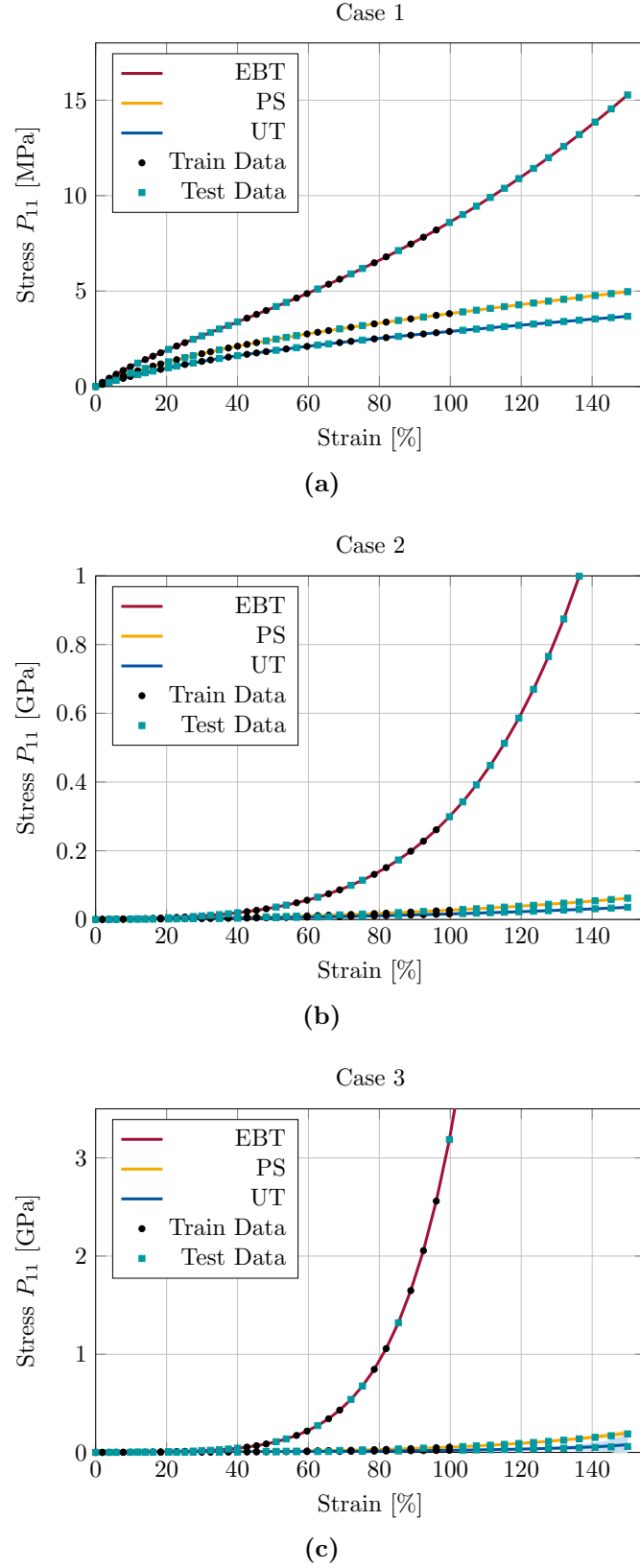


Fig. 4.6: Mean stress-strain response of all models using DSO, with corresponding train and test data (UT, PS, EBT) based on the generalized Mooney-Rivlin model for a 60.00%/40.00% train-test split. Shaded areas indicate 6σ confidence intervals.

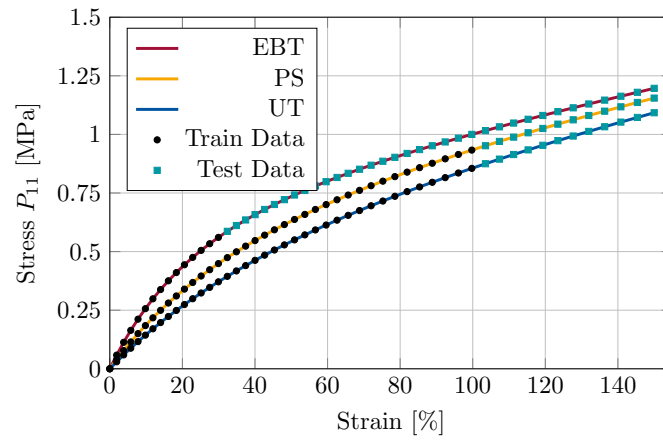


Fig. 4.7: Mean stress-strain response of all models using DSO, with corresponding train and test data (UT, PS, EBT) for the stretch-based Ogden model. Shaded areas indicate 6σ confidence intervals.

5 Benchmark Tests Using Experimental Data

All my money has been invested into experiments with which I have made new discoveries enabling mankind to have a little easier life.

N. TESLA

A crucial objective is to evaluate the efficacy of the proposed conceptual framework by benchmarking its performance on experimental data. In this regard, an essential benchmark is the data set presented by Treloar, which focuses on the multi-axial loading of vulcanized rubber. This data set is analyzed under the influence of noise to evaluate the uniqueness of the resulting strain energy functions in Section 5.1. Subsequently, the performance of the derived models is compared to that of classical constitutive approaches. In Section 5.2, some remarks are made on a stretch-based approach for describing the multi-axial loading of vulcanized rubber. Moreover, the experimental investigations of vulcanized rubber conducted by Kawabata et al. will be examined by analyzing the performance of different data set inputs in Section 5.3 [77]. Additionally, a data set that includes temperature-dependent effects for the thermoplastic polyester elastomer Hytrel 4556 will be tested in Section 5.4. The interpretability advantages of the proposed methodology are likewise examined in this context. Parts of the last section have been previously presented in my published work [4].

5.1 Multi-Axial Loading of Vulcanized Rubber

Natural rubber (NR) is a crucial raw material used in the automotive and tire industries. It fulfills a multitude of performance requirements, including durability, safety, weight reduction, and fuel efficiency. The distinctive properties of NR are attributed to a process known as vulcanization, a chemical process first discovered by Charles Goodyear in 1839 [78]. This process significantly enhances the mechanical properties of rubber, resulting in a material that is stiffer, stronger, more resistant to swelling and abrasion, and elastic over a wider range of temperatures. The search for suitable material models for rubber was initiated with Treloar's pioneering work in the 1940s. He investigated the general properties of rubber, developed a thermodynamic analysis

of rubber networks, and made a significant contribution to the understanding of the underlying physics of this complex material [79]. In 1944, he published a comprehensive data set on stress-strain characteristics of natural rubber, obtained from a variety of experimental setups, including those measuring the properties of the rubber under the conditions of UT, EBT, and PS [80]. This data set has become one of the most well-known and frequently utilized in the scientific community. It continues to serve as a crucial benchmark for evaluating constitutive models of rubber and rubber-like materials, as evidenced by the extensive literature on the subject, including [81–83] as well as references therein.

In the following analysis, the DSO package is employed to identify an optimal strain energy function for characterizing the Treloar data set. The data will be divided into a training (80.00 %) and a test set (20.00 %). Subsequently, the efficacy of the identified strain energy functions will be evaluated in comparison to established models, as referenced in [82, 84, 85]. Moreover, an investigation will be conducted to assess the robustness of the identified strain energy functions in the presence of noise. To identify an appropriate material model, it is not sufficient to fit each of the three curves individually. It is essential to consider all three curves simultaneously. To ensure the integrity of the analysis, the data set under examination contains 14 data points for the EBT, 14 data points for the PS, and 25 data points for the UT response. Given the significant difference in the number of data points for the EBT and UT responses, a straightforward approach is to duplicate the data set and assign greater weight to the EBT response. To evaluate the impact of noise, two distinct levels are tested given by

$$n_i(\lambda) = a_i \frac{\lambda}{\lambda_{\max}} \mathcal{N}(0, 1), \quad (5.1)$$

where $\mathcal{N}(0, 1)$ is the normal distribution, a_i is the amplitude level, λ is the current stretch and λ_{\max} is the maximum stretch. Accordingly, the noise level is proportional to the amplitude, the current strain, and is normalized to the maximum stretch. Two distinct amplitude levels $a_1 = 0.025$ MPa and $a_2 = 0.05$ MPa will be examined in this investigation.

As reported in [82] the Treloar data set can be fitted using the Mooney-Rivlin model where the material constants have been determined with $c_{10} = 1.62 \times 10^{-1}$ MPa and $c_{01} = 5.90 \times 10^{-3}$ MPa, see Figure 5.1 for the stress-strain response. It is evident that the EBT response accurately depicts the fundamental data. However, the responses for UT and PS are for strains greater than 400.00 %, significantly underestimating the observed stress-strain behavior. An effective material model should demonstrate a consistent performance across all three responses.

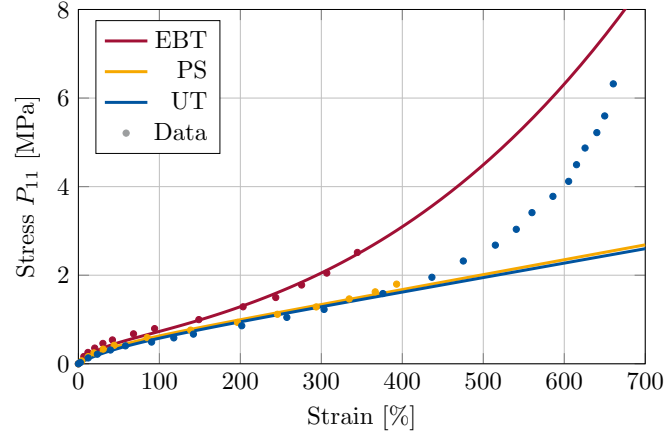


Fig. 5.1: Best fit for the Treloar data set using the Mooney-Rivlin model, with parameters $c_{10} = 1.62 \times 10^{-1}$ MPa and $c_{01} = 5.90 \times 10^{-3}$ MPa as given in Equation 5.2.

Using the DSO framework, the best performing strain energy Ψ_T is given by

$$\begin{aligned} \Psi_T = & \underbrace{0.13 I_C}_{\Psi_1} + \underbrace{2.40 \times 10^{-3} II_C}_{\Psi_2} + \underbrace{2.00 \times 10^{-3} \exp \sqrt{I_C}}_{\Psi_3} \\ & + \underbrace{2.76 \times 10^{-2} \left((\ln I_C)^2 + (\ln II_C)^2 \right)}_{\Psi_4}. \end{aligned} \quad (5.2)$$

The resulting formulation demonstrates a high degree of predictive power, as evidenced by an R^2 score of 97.32 %. Figure 5.2 illustrates the UT, PS, and EBT responses of this hyperelastic model. As this model can be decomposed

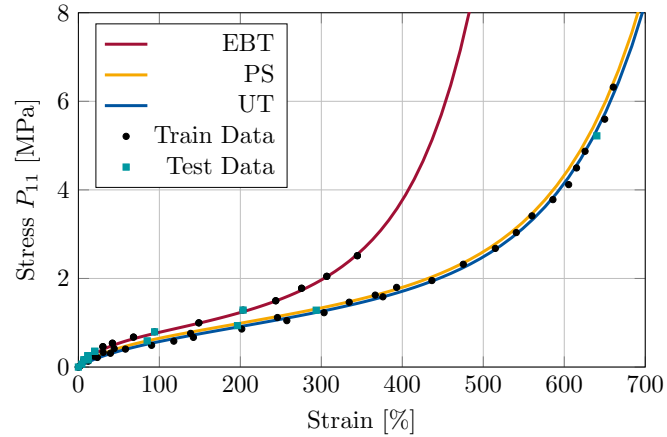


Fig. 5.2: Best fit for the Treloar data set of novel model discovered through DSO. The stress-strain responses for UT, PS and EBT are generated from the strain energy function given in Equation 5.2.

additively, the impact of each term Ψ_i can be visualized for the responses UT, PS and EBT. This is depicted in Figure 5.3. The predicted response for UT, PS as well as EBT is almost perfect throughout the whole interpolation and extrapolation range. A more detailed illustration of the strain ranges between 0.00 % and 300.00 % is presented in Figure 5.4. Upon analysis of the strain domain from 0.00 % to 700.00 %, it becomes evident that the first and third terms are of paramount importance for both UT and PS responses. It is noteworthy that, in the case of an EBT response, the second term also plays a crucial role. Nevertheless, within the strain domain from 0.00 % to 300.00 %, it is evident that all four terms contribute significantly to the EBT response. Interestingly, this strain energy function can be split up into four additive contributions: the first term Ψ_1 can be interpreted as a basic neo-Hookean response that solely depends on the first invariant. This term plays a pivotal role in the UT and PS responses, particularly within the range of small strains up to 300.00 %. The second term Ψ_2 is an additional correction term that depends on the second invariant. This term is a particularly significant contributing factor for strains exceeding 300.00 %, resulting in a markedly more rigid response in the EBT response. The third term Ψ_3 is an exponential function that depends on the first invariant. This contribution is of particular significance when the strain range exceeds 300.00 % for all loading cases, resulting in a notable stiffer response for large strains. It can thus be reasonably concluded that an exponential function was selected, given that it is multiplied by a significantly low coefficient. The last term Ψ_4 is a logarithmic function that depending on both invariants. This term is of particular importance with regard to the EBT response for the strain range between 0.00 % and 300.00 %.

Rivlin and Saunders observed in their 1951 experiments with a comparable rubber that the term $\partial\Psi/\partial\mathbf{I}_C$ in the strain energy function Ψ is independent of both \mathbf{I}_C and \mathbf{II}_C , while $\partial\Psi/\partial\mathbf{II}_C$ is independent of \mathbf{I}_C and decreases with an increase in \mathbf{II}_C [86]. In light of these observations, they proposed a function of the form:

$$\Psi_T = c_{10} (\mathbf{I}_C - 3) + \Phi (\mathbf{II}_C - 3) , \quad (5.3)$$

where c_{10} represents a constant, while Φ denotes a function with a continuously decreasing slope when \mathbf{II}_C increases. Based on this work, Gent and Thomas proposed a strain energy formulation wherein this function is expressed as a logarithmic function of \mathbf{II}_C with

$$\Phi = c_{01} \ln \left(\frac{\mathbf{II}_C}{3} \right) , \quad (5.4)$$

where c_{01} is a constant. The strain energy function presented in Equation 5.2 appears to reflect this underlying logic, as evidenced by the term Ψ_4 . However,

the refined function is markedly more intricate and nonlinear in character than the classical models that have been proposed for Φ . It is a considerable challenge for human intuition to successfully identify such a contribution. This term has a significant impact on the EBT response, while its influence on the UT and PS responses is minimal.

The found material model is a more accurate representation of the data set than many traditional hyperelastic models and requires only four material constants. Marckmann and Verron provide a summary and comparative analysis of twenty different models based on their ability to fit the experimental data for the Treloar data set [82]. A comprehensive investigation was conducted to identify the optimal performing models under identical loading conditions, specifically UT, PS, and EBT. In the course of their investigation, it was observed that the extended-tube model exhibited the best performance characteristics among all the models under consideration [24]. The model likewise features a minimalistic set of four material parameters, exhibiting robust predictive capabilities across a spectrum of loading scenarios. Furthermore, the findings indicated that the non-hyperelastic Shariff and unit sphere models demonstrated a high level of accuracy [87, 88]. However, these models are less commonly used in industrial applications compared to the extended-tube model. As listed in Table 5.1, a comparison of the R^2 scores of the proposed model discovered using DSO with those of the alternative approaches is provided. Furthermore, the Ogden model is capable of accurately predicting the underlying responses. Nevertheless, the Ogden model requires six material parameters, which makes it less practical for applications with limited experimental data. Models with fewer parameters, such as the three-chain, Hart-Smith, and eight-chain models, are unable to accurately predict the stress response over the entire strain range. It is noteworthy that in their analysis, they identified that for moderate strains of up to 200.00 - 250.00 %, the two-parameter Mooney-Rivlin model demonstrated the greatest efficacy, exhibiting performance characteristics comparable to those of more complex models. For small strains up to 150.00 %, the neo-Hookean constitutive equation is the preferred choice due to its physical basis, simplicity with a single parameter, and ability to predict material response over a range of loading conditions. These conclusions are supported by the identified strain energy function. The terms Ψ_1 and Ψ_2 serve as the fundamental building blocks for the neo-Hookean constitutive equation and the two-parameter Mooney-Rivlin model. As illustrated in Figure 5.4, these contributions are most significant for the small and moderate strain ranges up to 250.00 %.

Additionally, Ricker and Wriggers conducted a comprehensive study in which they fitted and compared a range of hyperelastic models for nine distinct rubber compounds, in addition to evaluating how these models performed when applied to the classical Treloar data set [84]. It was concluded that across different rubber compounds, models with three to five parameters generally perform best. The investigation focused on identifying the role and importance

of the second principal invariant for rubber models. Based on the findings, it was determined that UT is mainly influenced by the first invariant, while EBT and PS responses are equally affected by both invariants. Consequently, test data from a single experiment cannot adequately calibrate models dependent on both invariants, I_C and II_C . Furthermore, the utilization of solely I_C -based models results in an underestimation of the EBT response. By incorporating an additional II_C dependency, it is possible to achieve a balance in the stress response across diverse deformation modes and to offset potential limitations. These findings substantiate the observations made with the predicted material model by DSO. A significant benefit of the proposed methodology is that it does not necessitate an initial screening of any models, thereby preventing any potential for bias in model selection. The underlying relationships must be directly identified from the specified data and inputs.

A further question arises concerning the quality of the data set provided and its impact on performance. Accordingly, two distinct levels of noise are incorporated into the experimental data set. This leads to two central questions: first, to determine whether the derived strain energy function is a unique solution, and second, to explore the robustness of the prediction in the presence of noise. The analysis identified the optimal strain energy function $\Psi_{\text{Treloar}}^{n1}$ under the initial noise level as follows:

$$\Psi_{\text{Treloar}}^{n1} = \frac{\ln I_C + 28.42}{-0.03I_C + 1.13 - \frac{19.64 \exp\left(7.57 \exp\left(0.02\sqrt{I_C} - \frac{1}{\sqrt{II_C}}\right) - 16.15\right)}{I_C}}. \quad (5.5)$$

The best strain energy function obtained under the second noise level $\Psi_{\text{Treloar}}^{n2}$ is given by

$$\begin{aligned} \Psi_{\text{Treloar}}^{n2} = & 0.09I_C + 0.11\sqrt{II_C} + 0.11 \exp 0.60\sqrt{0.75II_C - 1} \\ & + \exp(0.07 \exp[\exp(0.02I_C)]) . \end{aligned} \quad (5.6)$$

The non-uniqueness of the obtained strain energy is evident due to the direct effect of the introduced noise on the data. For illustrative purposes, the stress-strain response for both models is presented in Figure 5.5. In particular, the strain energy function corresponding to the first noise level is observed to accurately describe both the PS and UT responses. However, it is noted that the EBT response is slightly underestimated. Despite this discrepancy, the derived model captures the underlying data set with a high accuracy and a R^2 score of 98.19 %. The second noise level formulation exhibits comparable patterns of behavior where the level of accuracy is given by a R^2 score of 97.15 %. In this instance, the PS and UT responses demonstrate a high degree of similarity, while the EBT response is subject to an underestimation. This may be attributed to the occurrence of data overlap within the strain range of 0.00 % to 200.00 %, which is a direct result of the noise introduced during the

process. Furthermore, this data overlap appears to result in a noticeably softer PS response in comparison to the first noise level for strains higher 300.00 %. This investigation demonstrates the significance of obtaining accurate experimental data. Additionally, the results indicate the availability of numerous feasible functions capable of describing the underlying data set. While there is no guarantee of a function that can be decomposed additively, the derived models effectively and accurately fitted the provided stress-strain responses despite the sparsity of the data.

Tab. 5.1: Comparison of the proposed model with existing approaches with respect to the number of material constants and the R^2 score for the Treloar data for each model.

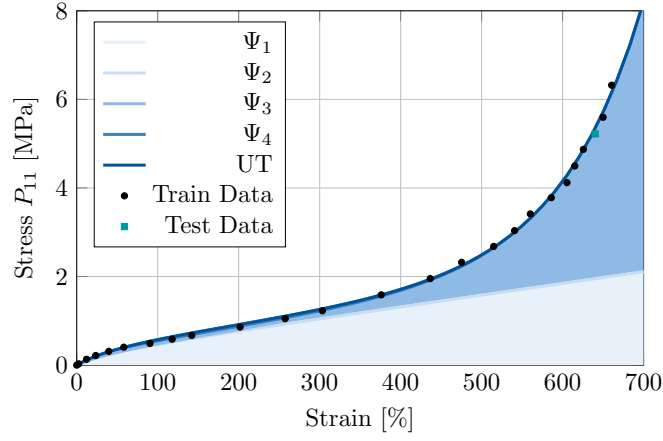
Model	Number of material constants	R^2 score
Proposed DSO	4	97.32 %
Extended tube [24]	4	96.56 %
Non-hyperelastic Shariff [87]	5	96.38 %
Ogden model [75]	6	95.58 %

Tab. 5.2: Material parameters of the extended tube model [24] for the Treloar data set.

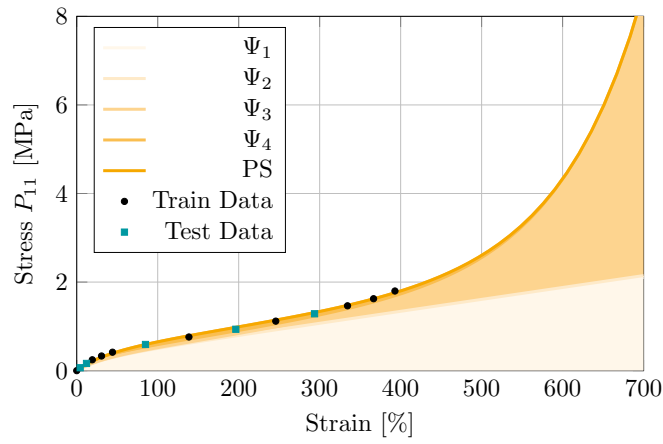
G_c	G_e	β	δ
0.20 MPa	0.19 MPa	0.34	0.10

Tab. 5.3: Material parameters of the non-hyperelastic Shariff model [87] for the Treloar data set.

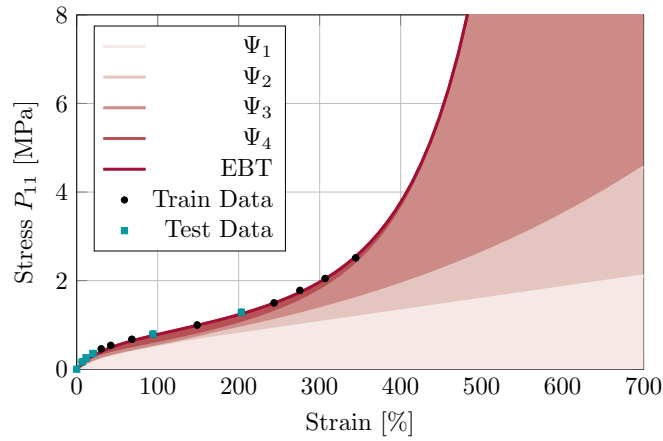
E	α_0	α_1	α_2	α_3	α_4
1.17 MPa	1.00	8.65×10^{-1}	3.66×10^{-2}	8.35×10^{-5}	2.04×10^{-2}



(a)

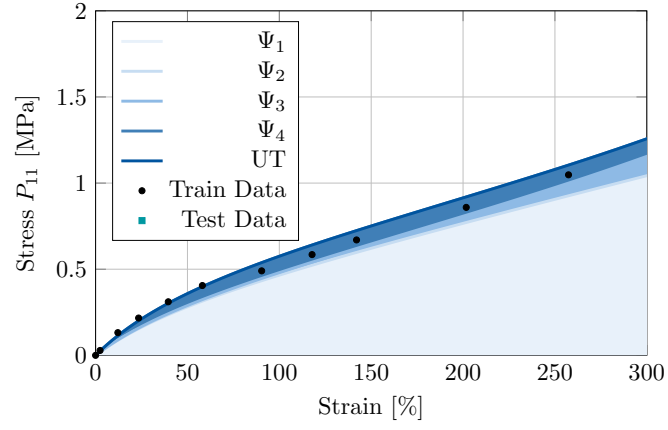


(b)

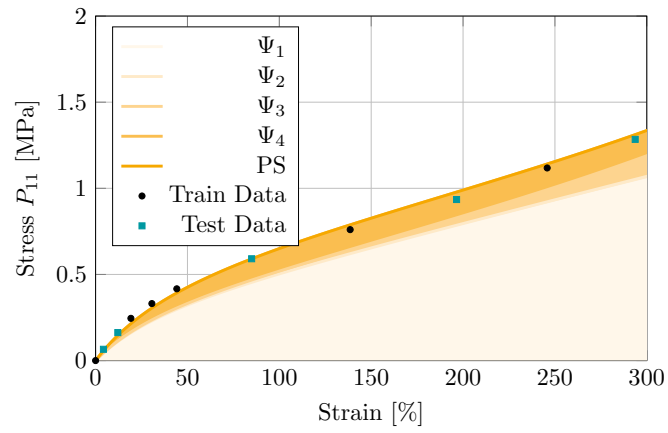


(c)

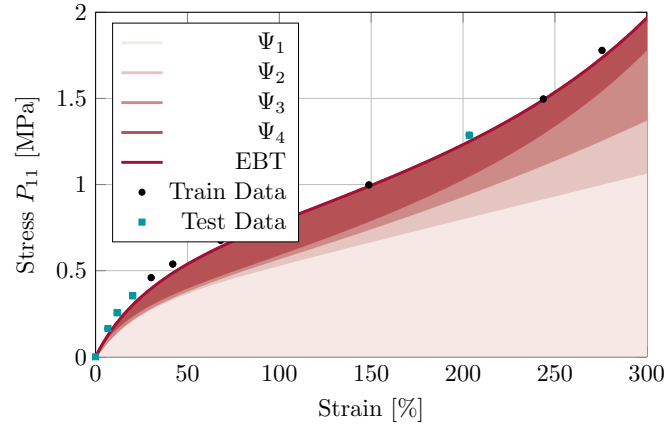
Fig. 5.3: Visualization of the contributions of each term Ψ_i for $i = 1, \dots, 4$ in the strain energy identified in Equation 5.2. The responses are shown for UT, PS and EBT for the strain range from 0.00 % to 700.00 %.



(a)

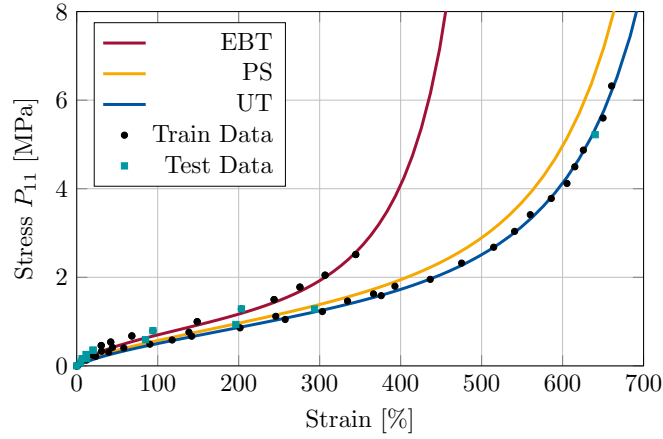


(b)

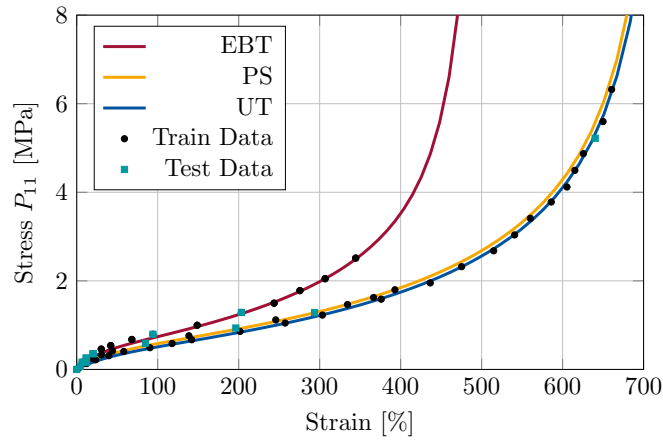


(c)

Fig. 5.4: Visualization of the contributions of each term Ψ_i for $i = 1, \dots, 4$ in the strain energy identified in Equation 5.2. The responses are shown for UT, PS and EBT for the strain range from 0.00 % to 300.00 %.

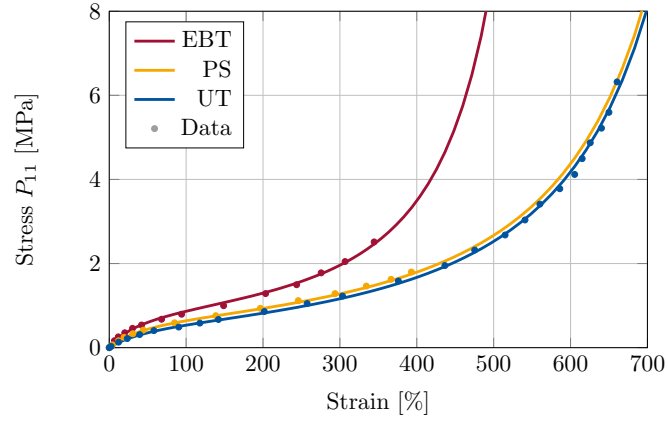


(a)

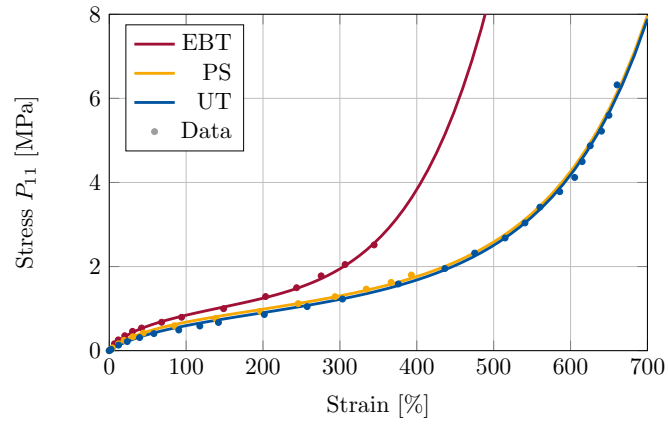


(b)

Fig. 5.5: Visualization of the stress-strain responses of novel models influenced by two different noise levels. The responses are derived from the strain energy functions described in Equation 5.5 and Equation 5.6.



(a)



(b)

Fig. 5.6: Best fit for the Treloar data set using (a) the extended tube model ($R^2 = 96.56\%$), (b) the non-hyperelastic Shariff model ($R^2 = 96.38\%$) for UT, PS and EBT. The used material parameters are listed in Table 5.2 and Table 5.3, respectively.

5.2 Stretch-Based Model Identification

As previously outlined in Section 4.4, it is possible to identify a material model through the use of a stretch-based formulation. The material parameters provided by Ogden for the Treloar data set can adequately describe the stress-strain response with a reasonable degree of accuracy. These material parameters are listed in Table 5.4. The responses for the UT, PS and EBT

Tab. 5.4: List of material parameters of the Ogden model for the Treloar data set, as detailed in [75].

	$i = 1$	$i = 2$	$i = 3$
α_i	1.30	5.00	-2.00
μ_i	0.63 MPa	0.12×10^{-2} MPa	-0.10×10^{-1} MPa

data are presented in Figure 5.7. It is evident that the model displays a slight

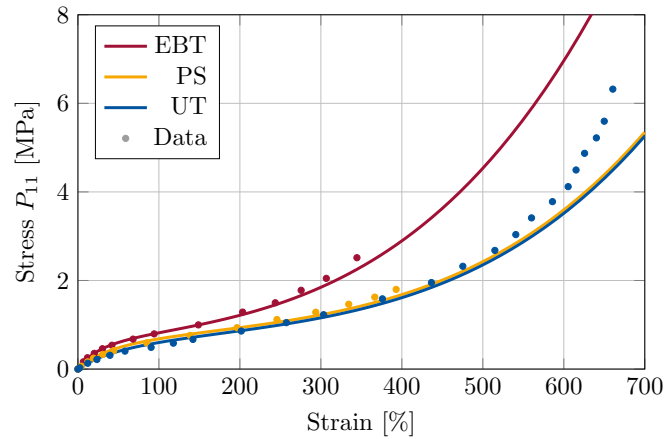


Fig. 5.7: Best fit for the Treloar data set using the stretch-based Ogden model for UT, PS and EBT. The used material parameters are listed in Table 5.4.

tendency to underestimate the UT, PS, and EBT responses for strain up to 400.00 %. A further notable shortfall in performance is evident for strains exceeding 500.00 %, where the UT response is underestimated. It should be noted that the level of accuracy achieved was only possible with the use of a total of six material constants.

This prompts the question of whether an alternative stretch-based formulation could provide a superior fit to the underlying data set using DSO. Once more, the basis list of functions has been expanded with the incorporation of the power function ("pow") for this analysis. The aforementioned approach based on the Valanis-Landel assumption is utilized to identify a novel material model.

Once again, an 80.00 % to 20.00 % train-test split was employed. The function ω was identified as follows:

$$\omega(\lambda) = 1.44 \left(0.4 \frac{2.96^\lambda}{\lambda} + \left(0.62 \sqrt{0.61\lambda + \sqrt{\exp\left(\frac{2.0^\lambda}{\lambda}\right)} - 1} \right)^{0.65} \right)^{0.4}. \quad (5.7)$$

The stress-strain response of the data set is illustrated in Figure 5.8. It is noteworthy that an R^2 score of 98.06 % was achieved, indicating that the identified strain energy function accurately predicts the responses for all three loading cases. It is evident that the model accurately predicts the responses across the entire strain region, exhibiting a superior performance compared to the Ogden model.

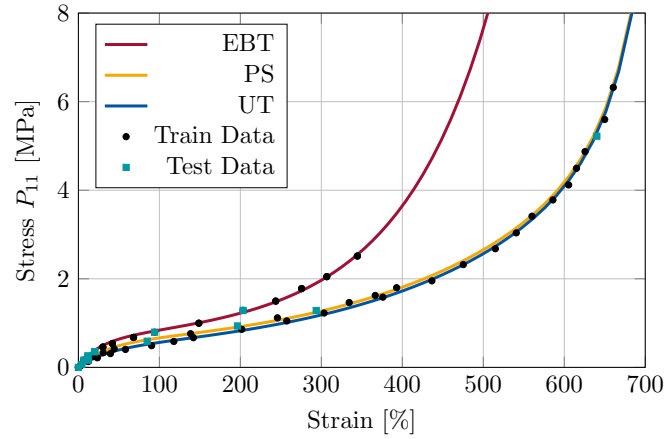


Fig. 5.8: Best fit for the Treloar data set using a novel stretch-based model discovered through DSO. The model, described in Equation 5.7, is based on the Valanis-Landel assumption. The fit is shown alongside corresponding training and test data for UT, PS and EBT.

This example demonstrates the effectiveness of a stretch-based approach in accurately characterizing the Treloar data set. While the degree of accuracy has been enhanced, the notable increase in complexity of the model is a significant drawback. However, further investigations and detailed analysis are necessary to fully determine the potential of this approach. One potential avenue for enhancing the simplicity of this approach is the incorporation of possible priors into the DSO framework.

5.3 Biaxial Loading of Vulcanized Rubber

In 1981, Kawabata et al. published the results of their comprehensive experimental investigation aimed at gaining a detailed understanding of the strain energy function of isoprene rubber vulcanizate [77]. They conducted a series of experiments on the biaxial extension of a sheet specimen at varying temperatures, building upon the work previously presented by Treloar. This data is a significant benchmark for evaluating and assessing the performance of different constitutive models. A primary objective was to determine the significance of the first and second invariants through biaxial deformation testing, providing highly accurate experimental data in both small and large deformation regions. To guarantee the accuracy of the results, specialised equipment was developed to enable precise measurements in the small-deformation region. In their theoretical discussion, they assumed that the material under consideration can be considered incompressible. The primary conclusions of their research are for the derivatives of the strain energy with respect to the invariant they noticed that $\frac{\partial \Psi}{\partial I_C} > \frac{\partial \Psi}{\partial II_C}$ for all deformation scenarios and that the derivative with respect to the second invariant $\frac{\partial \Psi}{\partial II_C}$ can assumed to be of negative value under small strain conditions.

To evaluate the performance of the DSO package on the Kawabata data set, three different training scenarios are explored. In the first scenario the UT, PS, and EBT responses will be used to identify a strain energy function. The remaining data will be used to evaluate the performance of the model, specifically its ability to predict the P_{11} and P_{22} responses without prior knowledge of the underlying data for P_{22} . It is important to note that the stretch information λ_2 is only provided through the information of the first and second invariant. In the second scenario, all data sets for the BT responses are used to determine if the model's performance improves with this additional information. The fitting is again only performed on the P_{11} stress. In the final scenario, the entire data set is used to evaluate the model's ability to accurately predict all data points including the P_{11} and the P_{22} stresses. A test train split of 70.00 % to 30.00 % is applied for all three cases. It is important to note that the strain energy function was determined as a function of the invariants I_C and II_C as inputs, although the data are given for the stretches λ_1 and λ_2 . Accordingly, a straightforward transformation is employed to ascertain the values of the invariants, as detailed in [77].

For the first example, the identified strain energy is given by

$$\Psi_{K,1} = 0.43 \left(0.38 \left[I_C \left(0.30 I_C - 8.58 \times 10^{-4} II_C \ln II_C - 0.30 \ln I_C + 4.73 \right) + II_C \right] + 1 \right)^{\frac{1}{2}}. \quad (5.8)$$

The corresponding predictions are visualized in Figure 5.9. The R^2 score is given with 99.67 % and the strain energy demonstrates a high degree of agreement between the predicted responses and the experimental data for UT, PS and EBT as depicted in Figure 5.9(a). Nevertheless, it is yet to be established how accurately the strain energy will predict responses in other scenarios. Therefore, Figure 5.9(b) illustrates the response of P_{11} as a function of the stretch λ_2 , while Figure 5.9(c) depicts the response of P_{22} . Figure 5.9(b) demonstrates that these three loading cases are sufficient for characterizing the material's behavior across various stretch combinations. A more detailed analysis of the P_{22} response indicates that, despite not being included during the fitting process, the strain energy function accurately captures the trends in the stress-strain responses. It can be concluded that the information provided by P_{11} is not fully sufficient for comprehensive predictions of P_{22} .

For the second training case the strain energy is given by

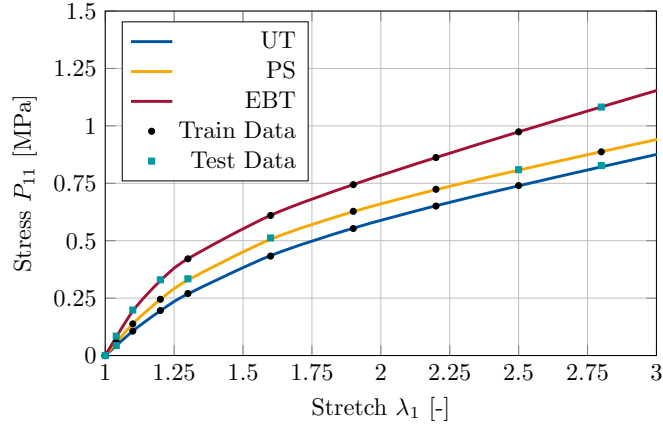
$$\begin{aligned} \Psi_{K,2} = & 0.17I_C - 0.03 + 0.10 \left(3.69 - 2.21 \sqrt{0.09I_C - 0.20\sqrt{II_C} + 1} \right) \\ & \cdot \ln \left(4.74I_C + II_C + \ln \left(\sqrt{II_C} \right) + \frac{5.21}{I_C} \right). \end{aligned} \quad (5.9)$$

The corresponding stress-strain responses are illustrated in Figure 5.10. It is evident that the generated predictive response is of an exceedingly high degree of accuracy, as indicated by an R^2 score of 99.40 %. In the second training case, all data from the biaxial loading were utilized. However, only the P_{11} response was fitted, while the P_{22} response was excluded from the fitting process. Figure 5.10(a) depicts the responses of UT, PS, and EBT while Figure 5.10(b) illustrates P_{11} over the stretch λ_2 . The fit is notably precise for the UT, PS, and BT responses, effectively capturing all observed trends. In Figure 5.10(c) the response of P_{22} over the stretch λ_2 is depicted. As illustrated, the predictive accuracy of the model for P_{22} is less precise in comparison to P_{11} . The predicted response is found to be a significant underestimate of the material's behavior, particularly for strains of $\lambda_1 = 3.7$. This indicates that both stresses are indispensable for the fitting.

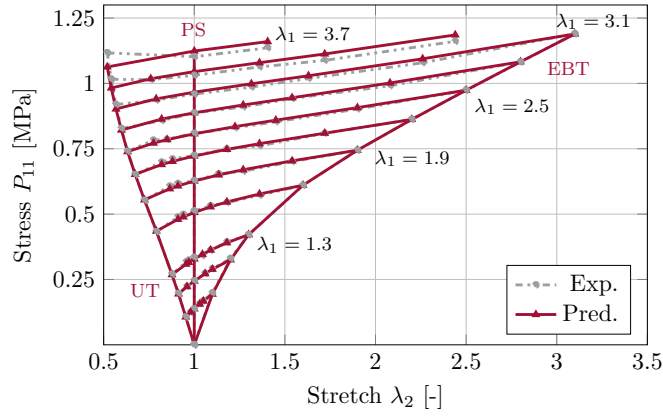
In the final case, both P_{11} and P_{22} responses were used for the fitting. The strain energy was determined with

$$\begin{aligned} \Psi_{K,3} = & 0.12I_C + 0.12\sqrt{II_C} - 0.03 \ln II_C \\ & - 0.03 \ln \left(\ln (II_C)^4 \right) - 0.13 - \frac{0.03 (-3.49I_C - 5.88II_C) \ln (II_C)}{II_C}. \end{aligned} \quad (5.10)$$

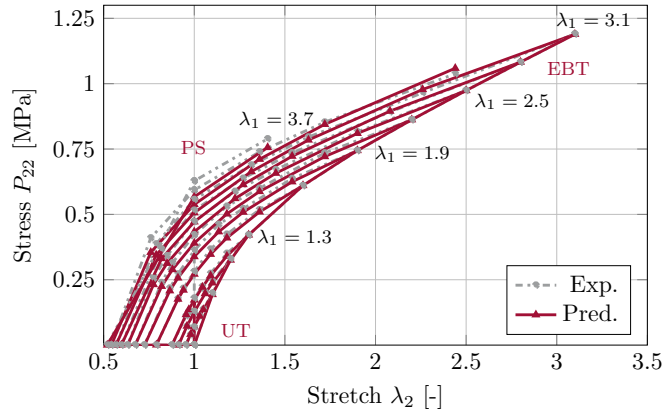
The resulting responses are visualized in Figure 5.11. In this instance, the generated predictions are observed to be of an extremely high degree of accuracy with a R^2 score of 98.40 %. Figure 5.11(a) depicts the predicted outcomes



(a)

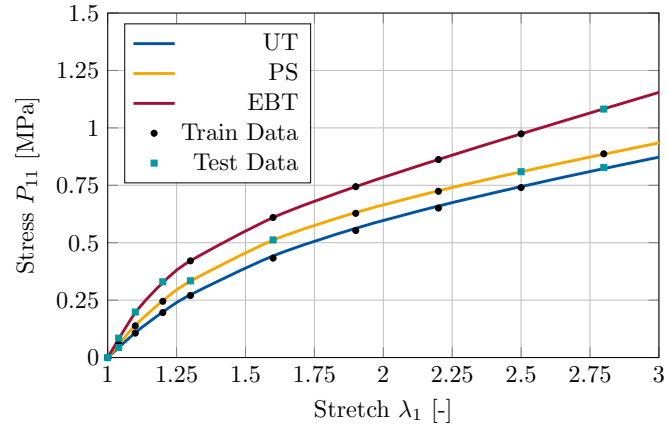


(b)

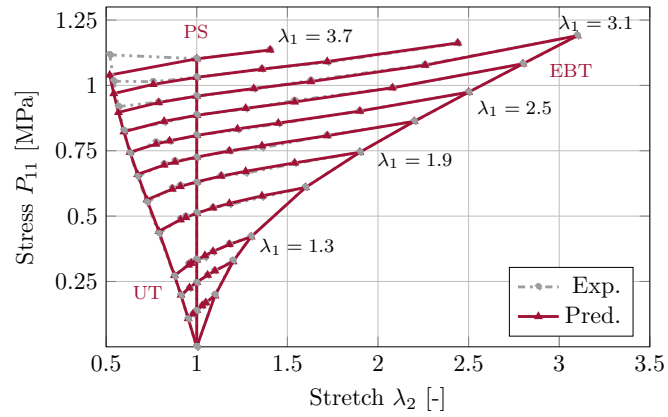


(c)

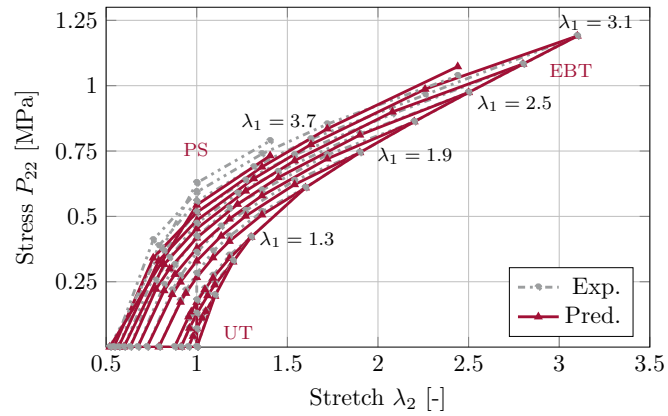
Fig. 5.9: Stress-strain responses for P_{11} and P_{22} for the Kawabata data set for λ_1 and λ_2 fitted using P_{11} of UT, PS and EBT. The responses are based on the strain energy function identified in Equation 5.8.



(a)

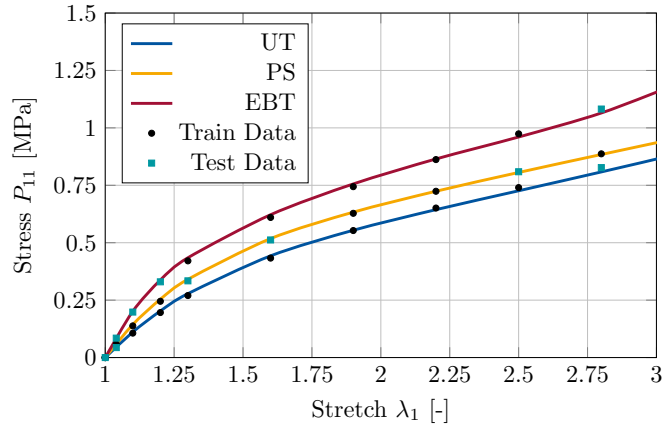


(b)

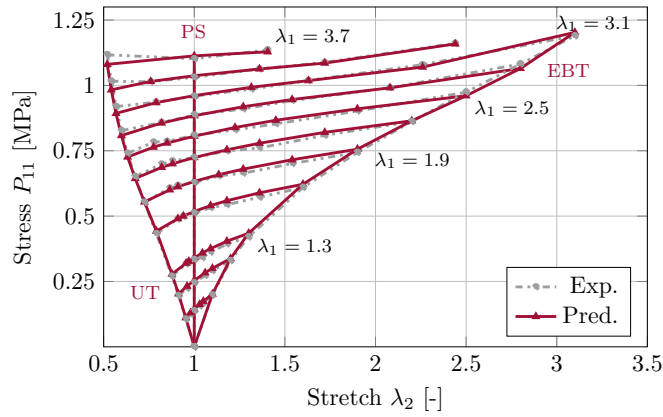


(c)

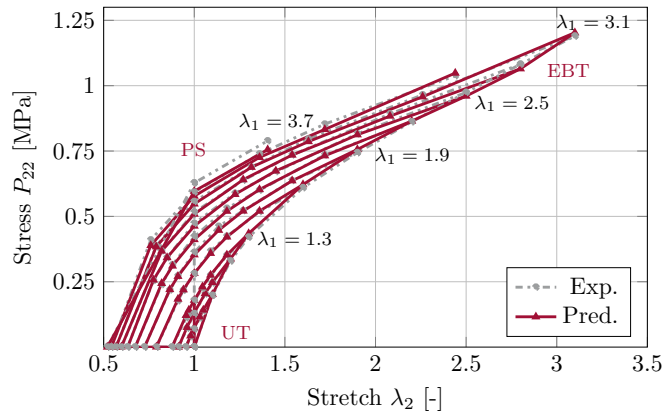
Fig. 5.10: Stress-strain responses for P_{11} and P_{22} for the Kawabata data set for λ_1 and λ_2 fitted using P_{11} data. The responses are based on the strain energy function identified in Equation 5.9.



(a)



(b)



(c)

Fig. 5.11: Stress-strain responses for P_{11} and P_{22} for the Kawabata data set for λ_1 and λ_2 fitted using P_{11} and P_{22} data. The responses are based on the strain energy function identified in Equation 5.10.

for UT, PS, and EBT. Figure 5.11(b) illustrates the response of P_{11} over λ_2 , while Figure 5.11(c) illustrates the response of P_{22} over λ_2 . The fitting of both stress responses has resulted in a notable enhancement in the precision of the calculated P_{22} response. Nevertheless, a slight underestimation persists.

It is crucial to acknowledge that the identified strain energy functions display distinctive characteristics that differentiate them from one another. This analysis indicates that there is no single, universally applicable strain energy function, rather, multiple potential functions can adequately fit the same data set. It is apparent that all formulations possess pronounced nonlinear characteristics. Moreover, the identified strain energy functions illustrate that both inputs, I_C and II_C , are indispensable for developing a reasonable model. As proposed by Kawabata et al., the micro-mechanical interpretation suggests that the dependency on I_C is primarily associated with intramolecular forces, while the dependency on II_C reflects intermolecular interactions [77]. It is, however, worthy of note that physically motivated models do not typically incorporate the second principal invariant in their formulations of strain energy functions. While this investigation does not establish any specific micro-mechanical relationships, it highlights the necessity of both inputs for the identification of an effective model. Moreover, this investigation indicates that for a precise model capable of predicting a variety of loading scenarios, both the P_{11} and P_{22} responses are indispensable for the fitting process. While the experimental data obtained from UT, PS, and EBT experiments can yield satisfactory fits, it is crucial to acknowledge that these data may not provide highly accurate predictions for specific loading cases, particularly with regard to the P_{22} response. The P_{11} stress is sufficiently robust for the identification of a strain energy function which effectively captures the observed trends in the P_{22} response.

5.4 Temperature-Dependent Thermoplastic Polyester Elastomer

The mechanical behavior of elastomers is subject to significant influence from temperature. A change in temperature can affect a material's fundamental properties, including its Young's modulus, tensile strength, and stress-strain response. It is therefore essential to consider this effect and to study the mechanical behavior over a range of different boundary conditions when modeling materials. It is common practice in the field of constitutive hyperelastic modeling to incorporate the effects of temperature by considering temperature-dependent material properties or by introducing additional temperature-dependent terms in the strain energy function. As discussed in Section 3.2, the framework presented here can be easily extended to include the influence of other parameters such as temperature. This methodology

allows for the systematic accounting of all potential nonlinearities due to temperature effects, resulting in more sophisticated models that incorporate not only variations in material parameters.

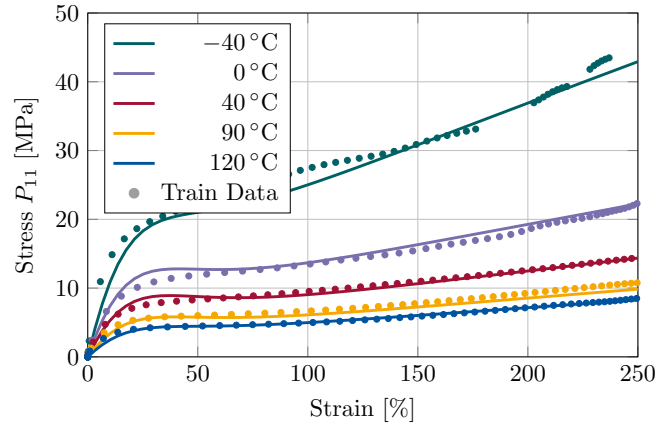
The following section will examine a temperature-dependent data set, which presents the stress-strain response of the thermoplastic polyester elastomer Hytrel 4556 for the uniaxial tensile loading case [89]. A total of nine stress-strain curves for temperatures between -40.00°C and 120.00°C are available for the purpose of identifying a suitable material model. In this particular example, the `gplearn` package will be employed. The temperature-dependent strain energy function Ψ_{Hy} was determined by the following equation:

$$\begin{aligned} \Psi_{\text{Hy}} = & \text{I}_{\bar{\mathbf{C}}} \exp \left(\left[\left(-\bar{T} + \exp \left(1.41 \sqrt{0.5 \bar{T}_l^2 - \bar{T}_l} \right) - 1.0 \right) \bar{T}_l^2 \right]^{\frac{1}{2}} \right) \\ & + 0.131 \text{I}_{\bar{\mathbf{C}}} \bar{T}_l - 2 \text{II}_{\bar{\mathbf{C}}} \bar{T}_l + \exp (41.19 \exp (-\text{II}_{\bar{\mathbf{C}}})) \bar{T}_l, \end{aligned} \quad (5.11)$$

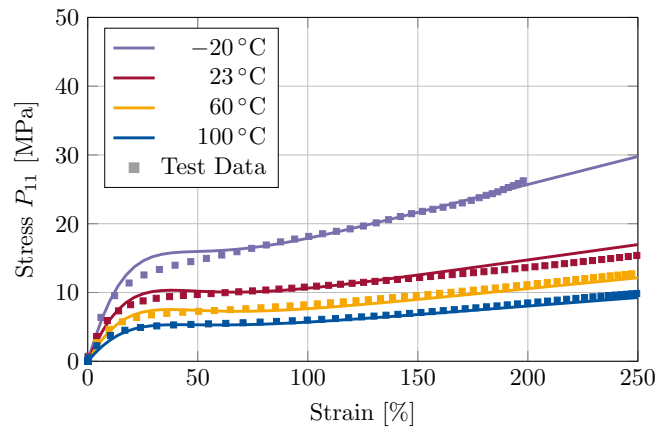
where $\bar{T}_l = \ln \bar{T}$ and \bar{T} is a scaled temperature given by

$$\bar{T} = \frac{T}{400} + \frac{1}{2}. \quad (5.12)$$

While not a mandatory requirement from a mathematical standpoint, scaling the input variables to a similar order of magnitude is advantageous for the numerical performance of the optimization procedure. Figure 5.12 illustrates the stress-strain responses for the test and training data sets. As anticipated, the stress response at lower temperatures is markedly stiffer than that observed at higher temperatures. The fitting was conducted on a training set that included only five temperature-dependent curves (-40.00°C , 0.00°C , 40.00°C , 90.00°C , 120.00°C) (see Figure 5.12(a)). The remaining four curves (-20.00°C , 23.00°C , 60.00°C , 100.00°C) were not included during the training phase. Consequently, they can be employed as a test set for the evaluation of the accuracy and reliability of the predicted strain energy function (see Figure 5.12(b)). For both sets, even for the curves that were not included in the training data set, the predicted stress response is in close agreement with the experimental data. The use of symbolic regression offers a substantial advantage in the form of interpretable algebraic equations, which will be the focus of this section's investigation. The primary objective will be to examine the strain energy derived from the experimental temperature-dependent data set, as presented in Equation 5.11, which will be analyzed in greater detail. Initially, the material law is simplified for the temperatures $T_1 = -20.00^\circ\text{C}$, $T_2 = 0.00^\circ\text{C}$ and $T_3 = 20.00^\circ\text{C}$, resulting in three distinct expressions for the



(a)



(b)

Fig. 5.12: Temperature-dependent stress-strain responses for the thermoplastic polyester elastomer Hytrel 4556 [89]. The responses for both the training and test sets are derived from the strain energy function described in Equation 5.11.

strain energy given by

$$\bar{\Psi}_{\text{Hy}}(\text{I}_{\bar{\text{C}}}, \text{II}_{\bar{\text{C}}}, 0.45) = 3.89\text{I}_{\bar{\text{C}}} + 1.60\text{II}_{\bar{\text{C}}} - 0.80 \exp(41.19 \exp(-\text{II}_{\bar{\text{C}}})) , \quad (5.13)$$

$$\bar{\Psi}_{\text{Hy}}(\text{I}_{\bar{\text{C}}}, \text{II}_{\bar{\text{C}}}, 0.50) = 2.85\text{I}_{\bar{\text{C}}} + 1.39\text{II}_{\bar{\text{C}}} - 0.69 \exp(41.19 \exp(-\text{II}_{\bar{\text{C}}})) , \quad (5.14)$$

$$\bar{\Psi}_{\text{Hy}}(\text{I}_{\bar{\text{C}}}, \text{II}_{\bar{\text{C}}}, 0.55) = 2.21\text{I}_{\bar{\text{C}}} + 1.20\text{II}_{\bar{\text{C}}} - 0.60 \exp(41.19 \exp(-\text{II}_{\bar{\text{C}}})) . \quad (5.15)$$

This simplification demonstrates that the strain energy is comprised of precisely three additive terms. Upon slight rearrangement of the strain energy formulation, the following derivation is obtained:

$$\bar{\Psi}_{\text{Hy}} = \underbrace{C_1(\bar{T})\text{I}_{\bar{\text{C}}}}_{\Psi_1} + \underbrace{C_2(\bar{T})\text{II}_{\bar{\text{C}}}}_{\Psi_2} + \underbrace{C_3(\bar{T}) \exp(41.19 \exp(-\text{II}_{\bar{\text{C}}}))}_{\Psi_3} , \quad (5.16)$$

where $C_1(\bar{T})$, $C_2(\bar{T})$ and $C_3(\bar{T})$ represent three temperature-dependent coefficients given by

$$C_1(\bar{T}) = \exp \left(\left[\left(-\bar{T} + \exp \left(1.41 \sqrt{0.5\bar{T}_l^2 - \bar{T}_l} \right) - 1.0 \right) \bar{T}_l^2 \right]^{\frac{1}{2}} \right) + 0.13\bar{T}_l, \quad (5.17)$$

$$C_2(\bar{T}) = -2\bar{T}_l, \quad (5.18)$$

$$C_3(\bar{T}) = \bar{T}_l. \quad (5.19)$$

A close examination of this formulation reveals that the initial two terms, Ψ_1 and Ψ_2 , align with the Mooney-Rivlin model, with temperature-dependent coefficients C_1 and C_2 . It bears mentioning that, based on an exhaustive literature review, the additional term Ψ_3 , which is weighted by the coefficient C_2 , has not yet been proposed in any existing literature. It is possible to illustrate the evolution of these coefficients C_i across the temperature range from -40.00°C to 120.00°C , as depicted in Figure 5.13. It can be observed that both coefficients C_1 and C_2 are positive. The plot demonstrates that while the value of coefficient C_1 is initially greater than that of C_2 , C_1 also exhibits a more rapid decline as temperature increases. The coefficient C_3 is inversely proportional to temperature and approaches zero at higher temperatures. As the generated model is of an additive nature, the contributions of each term Ψ_i can be decomposed, as shown in Figure 5.14 for the temperatures -40.00°C , -20.00°C and 0.00°C . The term Ψ_3 plays a crucial role in the strain range from 0.00% to 100.00% , serving as the primary factor influencing the initial stiffness of the material. Nevertheless, this effect decreased considerably as the strain increased. The primary stress response is mainly attributed to term Ψ_1 , while term Ψ_2 seems to function as an additional correction factor. This

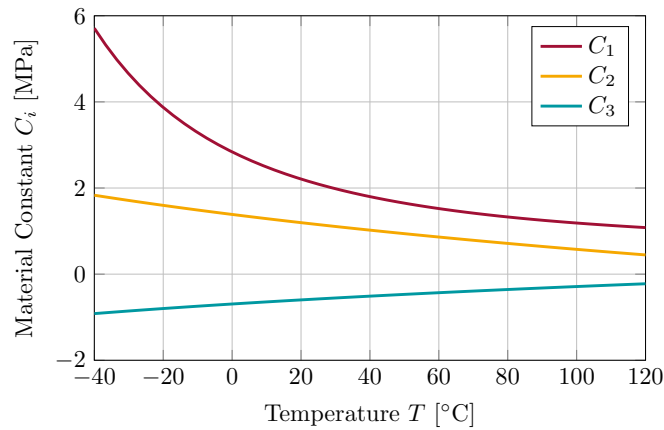
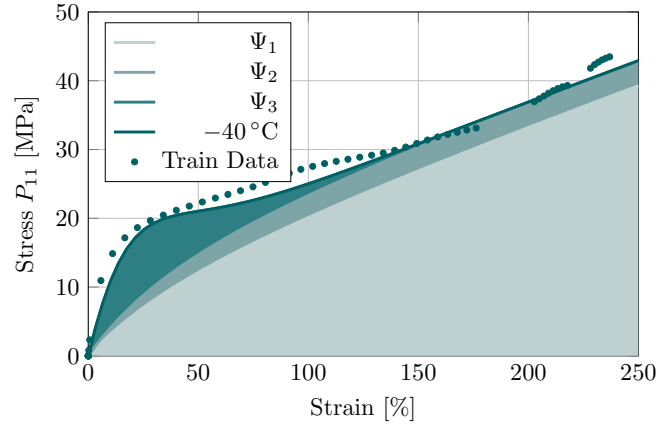
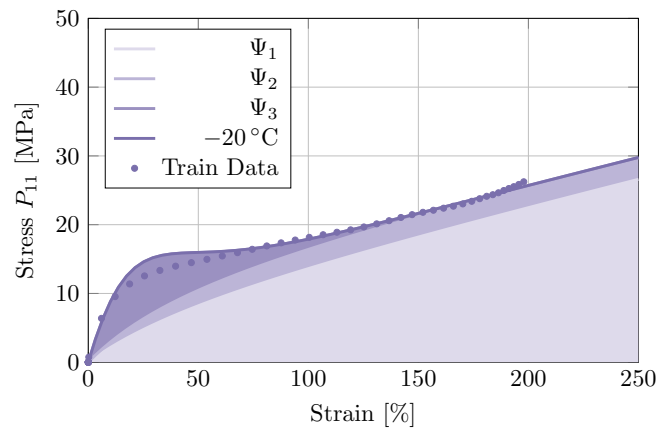


Fig. 5.13: Visualization of the material constants C_i as a function of temperature for thermoplastic polyester elastomer Hytrel 4556.

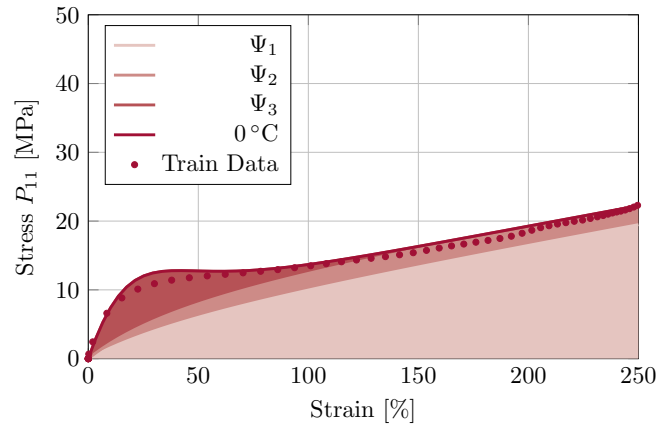
example demonstrates the straightforward analysis of a novel strain-energy formulation through the use of SR, which offers a notable advantage over alternative methods such as neural networks, sparse regression, or model-free approaches. As previously outlined, SR offers a comprehensive understanding of the fundamental material models and uncovers the manner in which particular terms impact the comprehensive stress-strain response. Moreover, the identified models are genuinely novel and can be adapted to specific materials based on the provided data. The specific characteristics of the material are accurately identified, and the framework can be trained using sufficiently small data sets. The framework displays the ability to identify and capture the underlying physical relationship, as evidenced by its interpolation and extrapolation capabilities.



(a)



(b)



(c)

Fig. 5.14: Visualization of the temperature-dependent contributions of each term Ψ_i for $i = 1, \dots, 3$ for the thermoplastic polyester elastomer Hytrel 4556 [89]. The responses for both the training and test sets are derived from the strain energy function described in Equation 5.11.

6 Rediscovering the Mullins Effect

Prediction is very difficult, especially if it's about the future!

N. BOHR

Elastomers, and in particular reinforced rubbers, typically demonstrate a softening behavior that emerges during the unloading phase and persists during the subsequent loading. This phenomenon was initially documented in the seminal work of Mullins and is henceforth referred to as the Mullins effect [90], see Figure 6.1. This phenomenon is more pronounced in materials containing an increasing amount of filler particles, such as carbon black or silica. It is typically accompanied by a range of other inelastic effects, including residual strain and deformation induced anisotropy [91]. Deformation-induced anisotropy describes the behavior of a material in which the response to tensile stress along the preload direction differs from the response to tensile stress in any other direction. The phenomenon of permanent set is typically associated with the Mullins effect. A substantial body of experimental evidence indicates that these effects are contingent upon the specific strain level, strain rate, and loading history. Furthermore, the Mullins effect is highly persistent and remains present even after a considerable period of relaxation. Nevertheless, this phenomenon can be reversed by subjecting the material to exposure of high temperature in a vacuum [92].

The physical source of the Mullins effect, despite its widespread appearance and importance, remains a topic of debate in the scientific community. For further insight, see, e.g., [93] and references therein. The Mullins effect has been interpreted in several differing physical perspectives. These include the detachment of polymer molecules from the filler interface, molecular slippage, and the rupture of filler clusters. These interpretations have been used as a foundation for micro-mechanically motivated material models of the Mullins effect.

One of the earliest phenomenological models of the idealized isotropic Mullins effect was proposed by Ogden and Roxburgh [94]. This pseudo-elastic model incorporates a damage parameter that is expressed as a function of the maximum value of the strain energy density that has been previously attained under tensile loading. Qi and Boyce developed a model with two distinct phases: one pertaining to a soft domain and the other to a hard domain [95]. The transition from the hard to soft domain is controlled by a state variable. An updated version of the Ogden-Roxburgh model has been developed by

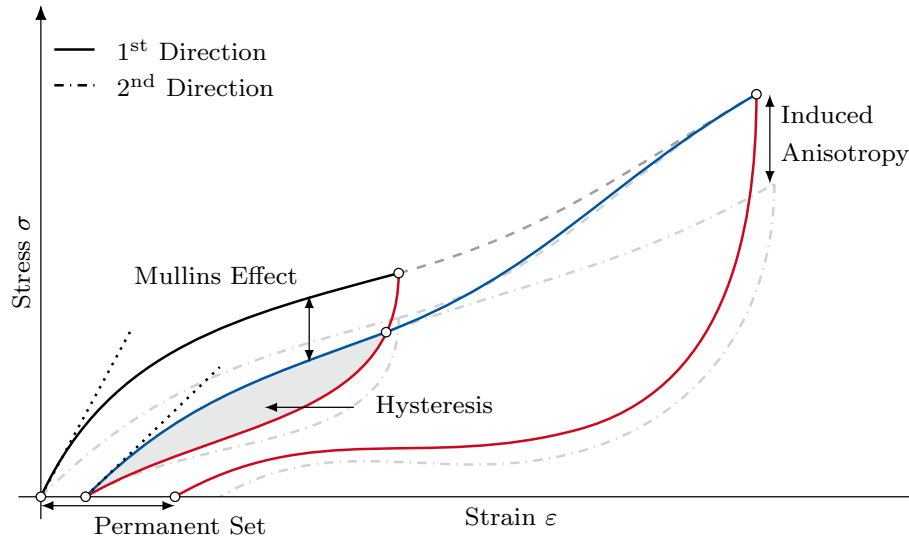


Fig. 6.1: Schematic stress-strain response of a rubber sample undergoing a loading cycle, followed by an unloading and reloading cycle. The curve demonstrates the Mullins effect and permanent set behavior.

Ogden and Dorfmann [96]. In this work, an alternative dissipation function was proposed as a means of representing the effects of stress softening and permanent set. Furthermore, another phenomenological model of the Mullins effect was proposed, which included permanent set and induced anisotropy [97]. A thermodynamically consistent phenomenological model of the anisotropic Mullins effect, including permanent set, was formulated in terms of principal stretches [98]. To describe the anisotropic Mullins effect in carbon black filled rubbers, a micro-mechanically motivated approach was proposed in [99]. Furthermore, a generalized network decomposition model for filled elastomers has been introduced [100]. In a recent publication, Ayoub et al. presented a visco-hyperelastic damage model that is capable of capturing a number of important mechanical phenomena, including cyclic stress softening, hysteresis, and permanent set [101]. Moreover, Khiêm and Itskov proposed an averaging-based tube model, applicable to both filled and unfilled elastomers [102], which was subsequently extended to model mechanically induced chemiluminescence in elastomers [103]. A micro-mechanical approach to modeling thermally induced aging in elastomers was proposed by Mohammadi et al. [104]. Recently, a modeling approach for Mullins-type damage behavior in double network hydrogels was presented in [105]. Guo et al. [106] introduced a model predicting deformation-induced damage and failure in elastomers, while Morovati et al. [107] considered damage accumulation effects for fatigue-induced stress softening in cross-linked multi-networked elastomers. Furthermore, Saadedine et al. presented a multiscale model for describing multi-axial inelastic behavior of elastomeric particulate composites [108]. Wang et al. [109] proposed an advanced model to study the influence of magnetic fields on the viscoelastic

behavior of soft magnetorheological elastomers under finite strain.

In the following investigation, the primary goal is to rediscover the Mullins effect using SR. Accordingly, a benchmark analysis will be conducted using artificial data generated through the Ogden-Roxburgh model. Moreover, the analysis will be complemented by an investigation of a temperature-dependent experimental data set of a filled silicone [110]. The primary objective is to assess the quality of the automatically generated material models in terms of accurate interpolation and extrapolation of experimental data. Additionally, it is crucial to examine the influence of data set size and input variables on model accuracy. In accordance with the methodology previously outlined, the continuum mechanical framework presented in Chapter 3 is integrated with SR as explained in Chapter 2 to determine an additional damage function. The analysis is conducted using the DSO package. To enhance adaptability, the modeling procedure is divided into two distinct phases. In the initial stage, the hyperelastic material model is identified. The determination of the strain energy necessitates an analysis of the stress-strain data obtained during the primary loading phase, which is commonly designated as the "virgin curve". As previously stated, the contributions of isochoric and volumetric effects to the strain energy function can be defined independently. Subsequently, these contributions serve as the foundation for the second stage, wherein the damage function is assessed and evaluated, as illustrated in Figure 6.2. Accordingly, the derived strain energy function Ψ is employed as the input variable for this stage. The fitting process for the damage function η is conducted on the cyclic data set. In this case, the maximum strain energy value attained in the preceding cycles, referred to as Ψ_m , is also provided as an input. In both steps, the first Piola-Kirchhoff stress is calculated in order to determine the strain energy and damage variable. This methodology can be extended to encompass additional inputs, including temperature, concentration, or even particle size distributions.

In the above mentioned pseudo-elastic model of the Mullins effect by Ogden and Roxburgh [94] the stress resulting from the hyperelastic constitutive equation is reduced by a damage variable η as follows

$$\mathbf{P} = \eta(\Psi_{\max}, \Psi) \mathbf{P}_0. \quad (6.1)$$

Accordingly, η depends on the actual strain energy Ψ and the maximal value Ψ_{\max} of the strain energy previously reached in the loading history and is described by

$$\eta(\Psi_{\max}, \Psi) = 1 - \frac{1}{r} \operatorname{erf} \left(\frac{\Psi_{\max} - \Psi}{m + \beta \Psi_{\max}} \right), \quad (6.2)$$

where $\operatorname{erf}(\cdot)$ represents the error function while r , β and m denote material constants. This model is an excellent choice for a benchmark due to its extensive usage and incorporation into commercial FE software. Moreover, its

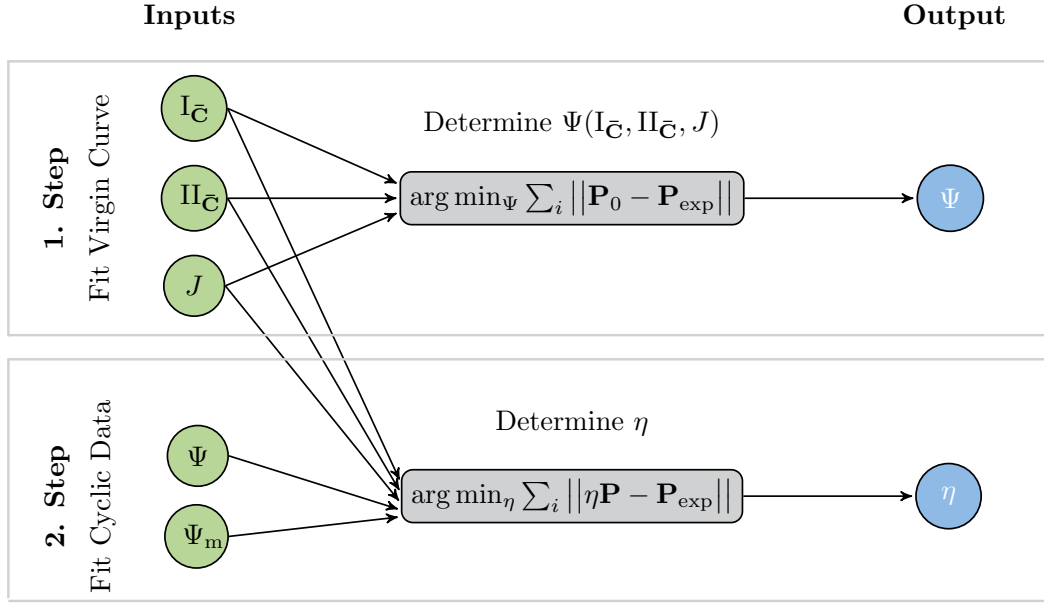


Fig. 6.2: Visualization of the two-step procedure implemented for modeling the Mullins effect. In the first step, the strain energy function Ψ is expressed in terms of invariants and other parameters using data from the primary loading curve. In the second step, the damage function η is determined using all inputs from the first step, along with the values of Ψ and Ψ_m . The fit is performed on cyclic loading data.

implementation is relatively straightforward, relying on only three material parameters. Moreover, this model has been shown to be an effective approach for accurately representing the Mullins effect.

Accordingly, Section 6.1 describes the application of the Ogden-Roxburgh model for the generation of an artificial data set for an initial benchmark. Therefore, the effectiveness of the proposed framework can be evaluated by quantifying its interpolation and extrapolation properties. In addition, it is crucial to evaluate the efficacy of this framework when applied to experimental data, which will be discussed in Section 6.2. To this end, the uniaxial tension data for six temperature ranges for filled silicone specimens will be employed in the subsequent analysis. A comprehensive analysis of the data set sizes and the reliability of the identified formulations for strain energy, as well as the damage variable, will be conducted for both artificial and experimental data. This chapter presents an edited version of my previous publication [1].

6.1 Benchmark Tests Using Ogden-Roxburgh Model

In order to assess the efficacy of the proposed framework in characterizing the softening behavior of elastomers, the Ogden-Roxburgh model is employed. As

outlined in Section 3.2 (see also Figure 6.2), the modeling process is initiated with an evaluation of the strain energy functions based on the primary loading. The stress-strain data for the primary loading have been generated using the generalized incompressible Mooney-Rivlin model, with the material constants for the first case of complexity (for further details, see the material constants for the DSO package in Table 4.1). The cyclic stress-strain data for unloading and subsequent reloading were obtained using the Ogden-Roxburgh model in Equation 6.2, with the following material constants: $r = 1.2$, $\beta = 0.5$ and $m = 2$.

To assess the quality of the interpolation and extrapolation, three load and unloading cycles were selected as training data to identify the damage function η , while two additional cycles were reserved for testing. The strain ranges within the training set ranged from 0.00 % to 100.00 %, while those within the test set ranged from 100.00 % to 150.00 %. Similar to the previous example, the training data was split with 80.00 % to 20.00 % to validate the interpolation quality. The first loading cycle consisted of 24 data points, the second of 42, and the third of 56. Consequently, the cyclic data for the test set included 70 and 82 data points for each of the three loading cases: UT, PS, and EBT. Furthermore, 74 additional data points were added to the existing data set for each loading case. However, only 122 of these points were included in the training set, which indicates that the data set as a whole remains relatively sparse.

As previously stated, the calculation of five strain energies and damage functions is essential for determining the impact of randomness on the output. A comparison of the mean stress-strain response of all five models, derived using the DSO package, with the corresponding training and test data for UT, PS, and EBT is presented in Figure 6.3. These diagrams depict the mean stress response and the corresponding 6σ confidence intervals, plotted against the strains for the loading cases of UT, PS, and EBT. It is noteworthy that the confidence interval in this particular example is exceedingly narrow. The proposed approach demonstrates a high degree of alignment with the underlying data, particularly in terms of both the interpolated and extrapolated ranges, which are predicted nearly perfectly. These outcomes are particularly noteworthy given the scarcity of the data utilized.

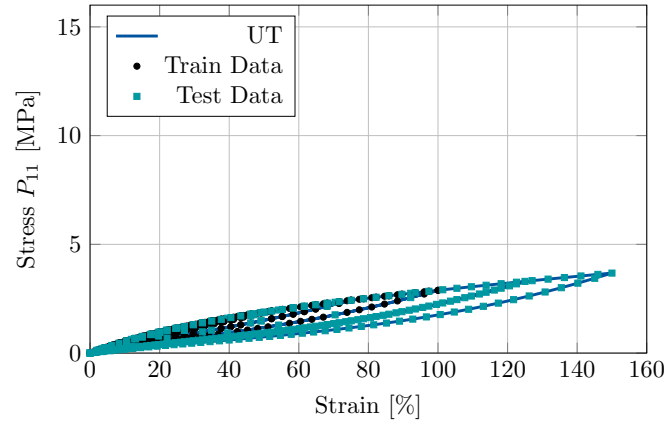
The recovery rates and the R^2 score for the virgin curve are identical to those obtained in Subsection 4.1.2. The damage variable exhibited an R^2 score exceeding 99.98 %, while the recovery rate reached 80.00 %. The determined damage models are listed in Table 6.1. The results of this benchmark test indicate that a limited number of loading cycles with sparse data are sufficient to recover the softening behavior with an extremely high degree of accuracy. The underlying continuum mechanical framework is capable of both interpolation and extrapolation of the given data, as well as a robust identification of the damage function.

It is similarly crucial to assess the impact of the train-test data split size. Ac-

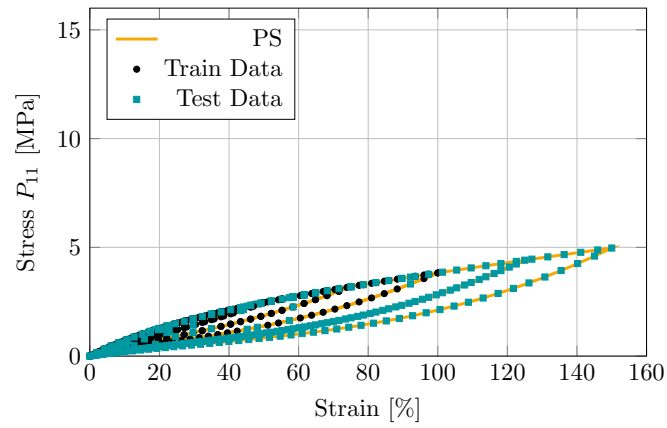
Tab. 6.1: Recovered damage models $\eta(\Psi, \Psi_{\max})$ for the Ogden-Roxburgh model, along with their corresponding R^2 scores.

N	Damage function $\eta(\Psi, \Psi_{\max})$	R^2 score
1	$0.83 \operatorname{erf}\left(\frac{4.0\Psi - 4.0\Psi_{\max}}{2\Psi_{\max} + 8.0}\right) + 1.0$	1.00
2	$0.83 \operatorname{erf}\left(\frac{4.0\Psi - 4.0\Psi_{\max}}{2\Psi_{\max} + 8.0}\right) + 1.0$	1.00
3	$0.83 \operatorname{erf}\left(\frac{\Psi - \Psi_{\max}}{0.5\Psi_{\max} + 2.0}\right) \operatorname{erf}(0.07\Psi + 1.21\Psi_{\max} + 3.09) + 1.0$	1.00
4	$0.83 \operatorname{erf}\left(\frac{2.0\Psi - 2.0\Psi_{\max}}{\Psi_{\max} + 4.0}\right) + 1.0$	1.00
5	$1.0 - 0.83 \operatorname{erf}\left(1.98 \frac{-\Psi + \Psi_{\max}}{\Psi_{\max} + 4.0}\right)$	1.00

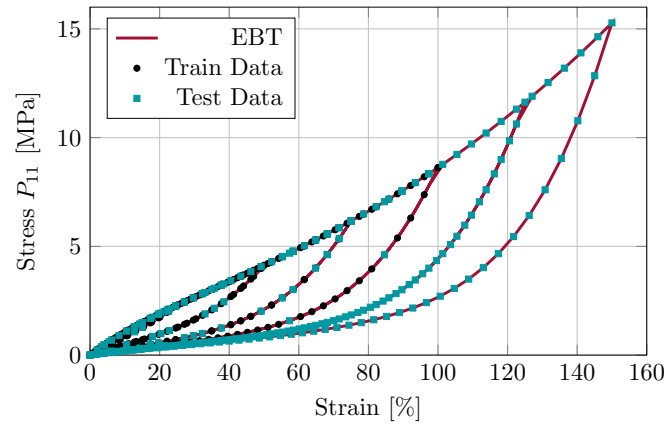
cordingly, an investigation is conducted into the performance of the framework when subjected to a test-train split of 70 to 30.00 % and 60 to 40.00 %. The results obtained with regard to the Ogden-Roxburgh model are illustrated in Figure 6.4 and Figure 6.5. Within the specified interpolation range, the results demonstrate a near-perfect fit for both train-test splits. It can be observed that the R^2 scores consistently exceed 99.80 %. As previously stated, it is possible to obtain a multitude of models that accurately describe the underlying data. Accordingly, a recovery rate of 80.00 % for the 70 to 30.00 % split and 20.00 % for the 60 to 40.00 % split were achieved. Upon examination of the extrapolation range, it was observed that for the 60 to 40.00 % train-test split, the confidence interval exhibited a notable widening in the final unloading cycle under EBT. It is evident that the efficacy of the models is influenced by the quantity of training data. The proposed approach demonstrates robust and highly accurate results for modeling softening behavior.



(a)



(b)



(c)

Fig. 6.3: Mean stress-strain response of all five models obtained using DSO, alongside the corresponding training and test data for UT, PS and EBT based on the generalized Mooney-Rivlin model of case 1 for the primary loading and the Ogden-Roxburgh model for the softening (unloading and further reloading). Shaded areas indicate 6σ confidence intervals.

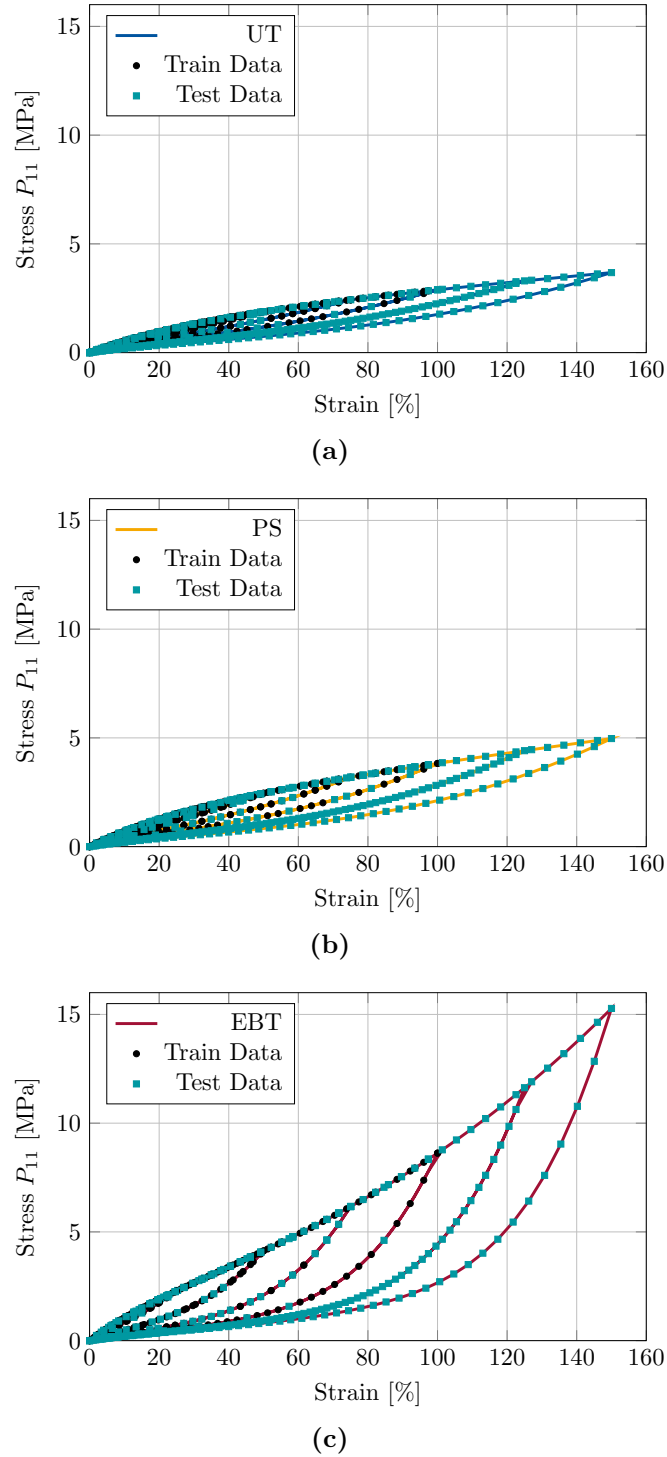
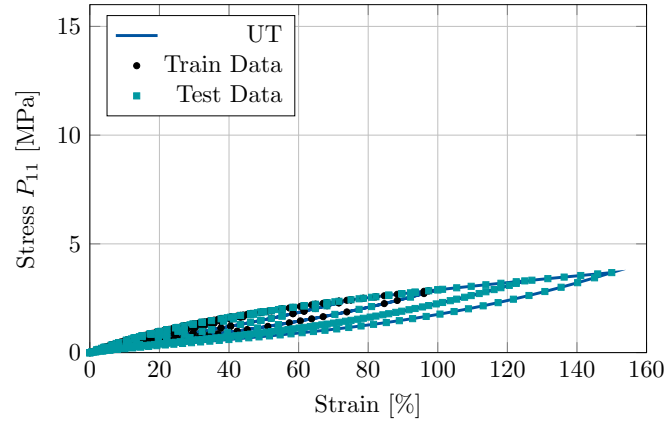
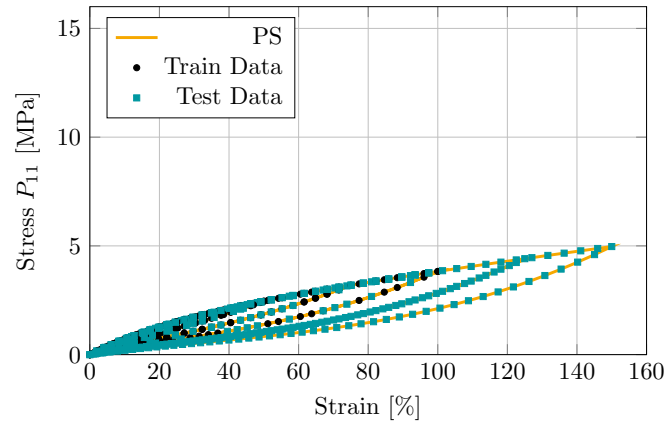


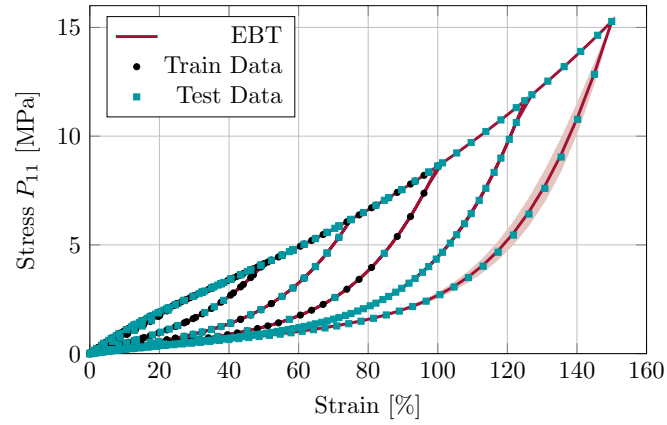
Fig. 6.4: Mean stress-strain response of all five models obtained using DSO, alongside the corresponding training and test data for UT, PS and EBT based on the generalized Mooney-Rivlin model of case 1 for the primary loading and the Ogden-Roxburgh model for the softening (unloading and further reloading). Results are obtained for a test-train split of 70.00 % to 30.00 %. Shaded areas indicate 6 σ confidence intervals.



(a)



(b)



(c)

Fig. 6.5: Mean stress-strain response of all five models obtained using DSO, alongside the corresponding training and test data for UT, PS and EBT based on the generalized Mooney-Rivlin model of case 1 for the primary loading and the Ogden-Roxburgh model for the softening (unloading and further reloading). Results are obtained for a test-train split of 60.00 % to 40.00 %. Shaded areas indicate 6σ confidence intervals.

6.2 Temperature-Dependent Filled Silicone

In the final analysis, an experimental data set that is dependent on temperature is considered [110]. In these experiments, filled silicone specimens were subjected to uniaxial tensile testing at temperatures of -40.00°C , -20.00°C , 20.00°C , 60.00°C , 100.00°C and 150.00°C . A series of loading and unloading cycles was conducted, with the amplitude gradually increasing at each step. A total of 120 data points were utilized to identify the strain energy function for the four specified training temperatures. Consequently, each curve consisted of 30 data points. The temperature-dependent strain energy function was determined from the primary loading curves under the temperatures -40°C , 20°C , 100°C and 150°C , while the curves of -20°C and 60°C served as test data. The material was considered as ideally incompressible. Accordingly, the following strain energy $\Psi_T(I_C, II_C, \tilde{T})$ was obtained:

$$\begin{aligned} \Psi_T(I_C, II_C, \tilde{T}) = & 0.11\sqrt[4]{I_C} \left[I_C \right. \\ & - 0.24\sqrt{0.85\left(\frac{II_C}{\tilde{T}} + \left(2.71\frac{I_C II_C}{\tilde{T}} + \ln\left(0.84\frac{I_C II_C}{\tilde{T}} + \ln \tilde{T}\right)\right)\right)} \\ & \left. \cdot \sqrt{\exp\left(0.55I_C\left(-2.28\tilde{T} + \ln \tilde{T} + 1.64\right)\right) - 1.03} - 2.65 \right], \end{aligned} \quad (6.3)$$

Here \tilde{T} is a scaled temperature mapping the temperature range from -100° to 200° to the data range between 0 and 1 using the following function:

$$\tilde{T} = \frac{T}{300} + \frac{1}{3}. \quad (6.4)$$

While rescaling the temperature range to a comparable order of magnitude is not a mathematically necessary step, it does enhance the computational efficiency of the optimization process. As explained in Section 3.2 the obtained strain energy function in Equation 6.3 is shifted such that the first condition in Equation 3.3 is satisfied. This shift is expressed as

$$\Psi_T^n(I_C, II_C, \tilde{T}) = \Psi_T(I_C, II_C, \tilde{T}) - \Psi_T(3, 3, \tilde{T}), \quad (6.5)$$

where the new function $\bar{\Psi}_T^n(I_C, II_C, \tilde{T})$ is used for identifying the temperature dependent damage function of the Ogden-Roxburg model in Equation 6.1. To this end, only unloading and reloading stress-strain data of the cyclic test for the temperature 20°C were used. All remaining cyclic data sets in particular for the temperatures -20°C 60°C served as test data. The so obtained damage

function is of the form

$$\begin{aligned} \eta_T(\Psi_T^n, \Psi_{T,\max}^n) = & 0.29 \coth \left[\Psi_T^n - 0.37 \Psi_T^n \left(\frac{\Psi_{T,\max}^n}{0.09 + 0.33 \Psi_T^n} \right. \right. \\ & + \operatorname{erf}(1936.97 + \Psi_{T,\max}^n) - \tanh(\Psi_T^n) \\ & + \tanh(1.33 - \tanh(1.90 - 14.49\Delta)) \\ & \left. \left. - \tanh[\tanh(1.67 - 47186.20\Delta)] \right] \right], \end{aligned} \quad (6.6)$$

where $\tanh(\cdot)$ and $\coth(\cdot)$ denote hyperbolic tangent and cotangent, respectively, $\Psi_{T,\max}^n$ is the maximal value of the accumulated strain energy while $\Delta = \operatorname{erf}(\Psi_T^n - \Psi_{T,\max}^n)$. The stress-strain responses resulting from Equation 6.3, Equation 6.6 according to Equation 3.6 and Equation 6.1 are shown in Figure 6.6 and Figure 6.7 for all temperatures. It is seen that only the primary curve and only one loading cycle were sufficient to describe very accurately the stress-strain responses at all six temperatures.

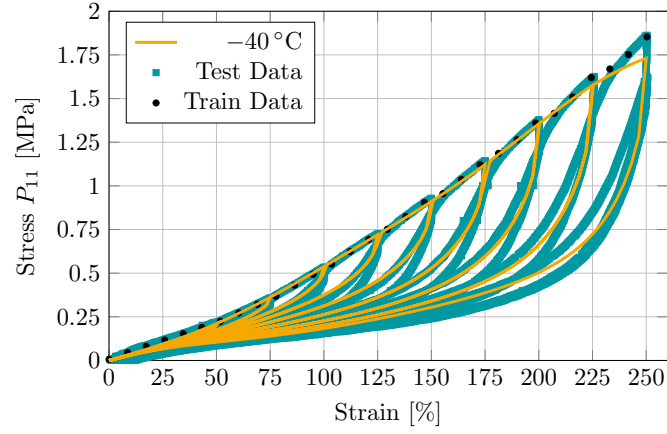
To further study the robustness of the proposed framework, the temperatures 20.00 °C, 60.00 °C and 100.00 °C for training and −40.00 °C, 20.00 °C and 150.00 °C for testing the same data set are used in an extrapolation performance analysis. Only the cyclic response of the −20.00 °C curve is applied to fit the damage variable.

Furthermore, it is essential to address the interpretability of the resulting model. A useful tool for such an investigation is to limit the complexity of the identified models. Therefore, the maximum length of the traversal is restricted to 32 tokens. The strain energy function obtained for this new evaluation is given by

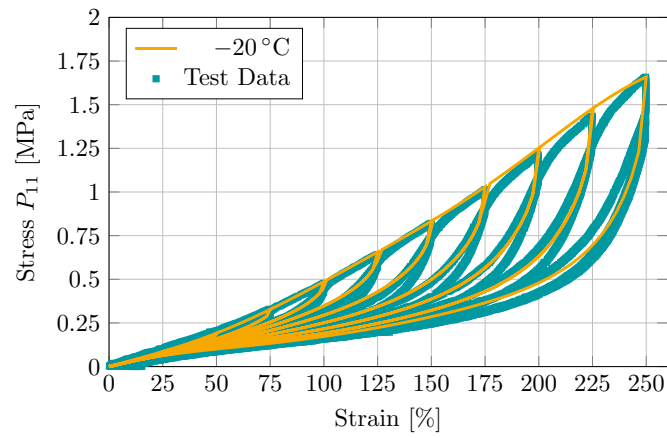
$$\begin{aligned} \Psi(\mathbf{I}_C, \tilde{T}) = & \\ 0.69 \left(0.07 \mathbf{I}_C + \tilde{T} - 0.38 + \frac{0.13}{\tilde{T}} \right) \ln(0.46 \mathbf{I}_C) \ln \left(1.48 \sqrt{0.38 \mathbf{I}_C - 1} \right), \end{aligned} \quad (6.7)$$

and depends only on the first invariant \mathbf{I}_C and the scaled temperature \tilde{T} . This is due to the fact the evaluation is based on the uniaxial tension data where the second invariant is generally not necessary. Note that this important behavior of the strain energy function (whether or how it depends on the second invariant) cannot be studied by using other machine learning approaches like for example artificial neural networks. Furthermore, the strain energy function can be simplified into two additive terms given by

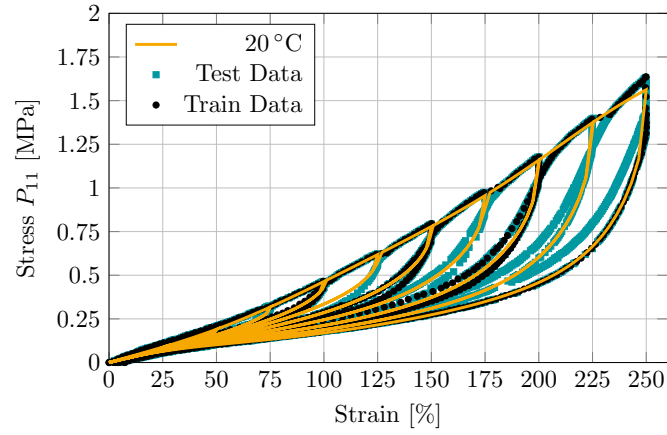
$$\Psi(\mathbf{I}_C, \tilde{T}) = \Psi_1(\tilde{T})\Psi_2(\mathbf{I}_C) + \Psi_3(\mathbf{I}_C), \quad (6.8)$$



(a)

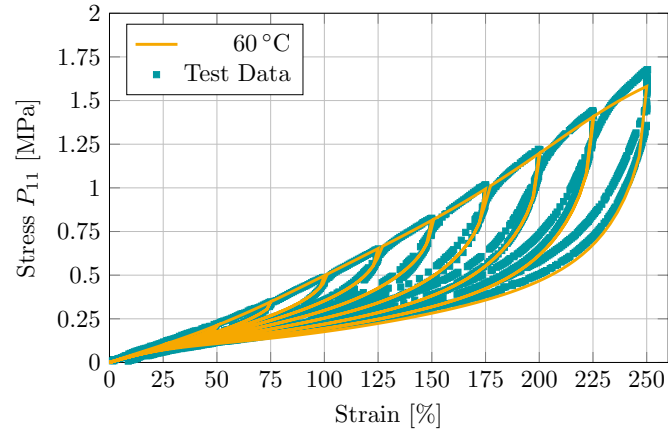


(b)

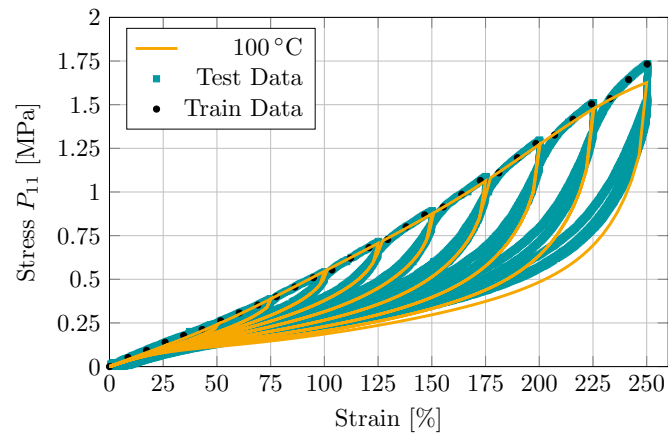


(c)

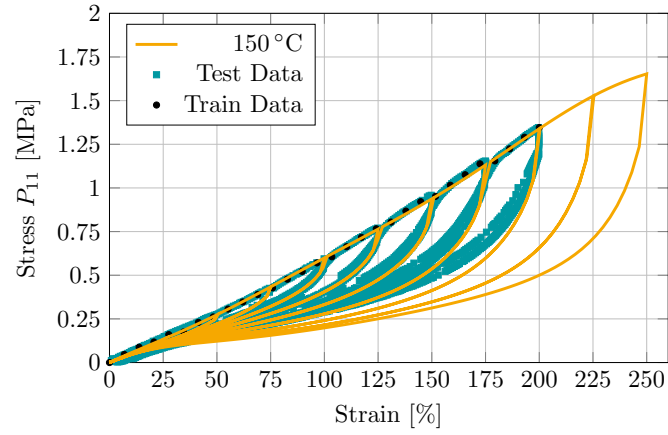
Fig. 6.6: Temperature-dependent cyclic stress-strain responses for a filled silicone subjected to stepwise increasing strain amplitudes at different temperatures. The comparison includes the stress-strain responses predicted by the model described in Equation 6.3 and Equation 6.6 obtained using DSO, alongside experimental data at -40.00°C , -20.00°C and 20.00°C [110].



(a)



(b)



(c)

Fig. 6.7: Temperature-dependent cyclic stress-strain responses for a filled silicone subjected to stepwise increasing strain amplitudes at different temperatures. The comparison includes the stress-strain responses predicted by the model described in Equation 6.3 and Equation 6.6 obtained using DSO, alongside experimental data at 60.00 °C, 100.00 °C and 150.00 °C [110].

where

$$\Psi_1(\tilde{T}) = 0.69 \left(\tilde{T} - 0.38 + \frac{0.13}{\tilde{T}} \right), \quad (6.9)$$

$$\Psi_2(I_C) = \ln(0.46I_C) \ln \left(1.48 \sqrt{0.38I_C - 1} \right), \quad (6.10)$$

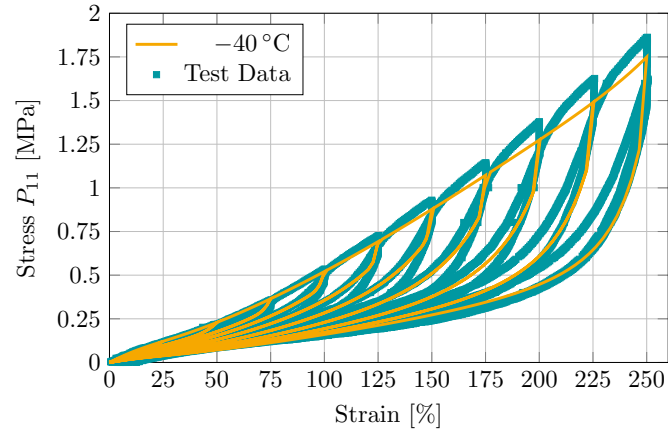
$$\Psi_3(I_C) = 0.05I_C\Psi_2(I_C). \quad (6.11)$$

From the obtained expression it is directly visible that the proposed strain energy would become unstable for values of $I_C < 2.63$, which cannot be reached under the incompressibility constraint. This direct stability analysis represents a significant advantage for example in comparison to the above mentioned artificial neural networks. In addition, the expression is not defined for the temperature $T = -100.00^\circ\text{C}$. It can be seen that the term $\tilde{\Psi}_3(I_C)$ represents an average response of the material independent of temperature. The term $\tilde{\Psi}_1(\tilde{T})\tilde{\Psi}_2(I_C)$ is solely responsible for all (non-linear) temperature effects. The resulting damage variable for this particular example has been identified by

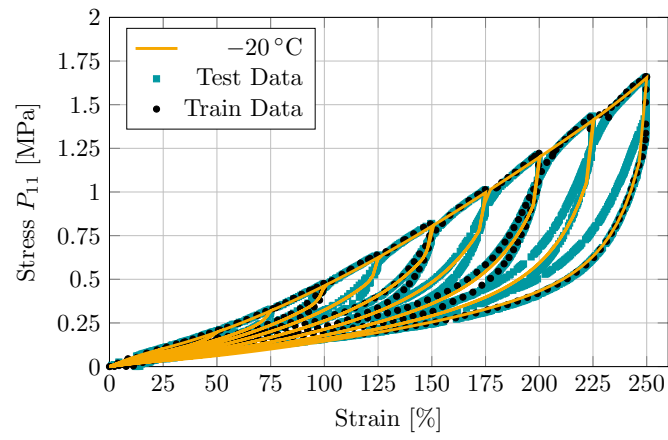
$$\begin{aligned} \eta_T(\Psi, \Psi_{\max}) = & \\ & - 5.73 + 16.36 \exp \left(- \tanh \left(\ln \left(-\Psi + 1.77 \exp \left(-\Psi + \Psi_{\max} + \operatorname{erf}(0.39\Psi) \right) \right) \right) \right. \\ & \left. + \tanh(1.38 \exp(-30.32\Psi + 30.29\Psi_{\max})) \right) \Bigg). \end{aligned} \quad (6.12)$$

The material response for all temperatures is plotted in Figure 6.8 and Figure 6.9. The R^2 score for the primary loading and unloading curve reached 98.10 % and 93.40 %, respectively. The derived model fits the primary loading curve of the training data well and interpolates well within the specified range between -20.00°C and 100.00°C , although there are slight deviations from the test data at -40.00°C and 150.00°C . The calculated damage variable accurately describes the unloading responses, although the last unloading cycle is underestimated for both the 60.00°C and 100.00°C temperatures.

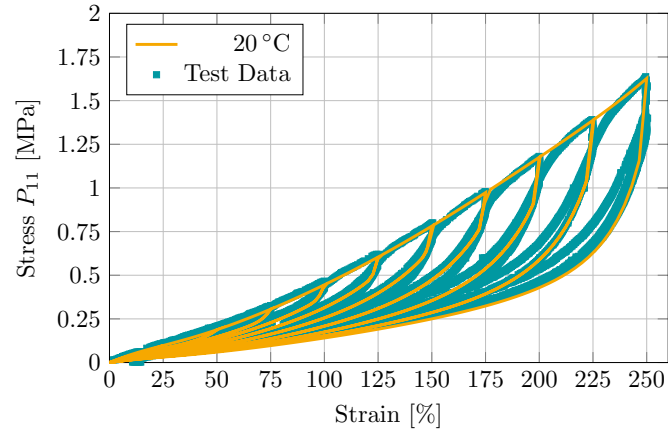
Thus, the proposed method demonstrates a robust ability to accurately generalize the material response with respect to temperature dependence, despite being trained on only three temperature curves. This performance is particularly remarkable under conditions of extreme data scarcity. In a broader application, whether for use in finite element simulations or in more general contexts, it is advisable to calibrate the material model over the entire available temperature range.



(a)

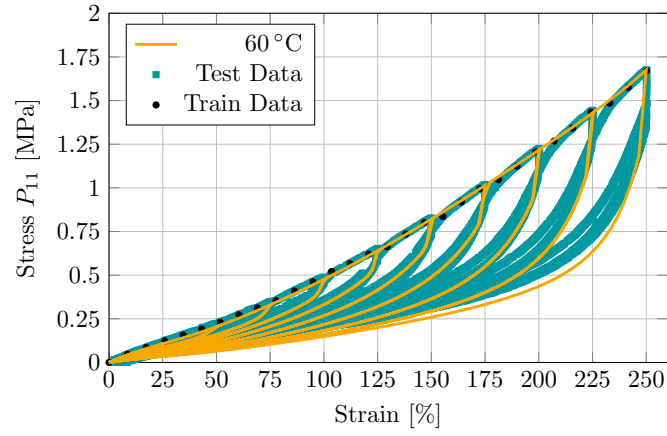


(b)

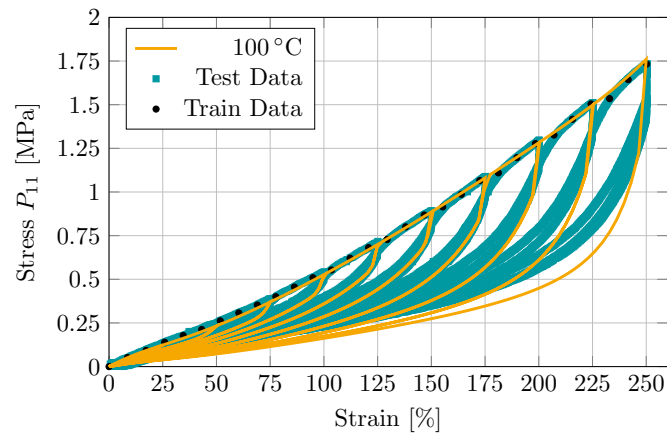


(c)

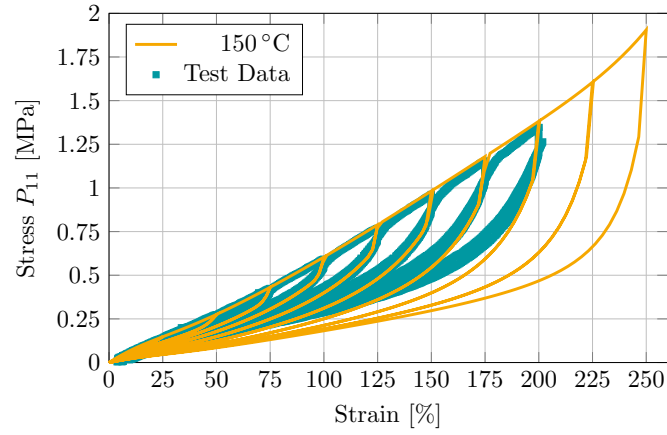
Fig. 6.8: Extrapolation assessment for temperature-dependent cyclic stress-strain responses for a filled silicone subjected to stepwise increasing strain amplitudes at different temperatures. The comparison includes the stress-strain responses predicted by the model described in Equation 6.7 and Equation 6.12 obtained using DSO, alongside experimental data at -40.00°C , -20.00°C and 20.00°C [110].



(a)



(b)



(c)

Fig. 6.9: Extrapolation assessment for temperature-dependent cyclic stress-strain responses for a filled silicone subjected to stepwise increasing strain amplitudes at different temperatures. The comparison includes the stress-strain responses predicted by the model described in Equation 6.7 and Equation 6.12 obtained using DSO, alongside experimental data at 60.00 °C, 100.00 °C and 150.00 °C [110].

7 Microstructural Aerogel Modeling

Mr. Charles Learned and I, with the kindly assistance and advice of Prof. J. W. McBain, undertook to test the hypothesis that the liquid in a jelly can be replaced by a gas with little or no shrinkage. Our efforts have met with complete success.

S. S. KISTLER

The history of aerogels is fascinating and dates back to the first synthesis by Samuel Stephens Kistler in the 1930s [111]. In this first work, Kistler succeeded in extracting the liquid phase from the pores of a gel. Realizing that the evaporation of liquid from a gel often results in a collapsed and densified solid, he explored the possibility of replacing the gel's liquid with gas without disturbing its solid structure, a process now known as supercritical drying. This initial work laid the foundation for the development of various types of aerogels, which are now considered the lightest solid materials. In general, aerogels belong to the group of porous materials and have many fascinating properties, e.g. silica aerogels (see Figure 7.1) are characterized by a very low density ($< 0.20 \text{ g/cm}^3$), high porosity (up to 99.98 v/v) as well as low thermal conductivity (up to $0.01 \text{ W m}^{-1} \text{ K}^{-1}$), and sound velocity as low as 20.00 ms^{-1} [112]. Because of these exceptional properties, potential applications for silica aerogels include thermal insulation to reduce heat loss in buildings [113], star dust collection in spacecraft [114] as well as acoustic insulation to effectively absorb sound waves, making them useful as sound insulating materials [115]. Furthermore, aerogels can be used to create controlled-release drug carriers [116, 117] or even as catalysts in fuel cells [118]. These exceptional features are strongly influenced by the microstructure of the material, such as pore size distribution, particle connectivity, and specific surface area [119–121]. Traditional aerogel synthesis is based on existing recipes or trial-and-error approaches derived from chemical principles, which sometimes limits the exploration of new and sustainable synthesis strategies [112, 122, 123]. The synthesis of aerogels is a multi-step process, and the desired properties depend highly on the ratio of precursor materials and other control parameters, see Figure 7.2 for an schematic synthesis process. To synthesize an aerogel, the initial step involves preparing a precursor solution by combining a solvent with the precursor materials. This step is critical as it provides the starting material

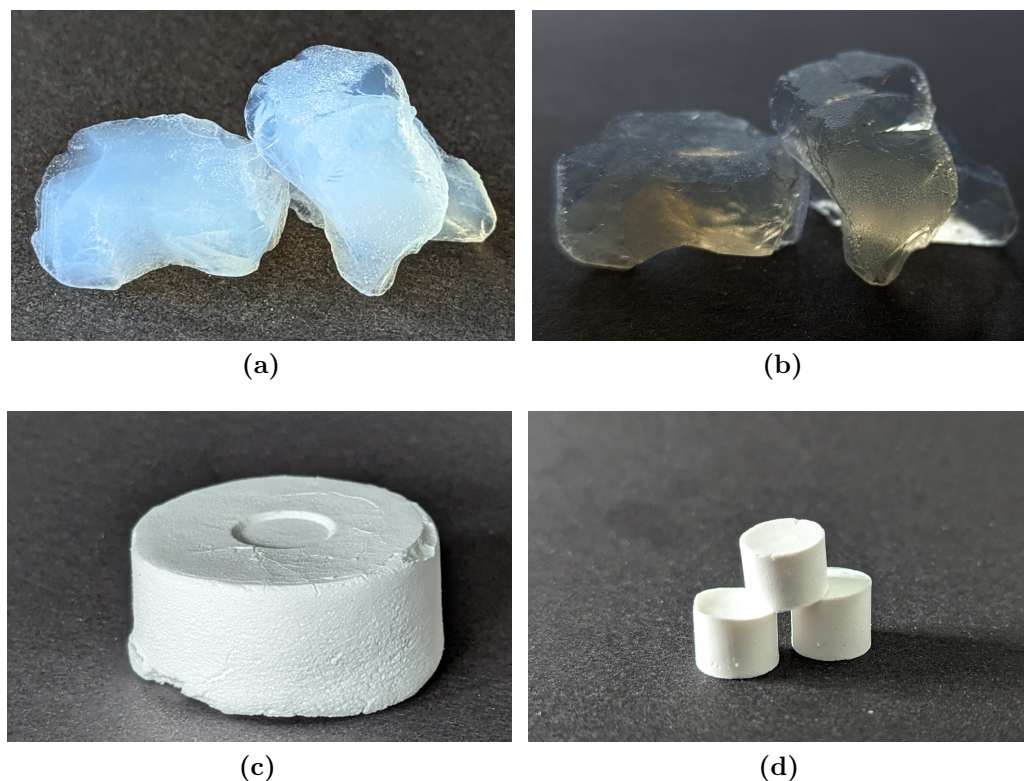


Fig. 7.1: Silica aerogel samples observed under different lighting conditions to demonstrate Rayleigh scattering phenomena: (a) with light illuminated from above and (b) with light illuminated from behind. Additionally, the figure includes images of (c) a marshmallow aerogel sample and (d) three corn starch aerogel samples.

for the aerogel formation. The gelation process occurs after the precursor solution is created. This process transforms the solution into a 3D network that creates the structural framework of the aerogel. Next, a solvent exchange is performed. The initial solvent used in the gelation process is replaced with a different solvent or solvent mixture that is more compatible with the drying conditions. Finally, the gel is dried either using supercritical drying or special ambient drying, freeze-drying or evaporation. Ideally, the process ensures that the gel's nanoporous morphology is preserved.

Due to the many steps and highly complex relations of the synthesis process, a comprehensive understanding of the structure-property relationships in aerogels is to this day lacking, making it difficult to predict the behavior of these materials under different environmental and loading conditions. Therefore, the ability to optimize the microstructure of silica aerogels through targeted synthesis and, in turn, to tailor their properties for a given application remains a significant challenge.

The properties of aerogels also highly depend on the type of aerogel. Generally, aerogels can be classified into two main types: organic aerogels and

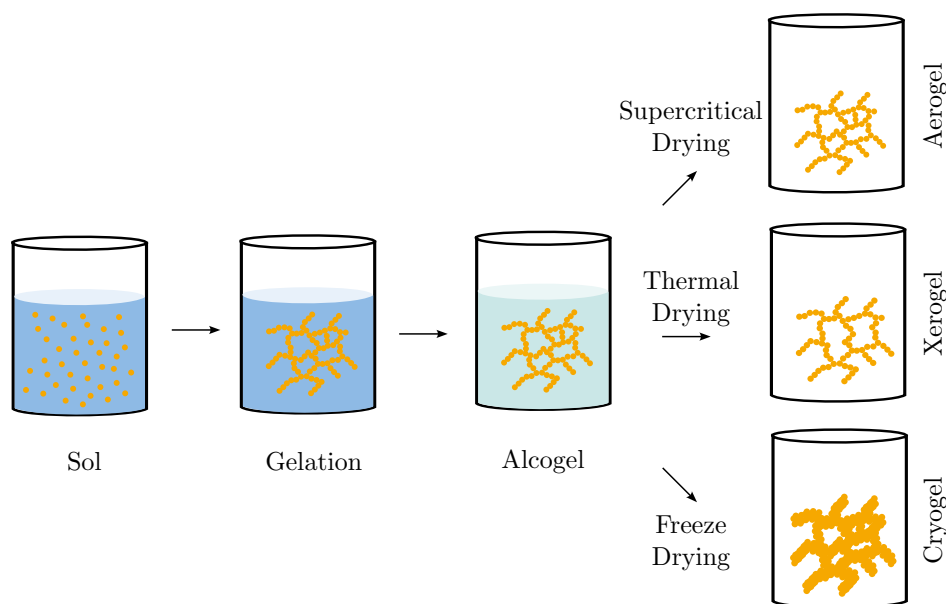


Fig. 7.2: Schematic representation of a conventional aerogel synthesis process, based on [122]. The process begins with the creation of a sol by mixing a solvent with precursor materials. Following gelation, solvent exchange is performed on the hydrogel, often using ethanol, to produce an alcogel. In the final step, drying is carried out, which can be achieved through supercritical drying, special ambient drying, freeze-drying, or evaporation.

inorganic aerogels (see Figure 7.3) [124, 125]. Organic aerogels are primarily composed of organic polymers or carbon-based materials. Commonly used precursor materials include resorcinol-formaldehyde, melamine-formaldehyde, or polyurethane. One major advantage of organic aerogels is their biocompatibility and suitability for use in biomedicine, drug delivery, and tissue engineering applications [124, 126–128]. Inorganic aerogels are composed primarily of inorganic materials, such as metal oxides (e.g., silica, alumina), metal chalcogenides (e.g., tellurium, selenium), or metal carbides (e.g., silicon carbide). Inorganic aerogels offer several advantages, including their high surface area as well as their thermal insulation properties, see [129] as well as references therein.

The type of aerogel significantly affects its morphology, with a distinction being made between colloidal-like aggregated structures and fibrillar-like cellular formations, see Figure 7.4 for the microstructural differences between κ -carrageenan and silica aerogels. Furthermore, minor changes in the synthesis parameters can result in significantly different properties. Since the early 1990s, various modeling techniques have been used to understand the mechanical structure-property relationships of aerogels. These approaches include molecular dynamics (MD), coarse-grained (CG), micro-mechanical multiscale, and continuum mechanics modeling. Initial efforts were constrained

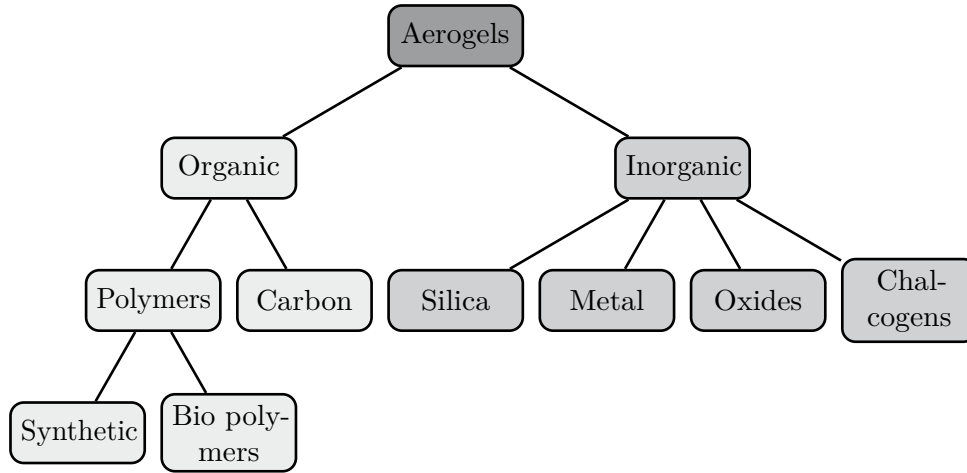


Fig. 7.3: Classification of aerogels into organic and inorganic, based on [124]. Organic aerogels are classified into two main categories: polymers and carbon-based aerogels. The former are further subdivided into synthetic or biopolymers. Inorganic aerogels are composed of silica, metal, oxides and chalcogenides.

by computational limitations and data availability. Classical MD simulations provide insight into nanoscale behavior, but face challenges in extrapolating to macroscale properties. Despite their ability to accurately capture atomic-scale dynamics, MD simulations are computationally expensive and time-consuming. CG models reduce the computational burden, but require careful validation against experimental data. These modeling approaches share the common goal of determining the structure-property relationships of aerogels in order to optimize their performance in various applications, with a focus on increasing mechanical stiffness while minimizing thermal conductivity.

One of the primary goals of current research is to explore methods for designing tailored materials (see Figure 7.5). A potential approach is to digitally model various aerogel structures in an effort to identify their fundamental properties at the microscale. This involves integrating various variables such as relative density, particle radius, and pore size distribution into these computational models. In the following section, the potential to investigate the influence of these input parameters and to formulate a predictive model for the mechanical behavior through deep symbolic regression will be explored. This approach provides an opportunity to optimize mechanical properties and manufacture tailored microstructures by establishing correlations between input parameters and actual material properties.

Mechanical properties of aerogels are often described by a power-law relationship. The commonly used power-law relationship between Young's modulus E and relative density c or the solid fraction ϕ_s is expressed as

$$E \propto c^m \quad \text{or} \quad E \propto \phi_s^m, \quad (7.1)$$

where m denotes the scaling exponent. While the open-cell foam model of Gibson and Ashby yields $m = 2$ [130], aerogels characterized by random network connectivity deviate from the idealized network structure of this model. For such materials, the value of m typically ranges between 2 and 4, as shown by Groß and Fricke [131]. The effect of density on the mechanical properties of silica aerogels was further investigated by Wong et al. who observed increased brittleness at higher aerogel densities [132].

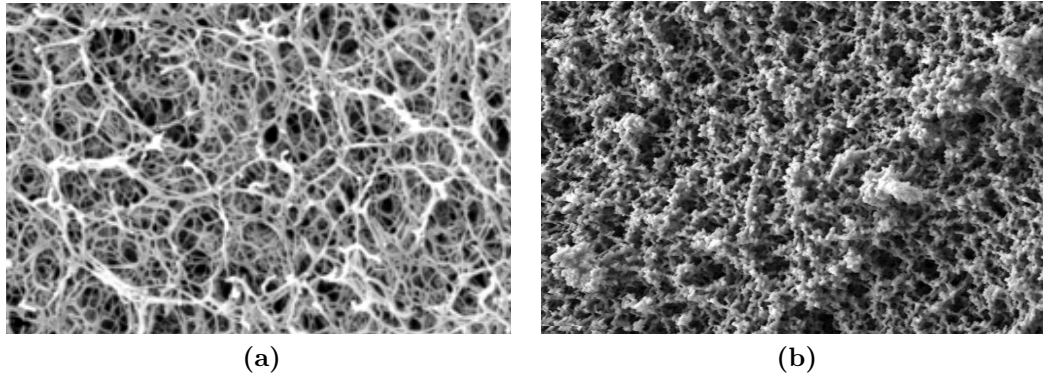


Fig. 7.4: SEM images of (a) κ -carrageenan aerogel and (b) TEM image of silica aerogel showing the different microstructures. In the case of κ -carrageenan aerogel the fibrillar-like cellular formations and for silica aerogel colloidal-like aggregated structures are visible.

In the following chapter, two different modeling approaches are discussed that aim to characterize silica aerogels, representing colloidal-like aggregated structures, and κ -carrageenan aerogels, representing open-porous cellular-like formations. Both of these approaches require micro-mechanical frameworks. For silica aerogels, the diffusion-limited cluster-cluster aggregation (DLCA) method is used to construct representative microstructures, which are subsequently used in finite element simulations to determine the mechanical response in Section 7.1. In the case of κ -carrageenan aerogels, Laguerre-Voronoi tessellation (LVT) is employed to construct analogous microstructures for an open-porous cellular like network and the results are presented in Section 7.2. Validation and calibration of both modeling approaches depend on experimental data including microstructural characterization and macroscopic mechanical behavior. In addition, a computational data set based on micro-mechanical attributes such as relative density or pore size distribution is generated to provide input to micro-mechanically motivated models. As a result, the direct parameters effects on the mechanical properties can be identified. The micro-mechanically motivated models will be identified using the `textttDSO` package, followed by a comprehensive discussion of the implications of the derived models. Parts of this chapter have been previously presented in my published work [2, 5, 6].

To correlate the mechanical responses only the uniaxial compression case will be considered. Therefore, the deformation gradient can be expressed using

$$\mathbf{F} = \begin{bmatrix} \lambda & 0 & 0 \\ 0 & 1 - \nu(\lambda - 1) & 0 \\ 0 & 0 & 1 - \nu(\lambda - 1) \end{bmatrix} \mathbf{e}_i \otimes \mathbf{e}_j, \quad (7.2)$$

where λ is the applied stretch, ν is the Poisson's ratio and \mathbf{e}_i and \mathbf{e}_j with $i, j = 1, 2, 3$ are two orthonormal vectors. To determine an appropriate strain energy function, this deformation gradient for uniaxial compression is considered. Note that, cellulose aerogels demonstrate the nearly zero Poisson effect while the Poisson's ratio for silica aerogels has been reported ranging between $\nu = 0.20 - 0.22$ [133, 134].

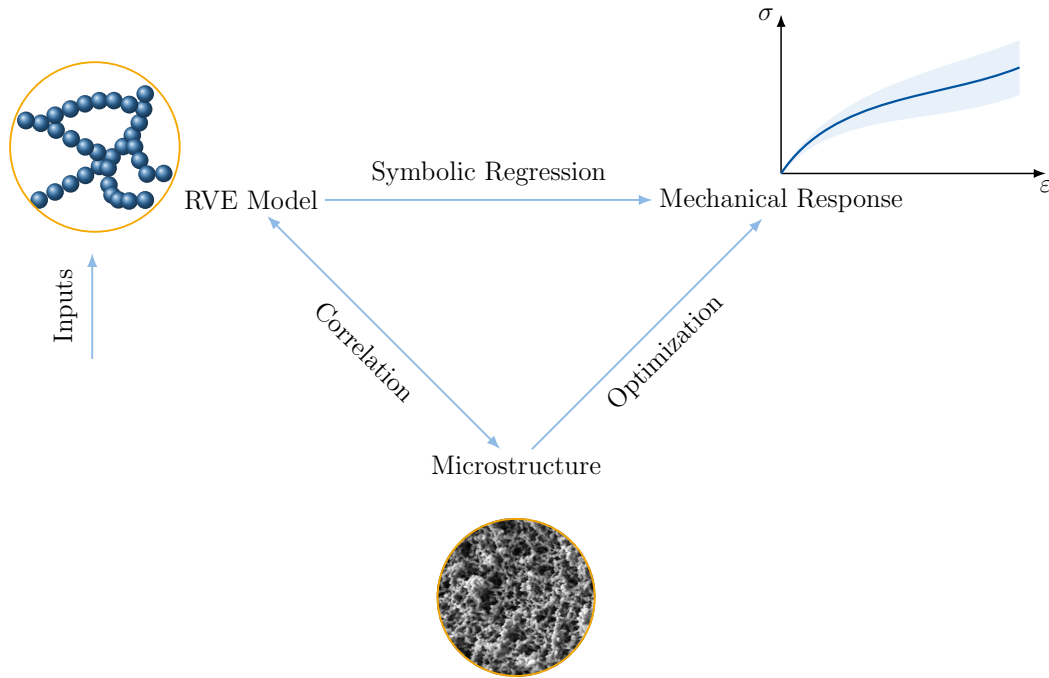


Fig. 7.5: Schematic representation of the RVE-based modeling approach employed to investigate the influence of input parameters on aerogel microstructures and their mechanical response through SR.

7.1 Modeling of Silica Aerogels Using Aggregated Structures

Silica aerogels are characterized by a fractal nature, exhibiting homogeneous macroscopic properties alongside mass distributions that exhibit fractal characteristics as a result of primary particle aggregation. The determination of

their fractal nature is often based on techniques such as small-angle X-ray scattering (SAXS) or small-angle neutron scattering (SANS) experiments, where the scattering curves reveal distinct regimes. In particular, the intermediate regime allows direct determination of the fractal dimension from the slope of the double logarithmic plot of the scattering curve. Classical supercritically dried silica aerogels are typically characterized by very low densities (around 100 kg m^{-3}) corresponding to high porosities around 95.00 % [133]. In combination with typical pore sizes below 100.00 nm, silica aerogels have attracted considerable attention, specifically for thermal insulation applications, but also for cosmic dust capture and drug delivery [135, 136]. There is considerable literature on the structural and mechanical properties of silica aerogels [112, 131–133, 137–143]. Most of these reports are experimental in nature while only very few theoretical investigations have been thus far reported. Silica aerogels deform elastically under small strains, however under large strains, they undergo irreversible plastic deformation. To characterize aerogel structures, the commonly utilized parameters are the pore size distribution, fractal dimension, and cluster correlation length.

Computational modeling has played a key role in investigating the mechanical and fractal features of aerogels. Different modeling tools applied in this context include molecular dynamics simulations [142, 144, 145], coarse-grained hard-sphere aggregation approaches [141, 146–149], flexible coarse-grained approaches [150–152], constitutive models [153], as well as multiscale models [154].

The sol-gel process for silica aerogels involves the assembly of small particles to form clusters and networks. As such, this process can be modeled by means of the aggregation mechanism. A number of particle-based aggregation algorithms have been developed, including diffusion-limited aggregation (DLA), reaction-limited aggregation (RLA), diffusion-limited cluster-cluster aggregation (DLCA), reaction-limited cluster-cluster aggregation (RLCA), ballistic aggregation, and others. Hasmy et al. investigated the potential of various algorithms for modeling silica aerogels [146, 147]. Their findings indicate that the shape of the experimental scattering curve is qualitatively well reproduced by cluster-cluster algorithms. The use of DLCA for modeling silica aerogels builds upon the foundational work of Kolb and Herrmann [155]. Furthermore, Ma et al. extended this approach to describe the bulk mechanical properties of silica aerogels and examine the influence of dangling bonds on network behavior [141, 148, 149]. They concluded that dangling mass does not significantly affect the scaling exponent. By subjecting DLCA networks to hydrostatic compression, they explored the relationship between density and bulk modulus. Despite numerous studies attempting to characterize silica aerogels using DLCA, there remains a lack of consensus regarding the impact of different model parameters on resulting morphology and finite deformation under mechanical loads. A primary objective is to elucidate the role of network

connectivity in load-transfer pathways and to comprehensively describe the bulk mechanical properties of silica aerogels.

7.1.1 Diffusion-Limited Cluster-Cluster Aggregation

A number of aggregation algorithms can be used to model particles undergoing random walks due to Brownian motion and the formation of clusters, which in turn form aggregates that are the building blocks of the network. The sol-gel process utilized to synthesize silica aerogels follows a comparable clustering process. The findings of Hasmy et al. indicate a close alignment between structures generated from DLCA and the scattering data of silica aerogels [146]. Consequently, this study will employ the DLCA algorithm to model silica aerogel networks. The methodology of the algorithm is explained below and illustrated in Figure 7.6. As a starting point for the method, a box with periodic boundary conditions has to be defined. Within this box a total number of $N_{\text{all}} = N_s + N_w$ seeds and walker particles are initialized (see Figure 7.6(a)). These particles can be placed randomly or in an arranged way within the box. In this example the particles are initialized on random points and they can move freely according to the random walk theory in 3D space. Initially, the DLCA algorithm was developed for a on-lattice approach, meaning that the particles could only jump to specific grid points in the 3D bounding box. In this example, an off-lattice algorithm was implemented. The step sizes for the seed and walker particles s_s and s_w are given as the norm of the distance vector $\Delta \mathbf{x}$ of three Gaussian randomly distributed components Δx , Δy and Δz given by

$$s_s = s_w = ||\Delta \mathbf{x}|| \quad \text{with} \quad \Delta \mathbf{x} = \frac{1}{\sqrt{\Delta x^2 + \Delta y^2 + \Delta z^2}} \begin{pmatrix} \Delta x \\ \Delta y \\ \Delta z \end{pmatrix}.$$

Thus, the next direction of each particle movement is evenly sampled from the surface of a sphere at the distance of the step sizes s_s or s_w . Moreover, the off-lattice algorithm requires the introduction of a parameter $\varepsilon_{\text{crit}}$, which represents the critical distance between a walker and a seed particle. Upon reaching this distance, the Brownian motion of the walker is terminated, allowing it to diffuse towards the seed particle and bind with it. Note that, aging of aerogels has shown to influence the neck-growth between the particles in the aerogel network [156, 157]. This neck-growth can subsequently be modeled within a finite element framework as the growth in the bond beam diameter d_{bond} . Additionally, a sticking probability p_s can be provided to model the cluster diffusion. In this analysis the sticking probability is $p_s = 1$, thus the walker particles always stick once the critical distance is undershot. With time, all the walkers diffuse to the seeds and clusters are formed (see Figure 7.6(b) – (c)).

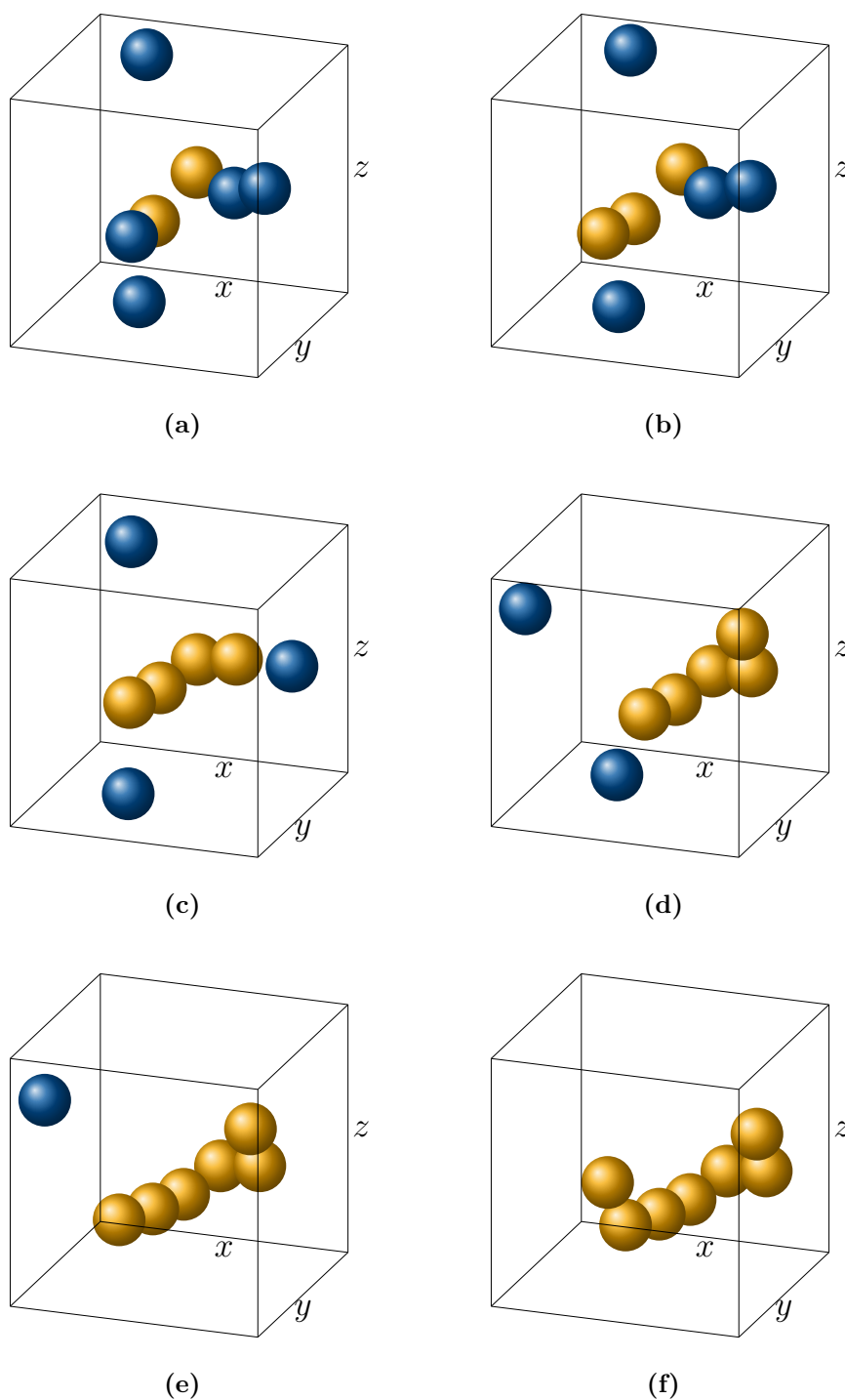


Fig. 7.6: Visualization of DLCA algorithm where (a) walkers (blue) and seeds (orange) are initialized in a given 3D domain, (b)-(e) illustrate the sequential diffusion of walkers towards the seeds leading to aggregation and cluster formation, (f) shows the final aggregated structure, where all walkers and seeds have coalesced into a single domain-spanning aggregate.

As soon as two particles of two different clusters likewise exceed this critical distance $\varepsilon_{\text{crit}}$, the two clusters are connected to form one single cluster [141] (see Figure 7.6(d) – (e)). Hence, the term cluster-cluster aggregation is used based on the algorithm proposed by Meakin [158]. All particles continue to move until all walkers are connected in a cluster and all clusters are connected to each other (see Figure 7.6(f)). In this example, the particles exhibit continuous movement in space. Consequently, a total of seven parameters can be varied: the radius of particles r , the critical distance $\varepsilon_{\text{crit}}$, the number of walkers N_w , the number of seeds N_s , the seed step s_s , the walker step s_w and the box size L . Given that particles can be initialized at random positions, the aggregate structure is subject to randomness, which in turn influences the mechanical response. The implementation in MATLAB was carried out using an object-oriented approach. To quantify the relative density of the generated structures, the volume of all particles V_p in ratio to the volume V_b of the simulation box was calculated by

$$c = \frac{V_p}{V_b} = \frac{4\pi N_{\text{all}} r^3}{3L^3}, \quad (7.3)$$

where r denotes the particle radius and L is the box size. The porosity, evaluated as $\phi = 1 - c$ for the generated structures with different relative densities needs to be in agreement with the corresponding values of the synthesized aerogels.

As silica aerogels are very good examples of fractal material, the computationally generated and chemically synthesized structures can be correlated by comparing their fractal properties. The latter can be quantified by the fractal dimension d_f , a parameter which characterizes the geometric properties of a structure by describing its self-similarity across different length scales. There are several methods for calculating d_f . One such method requires the calculation of the mass $m(r)$, of particles within a sphere of radius r . By varying the radius of the sphere and subsequently measuring the logarithmic increase in $m(r)$, one can observe that the relationship between $m(r)$ and r follows a power law given by

$$m(r) \propto r^{d_f}, \quad (7.4)$$

where the slope of the resulting curve, when plotted on a log-log scale, corresponds to the fractal dimension d_f . Once the fractal dimension has been determined for a given density of a silica aerogel, it can be correlated with values obtained from experimental SAXS curves. A primary objective in this context is to further investigate the influence of the relative density on the fractal dimension.

Exemplary aggregated structures for the concentrations of $c_1 = 10.00\%$, $c_2 = 8.75\%$, $c_3 = 7.50\%$ and $c_4 = 6.25\%$ are depicted in Figure 7.7. They

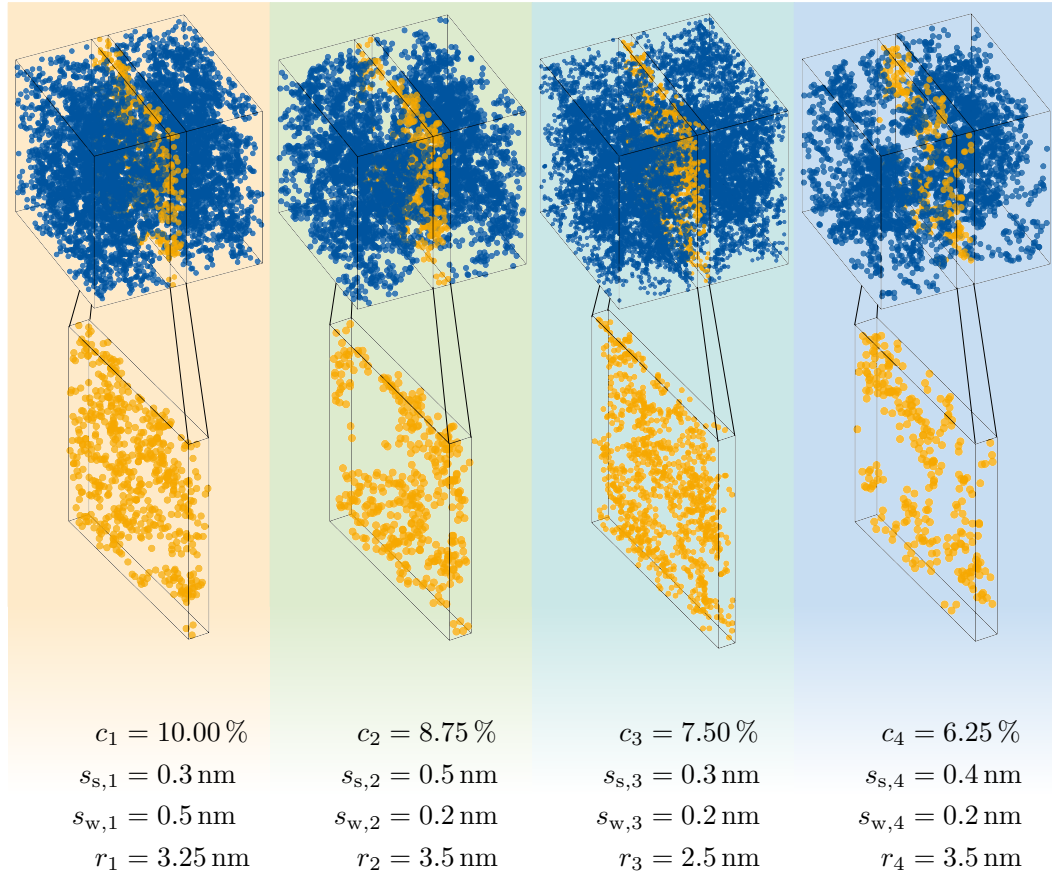


Fig. 7.7: Visualization of four aggregated structures at varying concentrations. Each structure is depicted with its 3D particles and includes a cross-sectional view through the center to highlight the internal connectivity.

have been chosen from a pool of a total of 1708 aggregates that have been generated using the DLCA algorithm [2]. The 3D network of each aggregated structure together with a cross-section visualization is shown in the center. The random network connectivity and high porosity within the network is clearly visible. In the simulation box, it may appear that a few particles are unconnected and isolated. However, these are, in fact, connected to other particles within the clusters through periodic boundary conditions. The connectivity of all particles within the simulation box was validated to guarantee that the generated aggregated structure accurately represents the microstructure of actual silica aerogels. Note that, a simulation box with the edge length $L = 200.00 \text{ nm}$ was chosen.

7.1.2 FE-Based Microstructure Analysis

In order to describe the mechanical properties of the generated aggregates, the finite element method (FEM) was utilized. Given the geometry of the

structures, the information about all particle positions and all connections between the particles was known *a priori*. In order to perform a FEM simulation, a representative volume element (RVE) was created. Its dimensions corresponded to the dimensions of the DLCA simulation box. The particles that originated from the DLCA algorithm were treated as nodes, while the bonds were modeled as beams. The FEM program ABAQUS was used, and the beam element type B31 based on the Timoshenko beam theory was applied. Beam elements are a useful choice as they are capable of reflecting the full range of deformation modes that a bond can undergo, which are bending, torsion and stretching. Young's modulus and Poisson ratio of the beams were specified as $E = 10^5$ Pa and $\nu = 0.29$, respectively [141]. In the implementation of the DLCA algorithm, the boundary surfaces of the box were subjected to periodic boundary conditions. Nevertheless, this does not ensure the existence of particles on the boundary. In order to generate periodic nodes, any connection between two particles that crossed a boundary surface was filtered. For each node on a boundary surface, a complementary node was created on the corresponding surface. The particle connections were separated with exact precision on the surface of the boundary, and a new node was subsequently generated. The newly generated nodes were stored in a dedicated set of periodic boundary nodes. Subsequently, the previous particle connection was removed, and two new connections were established with the intermediate node on the boundary surface. It should be noted that the particle position is additionally adjusted during the aggregation process in order to prevent particle overlap. This is a beneficial step to avoid the formation of very small elements, ensuring that the distance between the aggregated particles is precisely equal to the sum of their radii. It is crucial to emphasise that each node is characterised by six degrees of freedom, consisting of three translational and three rotational degrees of freedom. Furthermore, the degrees of freedom at the box boundaries are coupled through periodic boundary conditions by the use of dummy nodes. Therefore, three dummy nodes \mathbf{X}^A , \mathbf{X}^B and \mathbf{X}^C are defined. Each node corresponds to a surface pair of the box, e.g. \mathbf{X}^A couples all degrees of freedom on the left and right surface of the box. With $\boldsymbol{\theta} = (x \ y \ z \ \phi_x \ \phi_y \ \phi_z)^\top$ representing the degrees of freedom the coupling conditions are given by:

$$\boldsymbol{\theta}^{\text{left}} - \boldsymbol{\theta}^{\text{right}} = \mathbf{X}^A, \quad (7.5)$$

$$\boldsymbol{\theta}^{\text{top}} - \boldsymbol{\theta}^{\text{bottom}} = \mathbf{X}^B, \quad (7.6)$$

$$\boldsymbol{\theta}^{\text{front}} - \boldsymbol{\theta}^{\text{back}} = \mathbf{X}^C. \quad (7.7)$$

These conditions are implemented as *Equations in ABAQUS. Moreover, a point at the center of the RVE was fixed, resulting in the RVE experiencing expansion or compression about the center. It is possible to define frictionless contact between all beams with an additional exclusion of self contact. However,

as the RVE is only compressed up to 10.00 %, no significant contact between the beams occurs and therefore no effect on the initial stiffness response is noticeable. To perform the simulations input decks were created by a function in MATLAB. The RVEs were subjected to uniaxial compression, which is the common mode of deformation used to analyze the mechanical properties of silica aerogels.

Although the initial pool of aggregates was larger, convergence errors in conjunction with shorter elements and the absence of a backbone structure resulted in the generation of a simulation set consisting of only 1708.00 RVEs. This was an expected outcome, due to the randomness involved in the DLCA algorithm and the wide range of inputs provided for the generation of the data set. This resulted in structures with fewer cluster-cluster interactions, leading to localized cluster formation, which in turn led to the absence of backbone formation in certain cases. The RVEs lacking backbones are non-physical and were therefore not considered, as silica aerogels always exhibit a load-bearing backbone when exposed to compressive forces. Additionally, the data set was cleaned to remove outliers in the variance, which is introduced into the system due to the randomness involved in the DLCA process. As such, the converged 1708 samples were averaged over each sample, thus leading to a final data set of 200 structures. For the four exemplary aggregated structures visualized in Figure 7.7, it is possible to perform compression simulations up to 10.00 %. The distribution of the von Mises stress in the RVE structures of four distinct concentrations is illustrated in Figure 7.8. It is evident that a specific part of the

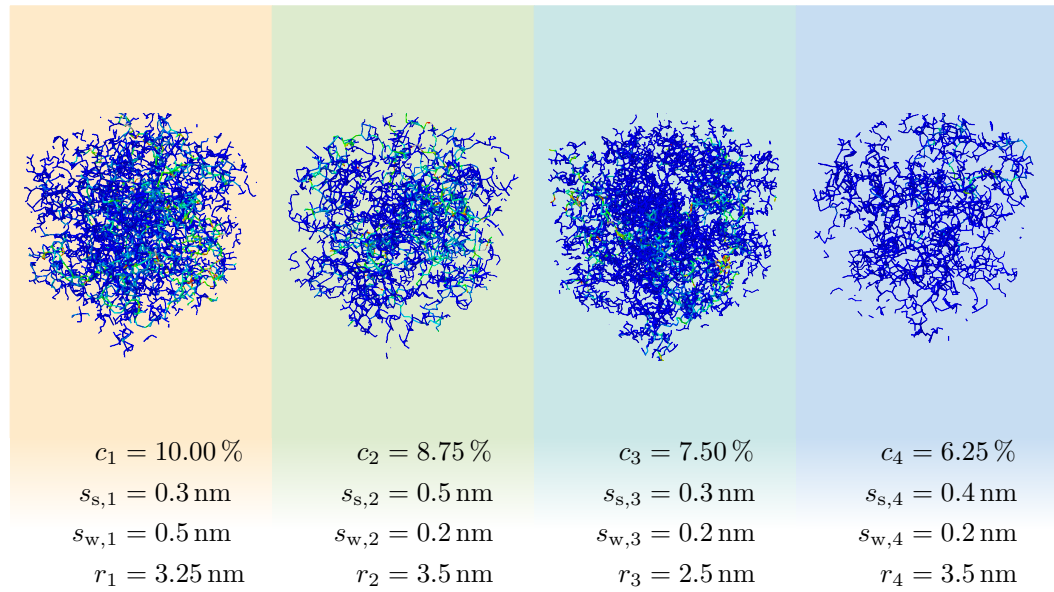


Fig. 7.8: Visualization of four aggregated structures at varying concentrations, illustrating the results from FE simulations of compression tests.

structure is primarily responsible for the load transfer. This part is called the

backbone structure of the aerogel network. In addition, it is possible to visualize the concentration-dependent stress-strain response, as well as the influence of the varying modulus of elasticity of each beam element, as illustrated in Figure 7.9. This demonstrates the influence of the concentration on the mechanical behavior. It can be observed that increasing the concentration enhances the stiffness of the aggregated structures. This seems reasonable enough following the scaling behavior observed typically in porous materials. Additionally, the scaling behavior is compared to experimental results obtained in [159]. The normalized stress response shows that the aggregated structures correspond very well to actual silica aerogels. Furthermore, the influence

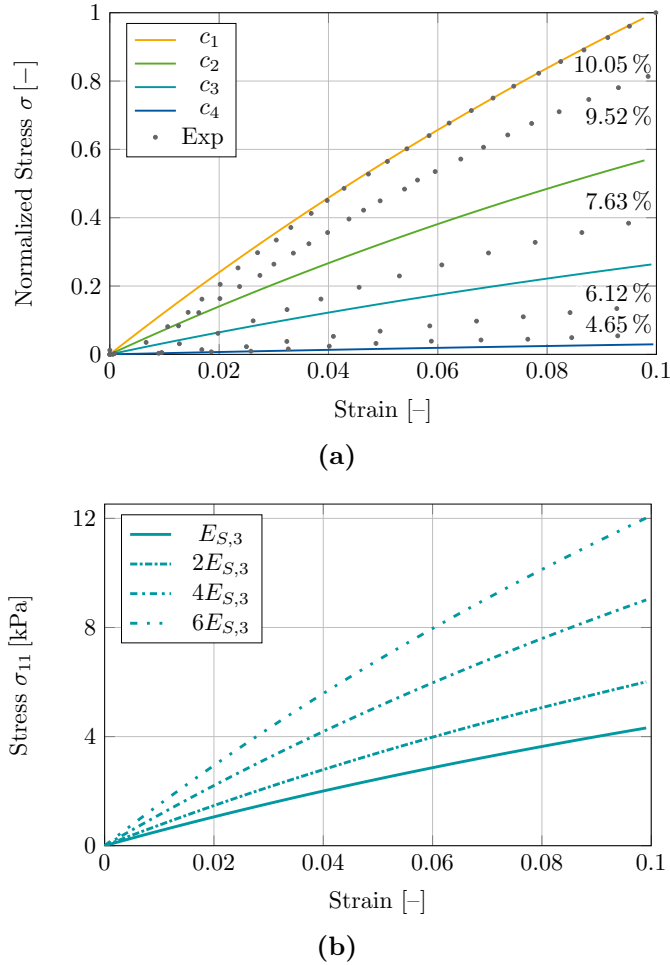


Fig. 7.9: Stress-strain responses of four aggregated structures at different concentrations, including a comparison to experimental results obtained by Wong et al. [159]. Additionally, the influence of varying modulus of elasticity for each beam element is illustrated for the aggregated structure for the concentration c_3 .

of skeletal Young's modulus is visualized for the aggregated structure of concentration c_3 (see Figure 7.9(b)). It can be seen that the stiffness of the beam elements increases directly in a linear fashion with increasing $E_{S,3}$. The

Young's modulus of the beam element can be validated through experimental measurements of the skeletal Young's modulus of silica aerogels. The observed increase in stiffness is supported by the fact that bending is the primary mode of deformation in silica aerogels, contributing significantly more to the overall stress than the other two modes. As previously demonstrated by Ma et al., within the elastic regime, the bending stress is proportional to the Young's modulus [141].

The aggregated structures generated by DLCA can be considered comparable to those of actual silica aerogels only if the material morphology and chemical kinetics are subjected to multi-dimensional validation. Accordingly, both aspects should be correlated with and compared to experimental data, as illustrated in Figure 7.10. Figure 7.10(a) describes the validation of the scaling exponent of the elastic modulus of the silica aerogel microstructure. The exponent of 3.95 (calculated for different concentrations of aggregates with $r = 3.00$ nm, $s_s = 0.30$ nm and $s_w = 0.30$ nm) in this study closely aligns with the exponent of 3.80 obtained from experimental measurements. Moreover, it can be seen in 7.10b(a), that the DLCA gelation kinetics qualitatively describes the post-nucleation sol-gel growth of the structure. In the computational model, the aforementioned kinetics are influenced by the step size of the walkers, with a larger step size resulting in accelerated growth. Consequently, the step size serves as a numerical representation of the influence of temperature on the secondary particles. As a result, the presented model structures exhibited similar characteristics to those of silica aerogels. The scaling exponent can be compared to the results of molecular dynamics simulations and other coarse-grained approaches, as well as to experimental results obtained in previous studies, as listed in Table 7.1. It is not uncommon for MD simulations to yield a relatively modest scaling exponent. The methodology presented here, which employs DLCA and FEM, demonstrates superior agreement in this regard. Moreover, the obtained data set is characterized by a box plot and a correlation matrix, as illustrated in Figure 7.11. It was observed that the averaging helps to remove several outliers from the data set. An interesting observations is that most of the structures have an elastic modulus between 20 to 100 kPa and many outliers exist that have quite stiff response, see Figure 7.11(a). In the case of the fractal dimension the fractality ranges between 2.62 to 2.68 for most of the aggregated structures. To understand the correlation between the DLCA parameters and material properties of the generated aggregates as well as the mechanical response, a correlation matrix was calculated, and is illustrated in Figure 7.11(b). It is immediately apparent that both particle step sizes have nearly no effect on any other parameter. This can be explained by the fact that the step size is a mathematical construct to model the influence of temperature in the gelation process, and as such it only affects the time of gelation in sol-gel processes [161]. As already known from literature there exists a positive correlation between the elastic modulus E and the concentration c , which can be itself validated from the correlation matrix [162]. The concentration has

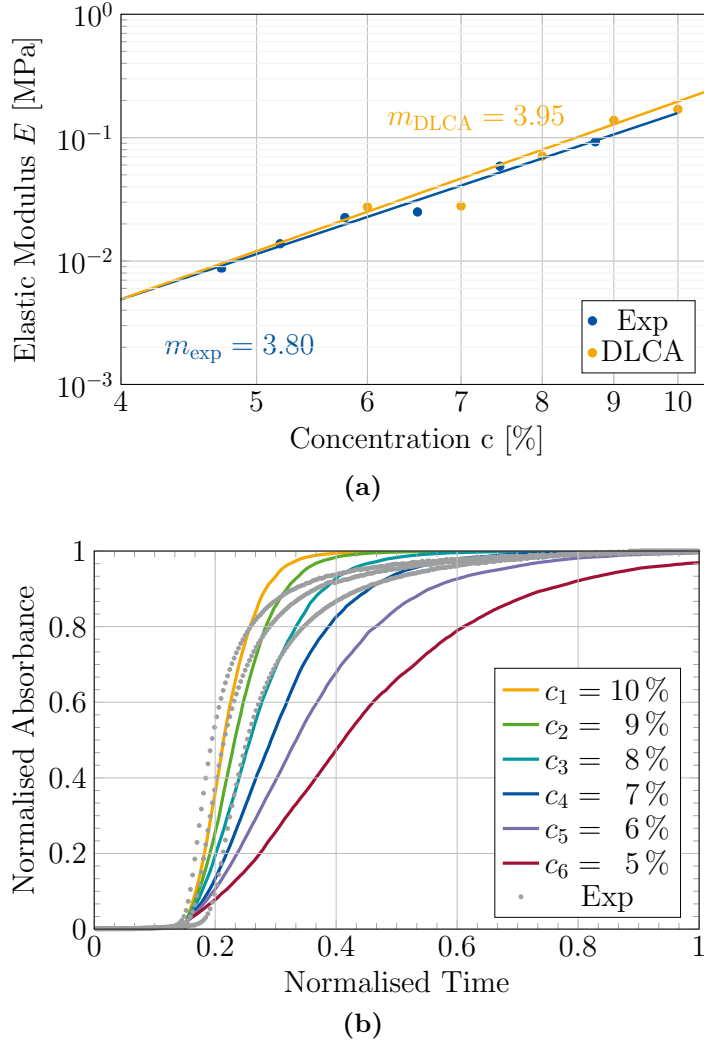


Fig. 7.10: Visualization of (a) elastic modulus as a function of concentration, with the scaling exponent determined to be $m = 3.95$, compared to experimental data from [5]. (b) shows the gelation kinetics for five different concentrations, compared to experimental data from [160].

also a positive correlation with the fractality. Furthermore, the analysis of the matrix reveals an inverse relationship between the radius and the elastic modulus.

The results obtained indicate that the concentration is the sole variable with a significant impact on the stress-strain response. Consequently, the development of a concentration-dependent model is a logical next step, which will be addressed in the following sections.

Tab. 7.1: Comparison of the the scaling exponent m obtained in this study with those reported in other modeling and experimental works. Abbreviations: CG - coarse-grained modeling, MD - molecular dynamics simulations.

	Method	Exponent m
Modeling		
This work	DLCA+FEM	3.95
Rivas-Murillo et al. [145]	MD	3.11 ± 0.21
Ferreiro-Rangel and Gelb [152]	CG	3.0 ± 0.2
Patil et al. [142]	MD	3.25 ± 0.1
Gonçalves et al. [143]	MD	3.84 ± 0.22
Experimental		
Wognier et al. [134]	SiO ₂ aerogels	3.7 ± 0.2
Groß and Fricke [131]	SiO ₂ aerogels	3.49 ± 0.07

7.1.3 Silica Aerogel Modeling

The microstructural responses, which are concentration-dependent, are employed in the derivation of a strain energy function. In order to achieve this, the deformation gradient provided in Equation 7.2 is employed. Moreover, it is essential to define the Poisson's ratio, which for silica aerogels is 0.2. In accordance with the deformation gradient, the input data consist of the three invariants I_C , II_C and J , in addition to the concentration c . The identified strain energy function is expressed as follows:

$$\Psi(II_C, c) = \frac{47.65 \exp(1.46II_C) \exp \left[\exp \left(-\frac{1044.7}{c^2} \right) \exp \left(\exp \left[2.39 \exp \frac{0.02}{II_C} \right] \right) \right]}{c + \exp(33.24 \exp(-0.33c))}. \quad (7.8)$$

Note that this model achieved an R^2 score of 98.62 %. The stress strain response is visualized in Figure 7.12. It is evident that the discovered model is capable of capturing the underlying trend and predicting a concentration-dependent stress-strain response. It is noteworthy that although three invariants were provided, only the second invariant was utilized in the model structure. This is a logical decision, given that the investigation is limited to uniaxial tension data, and therefore only one invariant is required.

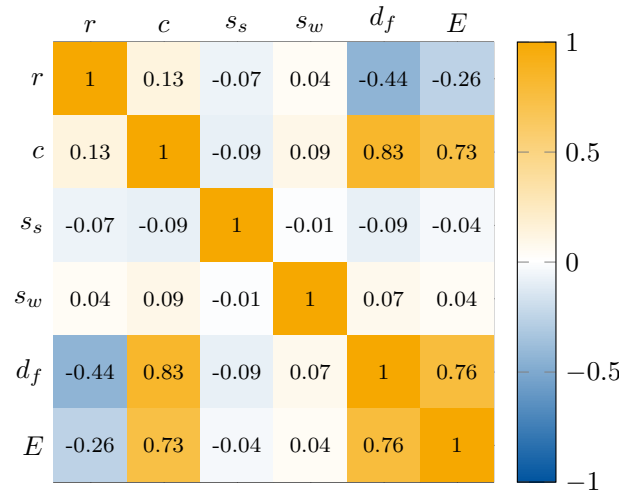
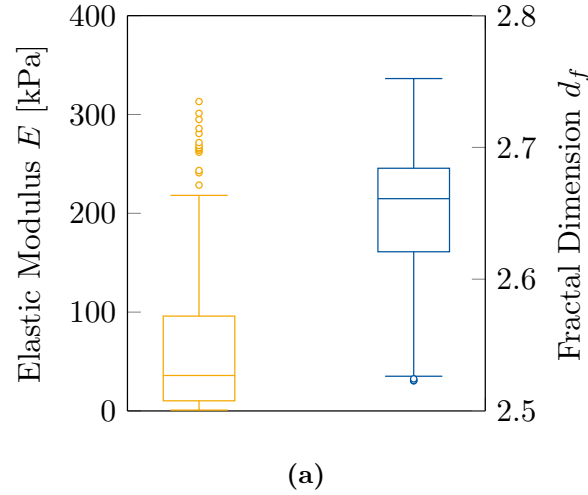


Fig. 7.11: Visualization of (a) boxplot showing the ranges for the elastic modulus E and fractal dimension d_f , after data pre-processing of all aggregated structures and (b) correlation matrix illustrating relationships between particle radius r , concentration c , seed step size s_s , walker step size s_w , fractal dimension d_f and the elastic modulus E .

7.2 Open-Porous Cellular-Like Aerogels

Open-porous cellular-like aerogels, such as κ -carrageenan aerogels, have been the subject of considerable scientific and industrial interest due to their exceptional properties. They are distinguished by ultralow bulk densities and thermal conductivities, making them highly effective for thermal insulation applications [163, 164]. Additionally, their high surface areas enhance their functionality in

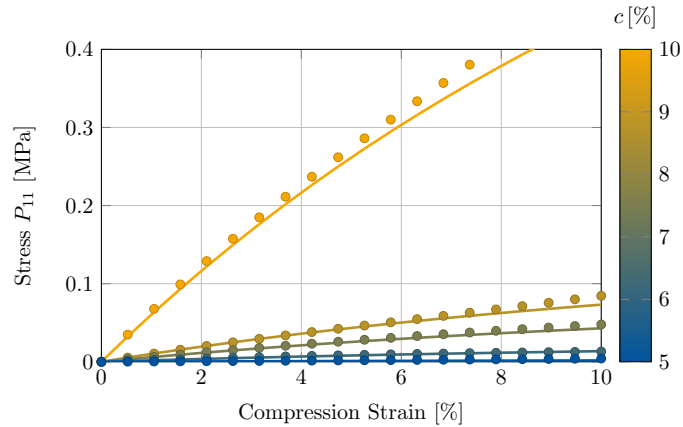


Fig. 7.12: Concentration-dependent stress-strain responses for silica aerogel based microstructures. The responses for both the training and test sets are derived from the strain energy function described in Equation 7.8.

a variety of additional applications, including filtration, oil-water separation, and CO₂ capture, as well as in catalysis [165–167]. Furthermore, the porous structure and inherent biocompatibility of these aerogels position them as promising candidates for tissue engineering and regenerative medicine [168]. The interconnected pore architecture facilitates tissue integration and vascularization, enhancing their suitability for advanced biomedical applications. Modeling open-porous cellular-like aerogels is a challenging endeavor due to the highly irregular nature of their pore structure, particularly in the case of biopolymer aerogels with pore sizes below 100.00 nm. The accurate characterization of their 3D pore structures is significantly limited by techniques such as nanoholotomography and scanning electron microscopy (SEM). The inability to reconstruct the 3D pore structure presents a significant challenge for computer simulations. A computational model was proposed by Rege et al. to describe the network structures of biopolymer aerogels using 2D Voronoi tessellations [169]. However, this approach failed to account for out-of-plane connectivity. To address these challenges, a new computational model was developed using Laguerre–Voronoi tessellation (LVT) based on random closed packing of polydisperse spheres [170, 171]. The newly developed model accurately depicts realistic 3D pore morphologies and was utilized to examine the mechanical properties of κ -carrageenan aerogels under compressive deformation. The generated data set, produced using the LVT, will be employed in this section for microstructural investigation and the identification of a strain energy function that can predict the stress-strain response based on a provided pore size distribution (PSD). This data set has been presented in [171].

7.2.1 Laguerre-Voronoi Tessellation

The generation of realistic 3D microstructures of an aerogel is achieved through the use of Laguerre-Voronoi tessellation (LVT). In the initial phase, an algorithm for the random closed packing of polydisperse spheres (RCPPS) is employed to construct a sphere-packed model box that aligns with the experimental pore-size distribution, as illustrated in Figure 7.13. The RCPPS serves as an input framework for the LVT, wherein each Voronoi cell encloses a sphere. A corrector step is introduced to adjust the volume of Voronoi cells relative to sphere volumes, thereby ensuring that the final structure closely matches the experimental pore-size distribution. Subsequently, the LVT is applied to the adjusted sphere distribution, generating a 3D Voronoi diagram that represents the aerogel's nanostructured network. This approach enables the creation of computationally designed 3D aerogel microstructures that closely resemble the real material's pore structure. The generated 3D models are then subjected to further analysis and simulations of the mechanical properties.

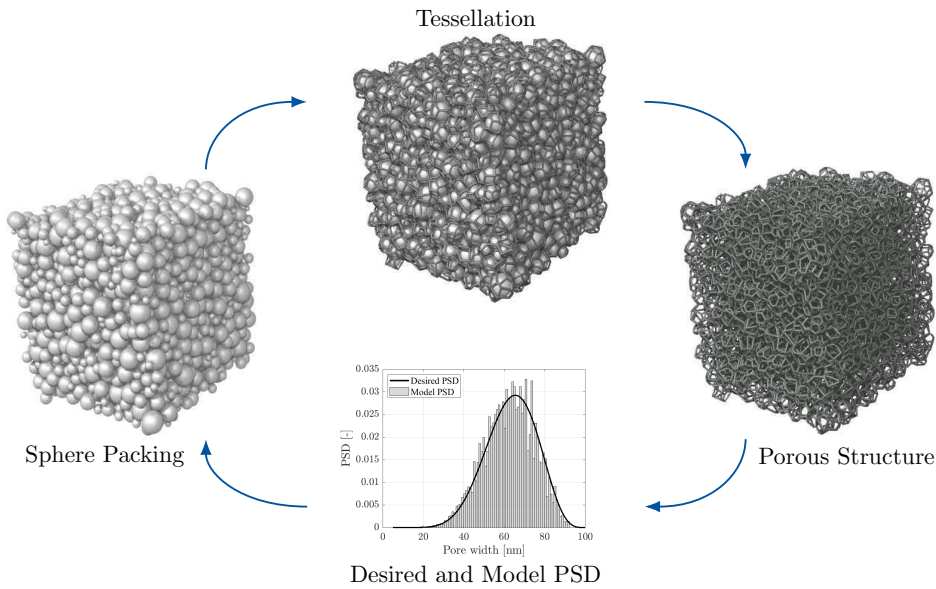


Fig. 7.13: Generation of 3D open-porous cellular-like microstructures using Laguerre-Voronoi tessellation, based on the random close packing of polydisperse spheres. The resulting structures are adjusted to match an desired experimental pore-size distribution, based on [171].

7.2.2 FE-Results and Data Set Analysis

The modeled aerogels were subjected to uniaxial compression testing utilizing the finite element package LS-DYNA, with the objective of studying their macroscopic mechanical behavior under periodic boundary conditions. The Young's modulus was assigned a value of 4.5 GPa for the beam elements, with

fiber diameters evaluated theoretically based on data obtained from the experiments. Figure 7.14 depicts three distinct exemplary PSDs and the respective contributions of pore widths in a box plot, accompanied by the accumulated PSD and the stress-strain response of the RVEs. The PSD can be described by a mean value, denoted by μ_d , and a standard deviation, denoted by σ_d . For the purpose of further analysis, it is also useful to define a single variable, known as the coefficient of variation, which is given by the expression $c_v = \mu_d/\sigma_d$. A total of 144 simulations were conducted for three solid fractions ϕ (1.00 %, 2.50 %, and 5.00 %) with different c_v values. In this example the experimental PSDs have a mean value given with $\mu_d = 47.50 \pm 2.50$ nm with a cell wall diameter of 4.50 ± 0.05 nm. The RVE size for all three structures was determined with 400.00 ± 10.00 nm, see Figure 7.14(a). These values were obtained for varying standard deviations of $\sigma_d = 6.00, 8.00$ and 15.00 nm [170]. As illustrated in Figure 7.14(c), the plateau regime is observed to be smaller in instances where a larger standard deviation of the PSD is employed. This is due to the fact that a larger standard deviation also gives rise to the existence of larger cells within the structure, which in turn contribute to a larger proportion of the total volume fraction. These contributions are apparent in the cumulative PSD, as illustrated in Figure 7.14(b). In the case of smaller cells, densification occurs at an earlier stage, resulting in a stiffer response.

A scaling relationship between the structural parameters of the solid fraction ϕ and the Young's modulus E was identified. The scaling exponent obtained was $m = 1.82$, as illustrated in Figure 7.15. This finding is in close agreement with the results obtained from open-cell foam models and experimental values. Moreover, the mechanical anisotropy of the aerogel RVE was investigated through uniaxial compression in three orthogonal directions. The results of this study indicate that the observed behavior was consistent across all directions.

The following section will present a strain energy formulation that characterizes the stress-strain response of open-porous cellular-like aerogel microstructures through the volume fraction and the coefficient of variation. These two parameters exhibit a pronounced influence on the mechanical response of the generated microstructures.

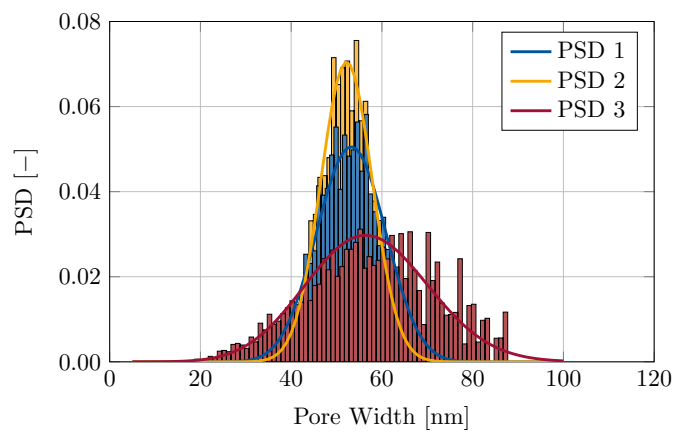
7.2.3 Open-Porous Cellular-Like Aerogel Modeling

To identify a strain energy function, the mechanical responses of all 144 RVEs were employed in order to determine the deformation gradient, as provided in Equation 7.2. In this particular case, the deformation gradient was calculated with a Poisson's ratio of $\nu = 0$. The strain energy function was identified based on input data consisting of the three invariants, I_C , II_C and J , in addition to the volume fraction ϕ and the coefficient of variation c_v . The discovered strain

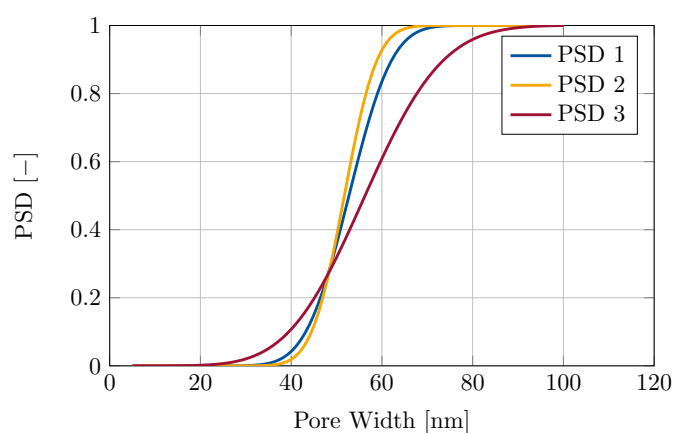
energy function is given by

$$\begin{aligned} \Psi(J, \phi, c_v) = & -0.03\phi^2 \left[0.01 \ln^2(65.52 - 3.37\phi) \right. \\ & \left. + \ln(\exp J + \ln(\ln(c_v))) \ln \left(-2.62 + \frac{3.62}{J} \right)^2 + 1 \right]^{-2}. \end{aligned} \quad (7.9)$$

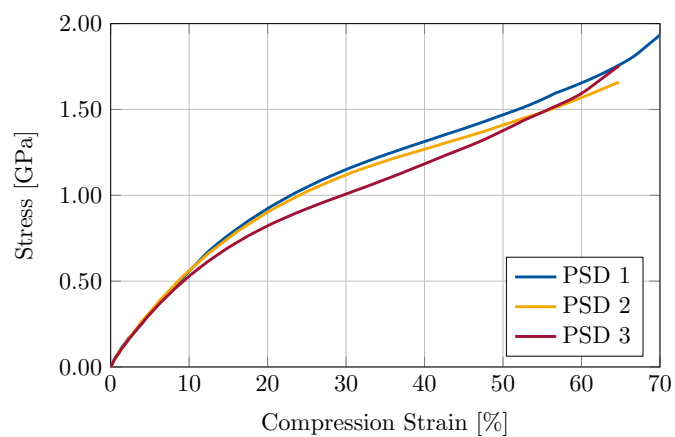
Note that the identified strain energy depends only on the invariant J as well as the volume fraction ϕ and the coefficient of variation c_v . Since the Poisson's ratio is given with $\nu = 0$ in this case, J directly corresponds to the stretch λ . The R^2 score for this model was determined with 97.51 %. Figure 7.16 illustrates the data set utilized in this study, accompanied by the corresponding predictive responses. Figure 7.16(a) illustrates the results of 144 simulations conducted across three volume fractions: 1.00 %, 2.50 %, and 5.00 %. The impact of the normalized coefficient of variation \bar{c}_v on these responses is also highlighted. The data suggest that higher values of \bar{c}_v are associated with increased stiffness in the initial compression phase, followed by a reduction in stiffness at greater compression levels. Moreover, Figure 7.16(b) depicts the strain energy response for each mean value of the coefficient of variation for each volume fraction. It is crucial to acknowledge that the mean response is skewed due to the increasing values of \bar{c}_v , approaching a limited stiffness response. Figure 7.16(c) illustrates the responses for all three volume fractions within a confidence interval defined by the standard deviation of the coefficient of variation $\sigma_{\bar{c}_v}$. It can be observed that a deviation in the response is only influenced in cases where higher volume fractions are involved.



(a)



(b)



(c)

Fig. 7.14: Visualization of (a) three different pore size distributions with varying standard deviations $\sigma_d = 6.00, 8.00$ and 15.00 nm. (b) shows the accumulated pore size distributions and (c) shows the resulting stress-strain responses corresponding to each pore size distribution.

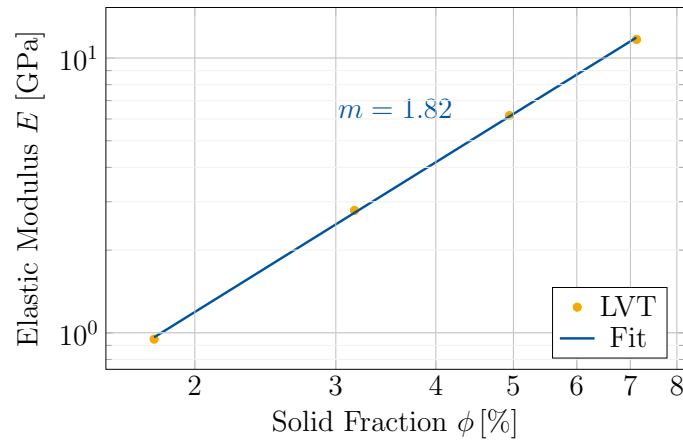
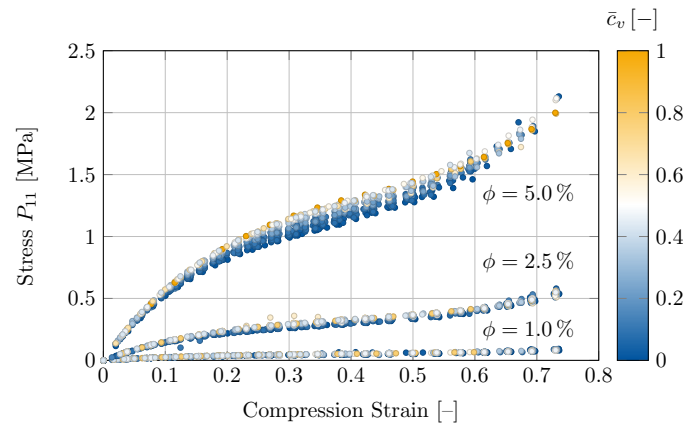
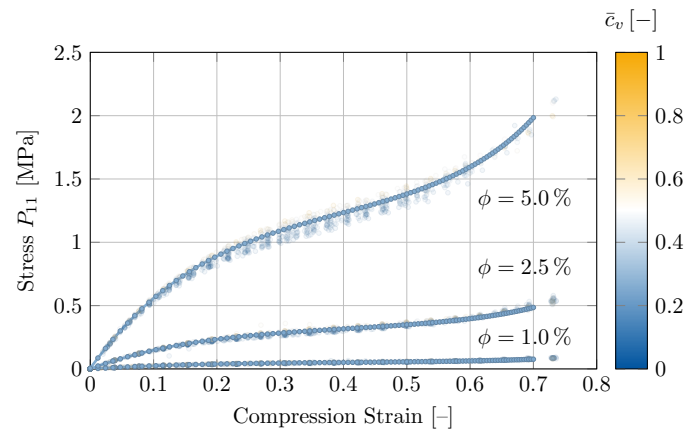


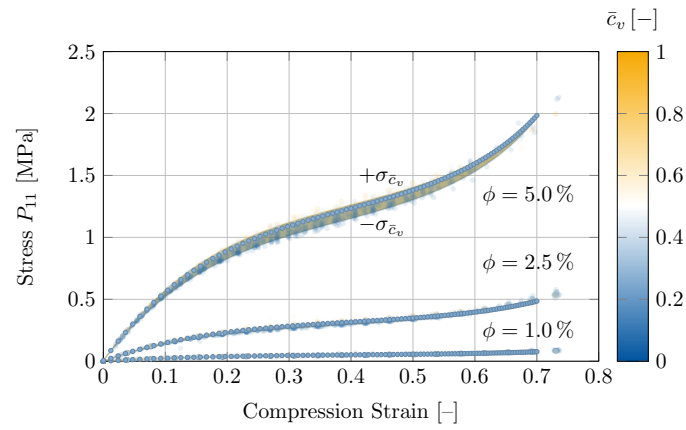
Fig. 7.15: Visualization of elastic modulus E as a function of volume fraction ϕ , with the scaling exponent determined to be $m = 1.82$.



(a)



(b)



(c)

Fig. 7.16: Visualization of (a) provided data set of stress-strain responses for volume fractions of 1.00 %, 2.50 %, and 5.00 %. (b) shows the mean stress-strain response derived from the strain energy function identified in Equation 7.9, along with (c) the stress-strain responses within one standard deviation of the coefficient of variation c_v .

8 Hydration Effects in Polyamide Aerogels

These motions were such as to satisfy me, after frequently repeated observation, that they arose neither from currents in the fluid, nor from its gradual evaporation, but belonged to the particle itself.

R. BROWN

Polyamide aerogels (PAA) are a lightweight porous material with exceptional mechanical properties and superior thermal insulation capabilities. In contrast to conventional silica aerogels, polyamide aerogels integrate the flexibility and conformal characteristics inherent to standard aerogels with augmented durability and strength [172, 173]. The compressive and tensile strengths of these materials are notably higher, offering an improved thermal insulation performance compared to conventional polymer foam insulation, and a relatively straightforward fabrication process. The advantageous properties of polyamide aerogels allow for their use in a variety of applications, including construction and aerospace insulation, as well as consumer electronics [172, 174]. However, one critical aspect that influences their performance is their hygroscopic nature, by which they are capable of rapidly absorbing moisture from the surrounding environment [175]. The hydration level has a significant effect on the mechanical and thermal properties of the material, due to alterations in the interactions between the polymer chains [175, 176]. Prior research has demonstrated that the compressive strength of these materials displays a non-monotonic relationship with water content, resulting from modifications to the hydrogen bond network and disruptions within the polymer architecture [172]. Therefore, it is of paramount importance to gain an understanding of the effects of hydration in order to accurately predict long-term performance and stability.

In the dry state, PAAs are composed of fibers held together by hydrogen bonds between amide groups, as illustrated in Figure 8.1. The initial stage of hydration involves the binding of water molecules to vacant sites within the hydrogen bonding network. This effect appears to reinforce the preexisting hydrogen bond network, thereby resulting in a stiffening effect within the aerogel structure. With advanced hydration, additional water molecules disrupt the original hydrogen bonding network between polyamide chains, thereby altering the structure of the aerogel. This disruption results in an

increase in the segmental motion of polyamide macromolecules. The increased mobility marks the initiation of partial dissolution of the nanosized fibers that constitute the aerogel backbone.

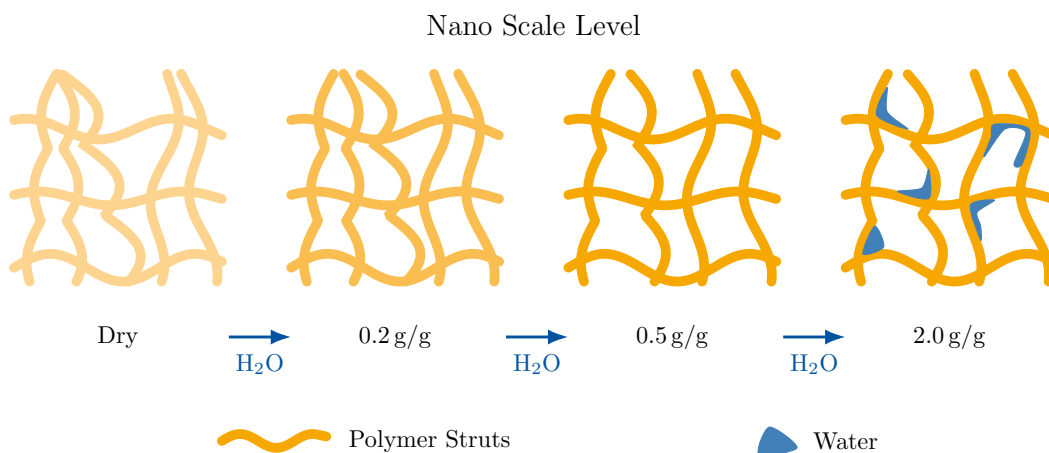


Fig. 8.1: Schematic overview of the evolving microstructure of polyamide (PA) aerogels as hydration levels increase. Initially, there is a strengthening of the existing hydrogen bond network. With further hydration, nanosized fibers begin to dissolve, ultimately leading to the destruction of the aerogel backbone. This process is based on findings from [175].

This chapter introduces a novel approach to quantitatively modeling the effects of hydration on polyamide aerogels through the use of SR. The objective is to identify the impact of varying water content on mechanical properties by incorporating hydration into the constitutive modeling framework. This analysis not only enhances theoretical insights but also serves to improve the practical applications of polyamide aerogels in a variety of fields. Accordingly, a brief introduction to the experimental characterization of the hydration effect is presented in Section 8.1. The hydration-dependent modeling is discussed in detail Section 8.2, where a new strain energy formulation is presented and subjected to critical analysis. The data utilized in this analysis has been previously published in [175].

8.1 Experimental Characterization

Two main techniques were used to achieve controlled hydration. In the initial approach, the water was added directly to the dry aerogel pieces. This method was used to analyze and characterize the structural features. The second hydration method was employed for the mechanical characterization, whereby equilibrium was achieved for PAA monoliths in sealed desiccators with controlled humidity for a period of 84.00 h. The compressive strength of dry and partially hydrated PAA monoliths was determined through the use of

an Instron 4302 universal strength testing machine, employing the humid air exposure method. During the course of the experiments, cylindrical monoliths with a length of 28.00 ± 3.00 mm and a diameter of 20.00 ± 2.00 mm were analyzed. Each measurement was repeated using at least three individual monoliths from different batches, independently conditioned. The averaged, smoothed stress-strain responses for the hydration levels of 0.00 %, 30.00 %, 45.00 %, 50.00 %, 70.00 % and 85.00 % are illustrated in Figure 8.2. The present

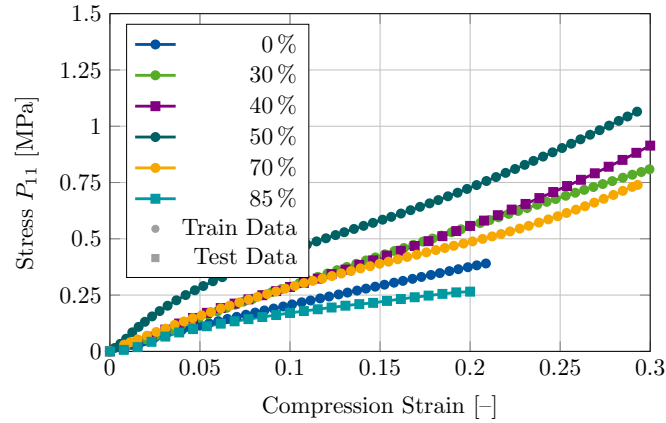


Fig. 8.2: Visualization of the averaged and smoothed stress-strain responses of polyamide aerogel monoliths subjected to compression strain. The hydration rates of 0.00 %, 30.00 %, 50.00 %, and 70.00 % are used as a training set, while the hydration rates of 40.00 % and 85.00 % serve as a test set.

investigation will leverage four discrete levels of hydration for training and the identification of a strain energy function. The remaining two hydration levels will be employed as a test data set. To assess the interpolation and extrapolation capabilities, the test set includes hydration levels of 40.00 % and 85.00 %.

Low-voltage scanning electron microscopy (LV-SEM) images of the pristine polyamide aerogel were obtained using a ThermoFisher Scientific Scios 2 device. The PAA samples were attached to vacuum-resistant carbon tapes without any additional coating for imaging purposes. The LV-SEM images demonstrate the existence of a 3D network composed of interconnected nanofibers with diameters within the range of 20.00 nm to 50.00 nm. The PAA exhibits a highly porous structure, with pores that are typically within the mesoporous range of 2.00 nm to 50.00 nm. The fibers display extensive interconnectivity, forming a complex 3D architecture with relatively smooth surface textures. The structure is observed to be uniform throughout the imaged areas, indicating consistent synthesis and drying processes without significant fiber aggregation or collapse.

8.2 Hydration Effect Modeling

In order to identify the strain and energy function for PA aerogels, it is necessary to define the deformation gradient, which is influenced by both the stretches and Poisson's ratio, as demonstrated in Equation 7.2. Currently, the existing literature lacks precise data concerning the Poisson's ratio for PA aerogel. Therefore, additional research is required to determine this crucial material parameter. Nevertheless, the Poisson ratio within the elastic region has been documented for polyurethane aerogels to be $\nu = 0.2$. Accordingly, this value will be employed as a point of reference for the forthcoming analysis. Based on the presented stress stain data, a strain energy formulation dependent on the degree of hydration was identified, given by

$$\bar{\Psi}(I_{\bar{C}}, II_{\bar{C}}, \kappa) = \left(5.05 \sin(-I_{\bar{C}} + \kappa + 0.16) \right) \left(\sqrt{I_{\bar{C}}} + 3I_{\bar{C}} + II_{\bar{C}} + \frac{18.94}{II_{\bar{C}}} \sqrt{2I_{\bar{C}} + II_{\bar{C}}} \sin(3.90\kappa) \sin[(2.40 - \kappa) \ln II_{\bar{C}} - I_{\bar{C}} + 0.31] \right)^{-1}. \quad (8.1)$$

The value of κ represents the degree of hydration and is defined within the range of 0 to 1. It should be noted that the identified formulation is highly nonlinear. A sinusoidal function was selected as it corresponds to the observation that the stiffness response is greatest for a hydration level of 50.00 %. The overall R^2 score for this strain energy with respect to the training data was determined to be 96.00 %. The stress-strain response of the strain energy formulation is illustrated in Figure 8.3. The identified formulation provides an accurate

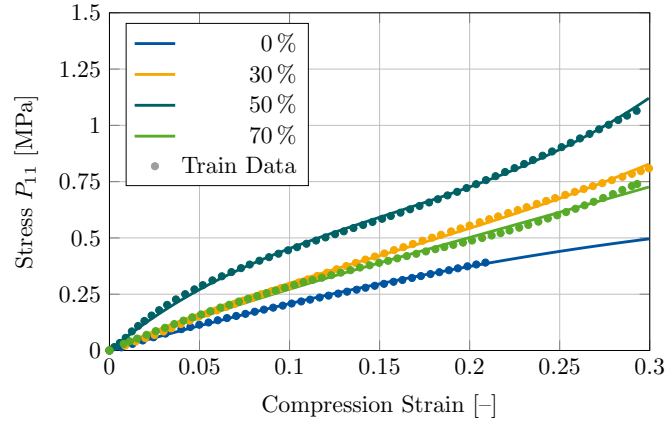


Fig. 8.3: Stress-strain responses of polyamide aerogels at varying levels of hydration, alongside the corresponding training data. The responses are derived from the strain energy function described in Equation 8.1.

representation of the underlying data. Nevertheless, it is unclear how effectively the strain energy function will perform when applied to data that has not been previously observed. To assess this, two supplementary curves representing

the hydration values of 40.00 % and 85.00 % can be employed. The stress-strain responses for these hydration levels are illustrated in Figure 8.4. A detailed analysis of the responses reveals that, although the strain energy function accurately reflects the general trend, it does not fully capture the stress-strain response for the test data. A number of factors may be responsible

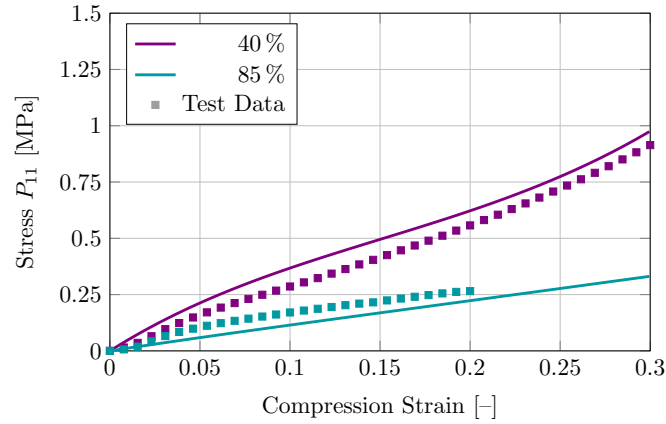


Fig. 8.4: Stress-strain responses of polyamide aerogels at varying levels of hydration, alongside the corresponding test data. The responses are derived from the strain energy function described in Equation 8.1.

for this underperformance. An examination of Young’s modulus across varying degrees of hydration reveals considerable inconsistencies in the data obtained, which can be attributed to uncertainties associated with the synthesis and measurement processes [175]. These inconsistencies consequently have an indirect impact on the framework’s predictive capabilities, as they are not incorporated into the analysis. Moreover, the modeling approach was based on a number of assumptions, including the assumption of a Poisson ratio of $\nu = 0.2$. Additionally, there is a possibility that the identified strain energy function overfits the existing data.

In conclusion, although the existing model offers a satisfactory representation of the stiffening trend in the stress response, its precision is limited. To gain further insight into the phenomenon of hydration and to develop a more accurate model, it is necessary to obtain a more comprehensive data set.

9 Conclusion

What is the good of drawing conclusions from experience? I don't deny we sometimes draw the right conclusions, but don't we just as often draw the wrong ones?

G. C. LICHTENBERG

In conclusion, this investigation has demonstrated the potential of symbolic regression for advancing material modeling through the discovery of novel constitutive material laws. In particular, the framework of deep symbolic regression in combination with continuum mechanical theory has shown great potential for the successful discovery of novel and interpretable formulations that accurately characterize complex material behaviors. This study presents a comprehensive analysis and evaluation of the performance of the framework for both artificial and experimental data sets. A novel model has been proposed for vulcanized rubber and temperature-dependent thermoplastic elastomers. The findings demonstrate the efficacy of symbolic regression in addressing challenges associated with sparse data conditions. Moreover, a methodology was proposed for incorporating additional nonlinear effects, such as the Mullins effect, into the modeling process. The modeling of aerogels offers a promising domain for future research, as this class of materials displays distinctive mechanical and thermal properties resulting from their intricate microstructures. This work presented a novel approach for identifying microstructure-based constitutive formulations for silica aerogels and κ -carrageenan aerogels. Moreover, the work put forth a novel strategy for comprehending hydration effects in polyamide aerogels. Further investigation in this field can facilitate a more comprehensive understanding of the interrelationships between microstructural and macroscopic properties, thereby enhancing the practical utility of aerogels in a range of industrial applications.

It is anticipated that symbolic regression will prove a valuable tool for further investigation in the field of material modeling, particularly for the development of predictive models applicable to a broader range of materials and conditions, as well as for the incorporation of uncertainties. The framework can be straightforwardly extended to accommodate anisotropic effects and the identification of viscoelastic material models. Moreover, the methodology may be extended to yield polyconvex formulations. The capacity to generate interpretable models suggests promising applications in the optimization of material design and the determination of the influence of microstructure on

macroscopic properties. This approach can be further extended for the discovery of surrogate models of RVEs, which can provide valuable insights into homogenization techniques such as FE². Further research could concentrate on improving the dependability of these methodologies across a range of data sets and extending their applicability to other complex materials, thereby making a significant contribution to the field of materials science.

Moreover, the framework of deep symbolic regression presents a promising avenue for further expansion and development. In particular, investigations into effective strategies for hyperparameter tuning could yield significant advancements in the field of material modeling. Furthermore, the methodology can be expanded to include the formulation of heuristic rules that could be integrated as priors within the model, which has not been explored in this analysis. Additionally, the approach could be enhanced by incorporating tensorial relationships between stress and strain tensors, which may facilitate a more profound understanding of material behavior. Despite these promising directions for future research, this work concludes here, acknowledging that there is still a significant amount of work to be done in advancing this field.

List of Figures

1.1	Classification of Constitutive Modeling Approaches	2
1.2	Novel Constitutive Artificial Neural Network Architecture . . .	9
2.1	Iterative Expression Evolution	12
2.2	Expression Tree and Traversal Example	14
2.3	Crossover Mutation	16
2.4	Subtree Mutation	17
2.5	Point Mutation	18
2.6	Hoist Mutation	19
2.7	Deep Symbolic Regression Process	23
3.1	Symbolic Regression Procedure for Novel Model Discovery . . .	29
4.1	Fitness Evolution of Generalized Mooney-Rivlin Model Using gplearn	35
4.2	Stress-Strain Responses for Incompressible Generalized Mooney- Rivlin Model Using gplearn	36
4.3	Stress-Strain Responses for Incompressible Generalized Mooney- Rivlin Model Using DSO	39
4.4	Stress-Strain Responses for Nearly Incompressible Generalized Mooney-Rivlin Model Using DSO	41
4.5	70.00 % to 30.00 % Train-Test Split Influence for Incompressible Generalized Mooney-Rivlin Model	44
4.6	60.00 % to 40.00 % Train-Test Split Influence for Incompressible Generalized Mooney-Rivlin Model	45
4.7	Stress-Strain Response for Stretch-Based Ogden Model Using DSO	46
5.1	Best Fit for Treloar Data Using Mooney-Rivlin Model	49
5.2	Best Fit for Treloar Data of Novel Model Discovered Using DSO	49
5.3	Contributions of Terms in Strain Energy for Strains up to 700.00 % for Treloar Data	54
5.4	Contributions of Terms in Strain Energy for Strains up to 300.00 % for Treloar Data	55
5.5	Stress-Strain Responses of Novel Models Under Different Noise Levels for Treloar Data	56
5.6	Stress-Strain Responses of Extended Tube and Non-Hyperelastic Shariff Model for Treloar Data	57

5.7	Best Fit for Treloar Data Using Stretch-Based Ogden Model	58
5.8	Best Fit for Treloar Data Using Novel Stretch-Based Model Discovered Using DSO	59
5.9	Stress-Strain Responses for Kawabata Data Set Fitted Using P_{11} of UT, PS and EBT	62
5.10	Stress-Strain Responses for Kawabata Data Set Fitted Using P_{11} Data	63
5.11	Stress-Strain Responses for Kawabata Data Set Fitted Using P_{11} and P_{22} Data	64
5.12	Temperature-Dependent Stress-Strain Responses for Thermo- plastic Polyester Elastomer Hytrel 4556	67
5.13	Material Constants as a Function of Temperature for Thermo- plastic Polyester Elastomer Hytrel 4556	68
5.14	Contributions of Temperature-Dependent Terms in Strain Energy	70
6.1	Schematic Stress-Strain Response with Mullins Effect and Per- manent Set	72
6.2	Two-Step Procedure for Modeling the Mullins Effect	74
6.3	Stress-Strain Responses for Ogden-Roxburgh Model Using DSO	77
6.4	70.00 % to 30.00 % Train-Test Split Influence for Ogden- Roxburgh Model	78
6.5	60.00 % to 40.00 % Train-Test Split Influence for Ogden- Roxburgh Model	79
6.6	Cyclic Stress-Strain Responses of Filled Silicone at -40.00°C , -20.00°C and 20.00°C	82
6.7	Cyclic Stress-Strain Responses of Filled Silicone at 60.00°C , 100.00°C and 150.00°C	83
6.8	Extrapolation Assessment for Cyclic Stress-Strain Responses of Filled Silicone at -40.00°C , -20.00°C and 20.00°C	85
6.9	Extrapolation Assessment for Cyclic Stress-Strain Responses of Filled Silicone at 60.00°C , 100.00°C and 150.00°C	86
7.1	Silica, Marshmallow and Corn Starch Aerogel Samples	88
7.2	Conventional Aerogel Synthesis Process	89
7.3	Classification of Aerogels	90
7.4	κ -Carrageenan and Silica Aerogel Microstructures	91
7.5	RVE-Based Microstructural Aerogel Modeling Using SR	92
7.6	DLCA Algorithm	95
7.7	Aggregated Structures at Different Concentrations	97
7.8	FE Compression Test of Four Aggregated Structures at Different Concentrations	99
7.9	Stress-Strain Responses of Four Aggregated Structures at Dif- ferent Concentrations	100

7.10	Elastic Modulus as a Function of Concentration and Gelation Kinetics at Different Concentrations	102
7.11	Boxplot of Elastic Modulus, Fractal Dimension, and Correlation Matrix for DLCA Inputs and Target Outputs	104
7.12	Concentration-Dependent Stress-Strain Responses for Silica Aerogel Based Microstructures	105
7.13	Generation of 3D Open-Porous Cellular-Like Microstructures .	106
7.14	Analysis of Pore Size Distributions and Resulting Stress-Strain Responses	109
7.15	Elastic Modulus as a Function of Volume Fraction	110
7.16	Stress-Strain Responses for Different Volume Fractions and Varying Coefficient of Variation	111
8.1	Effect of Hydration on Polyamide Aerogel Microstructure . . .	114
8.2	Hydration-Dependent Stress-Stress Responses of Polyamide Aerogel Monoliths	115
8.3	PAA Stress-Strain Responses for Training Data Set	116
8.4	PAA Stress-Strain Responses for Test Data Set	117
B.1	Mapping Between Reference and Current Configuration	vii
B.2	Cutting Face Through Body for Definition of Cauchy Vector .	ix

Bibliography

- [1] Abdusalamov, Rasul, Weise, Jendrik, and Itskov, Mikhail. “Rediscovering the Mullins effect with deep symbolic regression”. In: *International Journal of Plasticity* 179 (2024), p. 104037.
 - [2] Pandit, Prakul, Abdusalamov, Rasul, Itskov, Mikhail, and Rege, Ameya. “Deep reinforcement learning for microstructural optimisation of silica aerogels”. In: *Scientific Reports* 14.1 (2024), p. 1511.
 - [3] Abdusalamov, Rasul, Kaplunov, Julius, and Itskov, Mikhail. “Discovering asymptotic expansions for problems in mechanics using symbolic regression”. In: *Mechanics Research Communications* 133 (2023), p. 104197.
 - [4] Abdusalamov, Rasul, Hillgärtner, Markus, and Itskov, Mikhail. “Automatic generation of interpretable hyperelastic material models by symbolic regression”. In: *International Journal for Numerical Methods in Engineering* 124.9 (2023), pp. 2093–2104.
 - [5] Abdusalamov, Rasul, Scherdel, Christian, Itskov, Mikhail, Milow, Barbara, Reichenauer, Gudrun, and Rege, Ameya. “Modeling and Simulation of the Aggregation and the Structural and Mechanical Properties of Silica Aerogels”. In: *The Journal of Physical Chemistry B* 125.7 (2021), pp. 1944–1950.
 - [6] Abdusalamov, Rasul, Pandit, Prakul, Milow, Barbara, Itskov, Mikhail, and Rege, Ameya. “Machine learning-based structure–property predictions in silica aerogels”. In: *Soft Matter* 17 (2021), pp. 7350–7358.
 - [7] Xiong, Weibo, Abdusalamov, Rasul, and Itskov, Mikhail. “Mesoscopic structure modeling of silica aerogels using cluster-cluster aggregation”. In: *PAMM* (2024).
 - [8] Xiong, Weibo, Abdusalamov, Rasul, Itskov, Mikhail, Milow, Barbara, and Rege, Ameya. “Analysis of the microstructural connectivity and compressive behavior of particle aggregated silica aerogels”. In: *PAMM* (2024).
 - [9] Abdusalamov, Rasul, Itskov, Mikhail, Kaplunov, Julius, and Prikazchikov, Danila. “Adjustment of micro-structure parameters of aggregated structures for dynamic modeling of silica aerogels”.
-

- In: *Mechanics of High-Contrast Elastic Solids: Contributions from Euromech Colloquium 626*. Springer, 2023.
- [10] Pandit, Prakul, Abdusalamov, Rasul, Itskov, Mikhail, Milow, Barbara, and Rege, Ameya. “Data-driven inverse design and optimisation of silica aerogel model networks”. In: *PAMM* 23.1 (2023).
 - [11] Abdusalamov, Rasul, Hillgärtner, Markus, and Itskov, Mikhail. “Hyper-elastic material modelling using symbolic regression”. In: *PAMM* 22.1 (2023).
 - [12] Abdusalamov, Rasul, Pandit, Prakul, Itskov, Mikhail, Milow, Barbara, and Rege, Ameya. “Predictive modeling and simulation of silica aerogels by using aggregation algorithms”. In: *PAMM* 21.1 (2021).
 - [13] Abdusalamov, Rasul, Itskov, Mikhail, Milow, Barbara, and Rege, Ameya. “Analysis of the fractal properties of silica aerogels using diffusion-limited aggregation”. In: *PAMM* 20.1 (2021).
 - [14] Fuhg, Jan Niklas *et al.* *A review on data-driven constitutive laws for solids*. 2024. arXiv: 2405.03658.
 - [15] Kirchdoerfer, T. and Ortiz, M. “Data-driven computational mechanics”. In: *Computer Methods in Applied Mechanics and Engineering* 304 (2016), pp. 81–101.
 - [16] Shen, Y., Chandrashekhara, K., Breig, W. F., and Oliver, L. R. “Neural Network Based Constitutive Model for Rubber Material”. In: *Rubber Chemistry and Technology* 77.2 (2004), pp. 257–277.
 - [17] Gerwin, Donald. “Information processing, data inferences, and scientific generalization”. In: *Behavioral Science* 19.5 (1974), pp. 314–325.
 - [18] Santosa, Fadil and Symes, William W. “Linear Inversion of Band-Limited Reflection Seismograms”. In: *SIAM Journal on Scientific and Statistical Computing* 7.4 (1986), pp. 1307–1330.
 - [19] Wang, Kun and Sun, WaiChing. “Meta-modeling game for deriving theoretical-consistent, micro-structural-based traction-separation laws via deep reinforcement learning”. In: *arXiv preprint arXiv:1810.10535* (2018).
 - [20] Kaelbling, Leslie Pack, Littman, Michael L, and Moore, Andrew W. “Reinforcement learning: A survey”. In: *Journal of artificial intelligence research* 4 (1996), pp. 237–285.
 - [21] Lemaitre, Jean and Chaboche, Jean-Louis. *Mechanics of solid materials*. Cambridge university press, 1994.
 - [22] Mooney, M. “A Theory of Large Elastic Deformation”. In: *Journal of Applied Physics* 11.9 (1940), pp. 582–592.

- [23] Arruda, Ellen M. and Boyce, Mary C. “A three-dimensional constitutive model for the large stretch behavior of rubber elastic materials”. In: *Journal of the Mechanics and Physics of Solids* 41.2 (1993), pp. 389–412.
- [24] Kaliske, M and Heinrich, G. “An extended tube-model for rubber elasticity: statistical-mechanical theory and finite element implementation”. In: *Rubber Chemistry and Technology* 72.4 (1999), pp. 602–632.
- [25] Khiêm, Vu Ngoc and Itskov, Mikhail. “Analytical network-averaging of the tube model:: Rubber elasticity”. In: *Journal of the Mechanics and Physics of Solids* 95 (2016), pp. 254–269.
- [26] Eggersmann, Robert, Kirchdoerfer, Trenton, Reese, Stefanie, Stainier, Laurent, and Ortiz, Michael. “Model-free data-driven inelasticity”. In: *Computer Methods in Applied Mechanics and Engineering* 350 (2019), pp. 81–99.
- [27] Carrara, Pietro, De Lorenzis, Laura, Stainier, Laurent, and Ortiz, Michael. “Data-driven fracture mechanics”. In: *Computer Methods in Applied Mechanics and Engineering* 372 (2020), p. 113390.
- [28] Karapiperis, Konstantinos, Stainier, Laurent, Ortiz, Michael, and Andrade, José E. “Data-driven multiscale modeling in mechanics”. In: *Journal of the Mechanics and Physics of Solids* 147 (2021), p. 104239.
- [29] Chinesta, Francisco, Ladeveze, Pierre, Ibanez, Ruben, Aguado, Jose Vicente, Abisset-Chavanne, Emmanuelle, and Cueto, Elias. “Data-driven computational plasticity”. In: *Procedia engineering* 207 (2017), pp. 209–214.
- [30] Fuchs, Alexander, Heider, Yousef, Wang, Kun, Sun, WaiChing, and Kaliske, Michael. “DNN2: A hyper-parameter reinforcement learning game for self-design of neural network based elasto-plastic constitutive descriptions”. In: *Computers and Structures* 249 (2021), p. 106505.
- [31] Wang, Kun and Sun, WaiChing. “Meta-modeling game for deriving theory-consistent, microstructure-based traction–separation laws via deep reinforcement learning”. In: *Computer Methods in Applied Mechanics and Engineering* 346 (2019), pp. 216–241.
- [32] Liu, Minliang, Liang, Liang, Dong, Hai, Sun, Wei, and Gleason, Rudolph L. “Constructing growth evolution laws of arteries via reinforcement learning”. In: *Journal of the Mechanics and Physics of Solids* 168 (2022), p. 105044.
- [33] Linka, Kevin, Hillgärtner, Markus, Abdolazizi, Kian P., Aydin, Roland C., Itskov, Mikhail, and Cyron, Christian J. “Constitutive artificial neural networks: A fast and general approach to predictive data-driven constitutive modeling by deep learning”. In: *Journal of Computational Physics* 429 (2021), p. 110010.

- [34] Klein, Dominik K., Fernández, Mauricio, Martin, Robert J., Neff, Patrizio, and Weeger, Oliver. “Polyconvex anisotropic hyperelasticity with neural networks”. In: *Journal of the Mechanics and Physics of Solids* 159 (2022), p. 104703.
- [35] Bahmani, Bahador and Sun, WaiChing. “Physics-constrained symbolic model discovery for polyconvex incompressible hyperelastic materials”. In: *arXiv preprint arXiv:2310.04286* (2023).
- [36] Fuhg, Jan N. and Bouklas, Nikolaos. “On physics-informed data-driven isotropic and anisotropic constitutive models through probabilistic machine learning and space-filling sampling”. In: *Computer Methods in Applied Mechanics and Engineering* 394 (2022), p. 114915.
- [37] Ghaderi, Aref, Morovati, Vahid, and Dargazany, Roozbeh. “A Physics-Informed Assembly of Feed-Forward Neural Network Engines to Predict Inelasticity in Cross-Linked Polymers”. In: *Polymers* 12.11 (2020).
- [38] Klein, Dominik K, Ortigosa, Rogelio, Martínez-Frutos, Jesús, and Weeger, Oliver. “Nonlinear electro-elastic finite element analysis with neural network constitutive models”. In: *Computer Methods in Applied Mechanics and Engineering* 425 (2024), p. 116910.
- [39] Fuhg, Jan Niklas, Jones, Reese Edward, and Bouklas, Nikolaos. “Extreme sparsification of physics-augmented neural networks for interpretable model discovery in mechanics”. In: *Computer Methods in Applied Mechanics and Engineering* 426 (2024), p. 116973.
- [40] Linka, Kevin and Kuhl, Ellen. “A new family of Constitutive Artificial Neural Networks towards automated model discovery”. In: *Computer Methods in Applied Mechanics and Engineering* 403 (2023), p. 115731.
- [41] Flaschel, Moritz, Kumar, Siddhant, and De Lorenzis, Laura. “Unsupervised discovery of interpretable hyperelastic constitutive laws”. In: *Computer Methods in Applied Mechanics and Engineering* 381 (2021), p. 113852.
- [42] Thakolkaran, Prakash, Joshi, Akshay, Zheng, Yiwen, Flaschel, Moritz, De Lorenzis, Laura, and Kumar, Siddhant. “NN-EUCLID: Deep-learning hyperelasticity without stress data”. In: *Journal of the Mechanics and Physics of Solids* 169 (2022), p. 105076.
- [43] Kissas, Georgios, Mishra, Siddhartha, Chatzi, Eleni, and De Lorenzis, Laura. “The language of hyperelastic materials”. In: *Computer Methods in Applied Mechanics and Engineering* 428 (2024), p. 117053.
- [44] Xu, Haotian, Flaschel, Moritz, and De Lorenzis, Laura. “Discovering non-associated pressure-sensitive plasticity models with EUCLID”. In: (2024).

- [45] Langley, Pat. “Data-driven discovery of physical laws”. In: *Cognitive Science* 5.1 (1981), pp. 31–54.
- [46] Falkenhainer, Brian C and Michalski, Ryszard S. “Integrating quantitative and qualitative discovery: the ABACUS system”. In: *Machine Learning* 1 (1986), pp. 367–401.
- [47] Koza, John R *et al.* “Hierarchical genetic algorithms operating on populations of computer programs.” In: *IJCAI*. Vol. 89. 1989, pp. 768–774.
- [48] Koza, John R. “Genetic programming as a means for programming computers by natural selection”. In: *Statistics and computing* 4 (1994), pp. 87–112.
- [49] Koza, John R. “Genetic Programming, Version 2”. In: *Encyclopedia of Computer Science and Technology* 1989 (1997), pp. 1–26.
- [50] De Jong, Kenneth Alan. *An analysis of the behavior of a class of genetic adaptive systems*. University of Michigan, 1975.
- [51] Brindle, Anne. “Genetic algorithms for function optimization”. In: (1980).
- [52] Goldberg, Daniel E. “Genetic Algorithms in Search”. In: 1989.
- [53] Makke, Nour and Chawla, Sanjay. “Interpretable scientific discovery with symbolic regression: a review”. In: *Artificial Intelligence Review* 57.1 (2024), p. 2.
- [54] Stephens, Trevor *et al.* “Genetic Programming in Python, with a scikit-learn inspired API: gplearn”. In: *Documentation at <https://gplearn.readthedocs.io/en/stable/>* (2016).
- [55] Petersen, Brenden K, Landajuela, Mikel, Mundhenk, T Nathan, Santiago, Claudio P, Kim, Soo K, and Kim, Joanne T. “Deep symbolic regression: Recovering mathematical expressions from data via risk-seeking policy gradients”. In: *arXiv preprint arXiv:1912.04871* (2019).
- [56] Udrescu, Silviu-Marian and Tegmark, Max. “AI Feynman: A physics-inspired method for symbolic regression”. In: *Science Advances* 6.16 (2020), eaay2631.
- [57] La Cava, William *et al.* “Contemporary symbolic regression methods and their relative performance”. In: *arXiv preprint arXiv:2107.14351* (2021).
- [58] Wang, Yiqun, Wagner, Nicholas, and Rondinelli, James M. “Symbolic regression in materials science”. In: *MRS Communications* 9.3 (2019), pp. 793–805.

- [59] Augusto, D.A. and Barbosa, H.J.C. “Symbolic regression via genetic programming”. In: *Proceedings. Vol.1. Sixth Brazilian Symposium on Neural Networks*. 2000, pp. 173–178.
- [60] Poli, Riccardo, Langdon, William B., and McPhee, Nicholas Freitag. *A field guide to genetic programming*. With contributions by J. R. Koza. Published via <http://lulu.com> and freely available at <http://www.gp-field-guide.org.uk>, 2008.
- [61] Affenzeller, Michael, Winkler, Stephan, Wagner, Stefan, and Beham, Andreas. *Genetic algorithms and genetic programming: modern concepts and practical applications*. Taylor & Francis, 2009.
- [62] Petersen, Brenden K., Landajuela, Mikel, Mundhenk, T. Nathan, Santiago, Claudio P., Kim, Soo K., and Kim, Joanne T. *Deep symbolic regression: Recovering mathematical expressions from data via risk-seeking policy gradients*. 2021.
- [63] Truesdell, Clifford and Noll, Walter. *The Non-Linear Field Theories of Mechanics*. Third. Springer, 2004.
- [64] Müller, Ingo. *Grundzüge der Thermodynamik: mit historischen Anmerkungen*. Springer-Verlag, 2013.
- [65] Holzapfel, Gerhard A. *Nonlinear solid mechanics: a continuum approach for engineering science*. 2002.
- [66] Liu, I-Shih *et al.* *Continuum mechanics*. Vol. 5. Springer, 2002.
- [67] Bertram, Albrecht. *Elasticity and plasticity of large deformations*. Springer, 2012.
- [68] Haupt, Peter. *Continuum mechanics and theory of materials*. Springer Science & Business Media, 2013.
- [69] Itskov, M. *Tensor Algebra and Tensor Analysis for Engineers: With Applications to Continuum Mechanics*. Mathematical Engineering. Springer International Publishing, 2018.
- [70] Richter, H. “Das isotrope Elastizitätsgesetz”. In: *ZAMM-Journal of Applied Mathematics and Mechanics/Zeitschrift für Angewandte Mathematik und Mechanik* 28.7-8 (1948), pp. 205–209.
- [71] Hartmann, Stefan and Neff, Patrizio. “Polyconvexity of generalized polynomial-type hyperelastic strain energy functions for near-incompressibility”. In: *International Journal of Solids and Structures* 40.11 (2003), pp. 2767–2791.
- [72] Miehe, C. “Aspects of the formulation and finite element implementation of large strain isotropic elasticity”. In: *International Journal for Numerical Methods in Engineering* 37.12 (1994), pp. 1981–2004.

- [73] Bower, Allan F. *Applied Mechanics of Solids*. CRC Press, 2010.
- [74] Ogden, Raymond W, Saccomandi, Giuseppe, and Sgura, Ivonne. “Fitting hyperelastic models to experimental data”. In: *Computational Mechanics* 34 (2004), pp. 484–502.
- [75] Ogden, Raymond William. “Large deformation isotropic elasticity—on the correlation of theory and experiment for incompressible rubberlike solids”. In: *Proceedings of the Royal Society of London. A. Mathematical and Physical Sciences* 326.1567 (1972), pp. 565–584.
- [76] Valanis, KC and Landel, Robert F. “The strain-energy function of a hyperelastic material in terms of the extension ratios”. In: *Journal of Applied Physics* 38.7 (1967), pp. 2997–3002.
- [77] Kawabata, S, Matsuda, M, Tei, K, and Kawai, H. “Experimental survey of the strain energy density function of isoprene rubber vulcanizate”. In: *Macromolecules* 14.1 (1981), pp. 154–162.
- [78] Kauffman, George B. “Charles Goodyear (1800–1860), American Inventor, on the Bicentennial of His Birth”. In: *The Chemical Educator* 6.1 (2001), pp. 50–54.
- [79] Treloar, LR G. “The physics of rubber elasticity”. In: (1975).
- [80] Treloar, Leslie RG. “Stress-strain data for vulcanized rubber under various types of deformation”. In: *Rubber Chemistry and Technology* 17.4 (1944), pp. 813–825.
- [81] Boyce, Mary C and Arruda, Ellen M. “Constitutive models of rubber elasticity: a review”. In: *Rubber chemistry and technology* 73.3 (2000), pp. 504–523.
- [82] Marckmann, Gilles and Verron, Erwan. “Comparison of hyperelastic models for rubber-like materials”. In: *Rubber chemistry and technology* 79.5 (2006), pp. 835–858.
- [83] Steinmann, Paul, Hossain, Mokarram, and Possart, Gunnar. “Hyperelastic models for rubber-like materials: consistent tangent operators and suitability for Treloar’s data”. In: *Archive of Applied Mechanics* 82 (2012), pp. 1183–1217.
- [84] Ricker, Alexander and Wriggers, Peter. “Systematic fitting and comparison of hyperelastic continuum models for elastomers”. In: *Archives of Computational Methods in Engineering* 30.3 (2023), pp. 2257–2288.
- [85] He, Hong, Zhang, Qiang, Zhang, Yaru, Chen, Jianfeng, Zhang, Liquan, and Li, Fanzhu. “A comparative study of 85 hyperelastic constitutive models for both unfilled rubber and highly filled rubber nanocomposite material”. In: *Nano Materials Science* 4.2 (2022), pp. 64–82.

- [86] Rivlin, Ronald S and Saunders, DW0042. “Large elastic deformations of isotropic materials VII. Experiments on the deformation of rubber”. In: *Philosophical Transactions of the Royal Society of London. Series A, Mathematical and Physical Sciences* 243.865 (1951), pp. 251–288.
- [87] Shariff, M. H. B. M. “Strain Energy Function for Filled and Unfilled Rubberlike Material”. In: *Rubber Chemistry and Technology* 73.1 (2000), pp. 1–18.
- [88] Miehe, C., Göktepe, S., and Lulei, F. “A micro-macro approach to rubber-like materials—Part I: the non-affine micro-sphere model of rubber elasticity”. In: *Journal of the Mechanics and Physics of Solids* 52.11 (2004), pp. 2617–2660.
- [89] Chemie Wirtschaftsförderungs-GmbH. *DuPont Engineering Polymers Hytrel 4556*. 2022. URL: <https://www.campusplastics.com/campus/en/datasheet/Hytrel%20AE+4556/DuPont/52/abead118> (visited on 03/29/2022).
- [90] Mullins, L. “Softening of Rubber by Deformation”. In: *Rubber Chemistry and Technology* 42.1 (Mar. 1969), pp. 339–362.
- [91] Itskov, M, Haberstroh, Edmund, Ehret, AE, and Vohringer, MC. “Experimental observation of the deformation induced anisotropy of the Mullins effect in rubber”. In: *KGK-Kautschuk Gummi Kunststoffe* 59.3 (2006), pp. 93–96.
- [92] Laraba-Abbes, Fazilay, Ienny, Patrick, and Piques, Roland. “A new ‘Tailor-made’ methodology for the mechanical behaviour analysis of rubber-like materials: II. Application to the hyperelastic behaviour characterization of a carbon-black filled natural rubber vulcanizate”. In: *Polymer* 44.3 (2003), pp. 821–840.
- [93] Plagge, J. and Klüppel, M. “Mullins effect revisited: Relaxation, recovery and high-strain damage”. In: *Materials Today Communications* 20 (2019), p. 100588.
- [94] Ogden, R. W. and Roxburgh, D. G. “A pseudo-elastic model for the Mullins effect in filled rubber”. In: *Proceedings of the Royal Society of London. Series A: Mathematical, Physical and Engineering Sciences* 455.1988 (1999), pp. 2861–2877.
- [95] Qi, H.J. and Boyce, M.C. “Constitutive model for stretch-induced softening of the stress–stretch behavior of elastomeric materials”. In: *Journal of the Mechanics and Physics of Solids* 52.10 (2004), pp. 2187–2205.
- [96] Dorfmann, A. and Ogden, R.W. “A constitutive model for the Mullins effect with permanent set in particle-reinforced rubber”. In: *International Journal of Solids and Structures* 41.7 (2004), pp. 1855–1878.

- [97] Diani, J., Brieu, M., and Vacherand, J.M. “A damage directional constitutive model for Mullins effect with permanent set and induced anisotropy”. In: *European Journal of Mechanics - A/Solids* 25.3 (2006), pp. 483–496.
- [98] Itskov, Mikhail, Ehret, A, Kazakevičiūtė-Makovska, R, and Weinhold, G. “A thermodynamically consistent phenomenological model of the anisotropic Mullins effect”. In: *ZAMM-Journal of Applied Mathematics and Mechanics/Zeitschrift für Angewandte Mathematik und Mechanik: Applied Mathematics and Mechanics* 90.5 (2010), pp. 370–386.
- [99] Dargazany, Roozbeh and Itskov, Mikhail. “A network evolution model for the anisotropic Mullins effect in carbon black filled rubbers”. In: *International Journal of Solids and Structures* 46.16 (2009), pp. 2967–2977.
- [100] Dargazany, Roozbeh, Khiêm, Vu Ngoc, and Itskov, Mikhail. “A generalized network decomposition model for the quasi-static inelastic behavior of filled elastomers”. In: *International Journal of Plasticity* 63 (2014). Deformation Tensors in Material Modeling in Honor of Prof. Otto T. Bruhns, pp. 94–109.
- [101] Ayoub, G., Zaïri, F., Naït-Abdelaziz, M., Gloaguen, J.M., and Kridli, G. “A visco-hyperelastic damage model for cyclic stress-softening, hysteresis and permanent set in rubber using the network alteration theory”. In: *International Journal of Plasticity* 54 (2014), pp. 19–33.
- [102] Khiêm, Vu Ngoc and Itskov, Mikhail. “An averaging based tube model for deformation induced anisotropic stress softening of filled elastomers”. In: *International Journal of Plasticity* 90 (2017), pp. 96–115.
- [103] Khiêm, Vu Ngoc and Itskov, Mikhail. “Analytical network-averaging of the tube model: Mechanically induced chemiluminescence in elastomers”. In: *International Journal of Plasticity* 102 (2018), pp. 1–15.
- [104] Mohammadi, Hamid and Dargazany, Roozbeh. “A micro-mechanical approach to model thermal induced aging in elastomers”. In: *International Journal of Plasticity* 118 (2019), pp. 1–16.
- [105] Xiao, Rui, Mai, Thanh-Tam, Urayama, Kenji, Gong, Jian Ping, and Qu, Shaoxing. “Micromechanical modeling of the multi-axial deformation behavior in double network hydrogels”. In: *International Journal of Plasticity* 137 (2021), p. 102901.
- [106] Guo, Qiang and Zaïri, Fahmi. “A micromechanics-based model for deformation-induced damage and failure in elastomeric media”. In: *International Journal of Plasticity* 140 (2021), p. 102976.
- [107] Morovati, Vahid, Bahrololoumi, Amir, and Dargazany, Roozbeh. “Fatigue-induced stress-softening in cross-linked multi-network elas-

- tomers: Effect of damage accumulation". In: *International Journal of Plasticity* 142 (2021), p. 102993.
- [108] Saadedine, Mahrez *et al.* "A multiscale model for multiaxial inelastic behavior of elastomeric particulate composites". In: *International Journal of Plasticity* 164 (2023), p. 103594.
- [109] Wang, Bochao, Bustamante, Roger, Kari, Leif, Pang, Haoming, and Gong, Xinglong. "Modelling the influence of magnetic fields to the viscoelastic behaviour of soft magnetorheological elastomers under finite strains". In: *International Journal of Plasticity* 164 (2023), p. 103578.
- [110] Rey, Thierry, Chagnon, G, Le Cam, J-B, and Favier, Denis. "Influence of the temperature on the mechanical behaviour of filled and unfilled silicone rubbers". In: *Polymer Testing* 32.3 (2013), pp. 492–501.
- [111] Kistler, Samuel Stephens. "Coherent expanded aerogels and jellies". In: *Nature* 127.3211 (1931), pp. 741–741.
- [112] Aegerter, Michel A, Leventis, Nicholas, Koebel, Matthias, and Steiner III, Stephen A. *Springer Handbook of Aerogels*. Springer Nature, 2023.
- [113] Danaci, Hacer Mutlu and Akin, Neslihan. "Thermal insulation materials in architecture: a comparative test study with aerogel and rock wool". In: *Environmental Science and Pollution Research* 29.48 (2022), pp. 72979–72990.
- [114] Burchell, Mark J., Graham, Giles, and Kearsley, Anton. "COSMIC DUST COLLECTION IN AEROGEL". In: *Annual Review of Earth and Planetary Sciences* 34.1 (2006), pp. 385–418.
- [115] Mazrouei-Sebdani, Zahra, Begum, Hasina, Schoenwald, Stefan, Horoshenkov, Kirill V., and Malfait, Wim J. "A review on silica aerogel-based materials for acoustic applications". In: *Journal of Non-Crystalline Solids* 562 (2021), p. 120770.
- [116] Hrubesh, Lawrence W. "Aerogel applications". In: *Journal of Non-Crystalline Solids* 225 (1998), pp. 335–342.
- [117] Smirnova, Irina and Gurikov, Pavel. "Aerogel production: Current status, research directions, and future opportunities". In: *The Journal of Supercritical Fluids* 134 (2018), pp. 228–233.
- [118] Zion, Noam, Douglin, John C., Cullen, David A., Zelenay, Piotr, Dekel, Dario R., and Elbaz, Lior. "Porphyrin Aerogel Catalysts for Oxygen Reduction Reaction in Anion-Exchange Membrane Fuel Cells". In: *Advanced Functional Materials* 31.24 (2021), p. 2100963.
- [119] Dorcheh, A Soleimani and Abbasi, MH. "Silica aerogel; synthesis, properties and characterization". In: *Journal of materials processing technology* 199.1-3 (2008), pp. 10–26.

- [120] Woignier, Thierry, Primera, Juan, Alaoui, Adil, Etienne, Pascal, Despestis, Florence, and Calas-Etienne, Sylvie. “Mechanical properties and brittle behavior of silica aerogels”. In: *Gels* 1.2 (2015), pp. 256–275.
- [121] Emmerling, A and Fricke, J. “Scaling properties and structure of aerogels”. In: *Journal of Sol-Gel Science and Technology* 8.1-3 (1997), pp. 781–788.
- [122] Esquivel-Castro, Tzipatly A, Martínez-Luévanos, Antonia, Estrada-Flores, Sofía, and Cano-Salazar, Lucía F. “Porous materials for applications in energy and environment”. In: *Handbook of nanomaterials and nanocomposites for energy and environmental applications*. Springer, 2020, pp. 1–19.
- [123] Soleimani Dorcheh, A. and Abbasi, M.H. “Silica aerogel; synthesis, properties and characterization”. In: *Journal of Materials Processing Technology* 199.1 (2008), pp. 10–26.
- [124] Nita, Loredana Elena, Ghilan, Alina, Rusu, Alina Gabriela, Neamtu, Iordana, and Chiriac, Aurica P. “New trends in bio-based aerogels”. In: *Pharmaceutics* 12.5 (2020), p. 449.
- [125] Alwin, S and Sahaya Shajan, X. “Aerogels: promising nanostructured materials for energy conversion and storage applications”. In: *Materials for renewable and sustainable energy* 9.2 (2020), p. 7.
- [126] Budtova, Tatiana. “Cellulose II aerogels: A review”. In: *Cellulose* 26 (2019), pp. 81–121.
- [127] Lee, Jong-Hoon and Park, Soo-Jin. “Recent advances in preparations and applications of carbon aerogels: A review”. In: *Carbon* 163 (2020), pp. 1–18.
- [128] Abdul Khalil, HPS *et al.* “A review on plant cellulose nanofibre-based aerogels for biomedical applications”. In: *Polymers* 12.8 (2020), p. 1759.
- [129] Ziegler, Christoph, Wolf, André, Liu, Wei, Herrmann, Anne-Kristin, Gaponik, Nikolai, and Eychmüller, Alexander. “Modern inorganic aerogels”. In: *Angewandte Chemie International Edition* 56.43 (2017), pp. 13200–13221.
- [130] Gibson, Lorna J and Ashby, Michael F. *Cellular solids: structure and properties*. Cambridge university press, 1999.
- [131] Groß, J. and Fricke, J. “Scaling of elastic properties in highly porous nanostructured aerogels”. In: *NanoStructured Materials* 6 (1995), pp. 905–908.
- [132] Wong, Joanna CH, Kaymak, Hicret, Brunner, Samuel, and Koebel, Matthias M. “Mechanical properties of monolithic silica aerogels made

- from polyethoxydisiloxanes”. In: *Microporous and mesoporous materials* 183 (2014), pp. 23–29.
- [133] Gross, Joachim, Reichenauer, Gudrun, and Fricke, Jochen. “Mechanical properties of SiO₂ aerogels”. In: *Journal of Physics D: Applied Physics* 21 (1988), pp. 1447–1451.
- [134] Woignier, T and Phalippou, J. “Scaling law variation of the mechanical properties of silica aerogels”. In: *Le Journal de Physique Colloques* 50.C4 (1989), pp. C4–179.
- [135] Hrubesh, Lawrence W. “Aerogel applications”. In: *Journal of Non-Crystalline Solids* 225 (1998), pp. 335–342.
- [136] Smirnova, I, Suttiruengwong, S, and Arlt, W. “Feasibility study of hydrophilic and hydrophobic silica aerogels as drug delivery systems”. In: *Journal of Non-Crystalline Solids* 350 (2004), pp. 54–60.
- [137] Gross, J., Fricke, J., Pekala, R. W., and Hrubesh, L. W. “Elastic nonlinearity of aerogels”. In: *Phys Rev B Condens Matter* 45.22 (1992), pp. 12774–12777.
- [138] Gross, J. and Fricke, J. “Ultrasonic velocity measurements in silica, carbon and organic aerogels”. In: *Journal of Non-Crystalline Solids* 145 (1992), pp. 217–222.
- [139] Parmenter, Kelley E. and Milstein, Frederick. “Mechanical properties of silica aerogels”. In: *Journal of Non-Crystalline Solids* 223 (1998), pp. 179–189.
- [140] Maleki, Hajar, Durães, Luisa, and Portugal, António. “An overview on silica aerogels synthesis and different mechanical reinforcing strategies”. In: *Journal of Non-Crystalline Solids* 385 (2014), pp. 55–74.
- [141] Ma, Hang-Shing, Roberts, Anthony P., Prévost, Jean-H., Jullien, Rémi, and Scherer, George W. “Mechanical structure-property relationship of aerogels”. In: *Journal of Non-Crystalline Solids* 277 (2000), pp. 127–141.
- [142] Patil, Sandeep P., Rege, Ameya, Sagardas, Itskov, Mikhail, and Markert, Bernd. “Mechanics of Nanostructured Porous Silica Aerogel Resulting from Molecular Dynamics Simulations”. In: *The Journal of Physical Chemistry B* 121.22 (2017), pp. 5660–5668.
- [143] Gonçalves, William, Morthomas, Julien, Chantrenne, Patrice, Perez, Michel, Foray, Geneviève, and Martin, Christophe L. “Elasticity and strength of silica aerogels: A molecular dynamics study on large volumes”. In: *Acta Materialia* 145 (2018), pp. 165–174.
- [144] Pohl, Phillip I, Faulon, Jean-Loup, and Smith, Douglas M. “Molecular dynamics computer simulations of silica aerogels”. In: *Journal of non-crystalline solids* 186 (1995), pp. 349–355.

-
- [145] Rivas Murillo, John S., Bachlechner, Martina E., Campo, Fritz A., and Barbero, Ever J. “Structure and mechanical properties of silica aerogels and xerogels modeled by molecular dynamics simulation”. In: *Journal of Non-Crystalline Solids* 356.25-27 (2010), pp. 1325–1331.
- [146] Hasmy, A., Foret, M., Pelous, J., and Jullien, R. “Small-angle neutron-scattering investigation of short-range correlations in fractal aerogels: Simulations and experiments”. In: *Phys Rev B Condens Matter* 48.13 (1993), pp. 9345–9353.
- [147] Hasmy, Anwar, Anglaret, Eric, Foret, Marie, Pelous, Jacques, and Jullien, Rémi. “Small-angle neutron-scattering investigation of long-range correlations in silica aerogels: Simulations and experiments”. In: *Physical Review B* 50.9 (1994), pp. 6006–6016.
- [148] Ma, Hang-Shing, Prévost, Jean-H., Jullien, Rémi, and Scherer, George W. “Computer simulation of mechanical structure-property”. In: *Journal of Non-Crystalline Solids* 285 (2001), pp. 216–221.
- [149] Ma, Hang-Shing, Prévost, Jean-H., and Scherer, George W. “Elasticity of DLCA model gels with loops”. In: *International Journal of Solids and Structures* 39 (2002), pp. 4605–4614.
- [150] Gelb, Lev D. “Simulating Silica Aerogels with a Coarse-Grained Flexible Model and Langevin Dynamics”. In: *The Journal of Physical Chemistry C* 111 (2007), pp. 15792–15802.
- [151] Ferreiro-Rangel, Carlos A and Gelb, Lev D. “Investigation of the bulk modulus of silica aerogel using molecular dynamics simulations of a coarse-grained model”. In: *The Journal of Physical Chemistry B* 117.23 (2013), pp. 7095–7105.
- [152] Ferreiro-Rangel, Carlos A and Gelb, Lev D. “Computational study of uniaxial deformations in silica aerogel using a coarse-grained model”. In: *The Journal of Physical Chemistry B* 119.27 (2015), pp. 8640–8650.
- [153] Lei, Jincheng and Liu, Zishun. “A novel constitutive model for the mechanical properties of silica aerogels”. In: *Journal of Applied Physics* 124.2 (2018).
- [154] Rege, Ameya and Patil, Sandeep P. “On the Molecular to Continuum Modeling of Fiber-Reinforced Composites”. In: *Advanced Theory and Simulations* 3 (2020), p. 1900211.
- [155] Kolb, M. and Herrmann, H. J. “The sol-gel transition modelled by irreversible aggregation of clusters”. In: *Journal of Physics A* 18 (1985), pp. L435–L441.

- [156] Einarsrud, Mari-Ann and Nilsen, Elin. “Strengthening of water glass and colloidal sol based silica gels by aging in TEOS”. In: *Journal of Non-Crystalline Solids* 226 (1998), pp. 122–128.
- [157] Einarsrud, M.-A. *et al.* “Strengthening of silica gels and aerogels by washing and aging processes”. In: *Journal of Non-Crystalline Solids* 285 (2001), pp. 1–7.
- [158] Meakin, Paul. “Diffusion-limited aggregation in three dimensions: Results from a new cluster-cluster aggregation model”. In: *Journal of Colloid and Interface Science* 102.2 (1984), pp. 491–504.
- [159] Wong, Joanna C.H., Kaymak, Hicret, Brunner, Samuel, and Koebel, Matthias M. “Mechanical properties of monolithic silica aerogels made from polyethoxydisiloxanes”. In: *Microporous and Mesoporous Materials* 183 (2014), pp. 23–29.
- [160] Borzęcka, Nina H, Nowak, Bartosz, Gac, Jakub M, Głaz, Tomasz, and Bojarska, Marta. “Kinetics of MTMS-based aerogel formation by the sol-gel method-experimental results and theoretical description”. In: *Journal of Non-Crystalline Solids* 547 (2020), p. 120310.
- [161] McDOWELL, R. “Influence of temperature on gel formation”. In: *Nature* 148.3765 (1941), pp. 780–781.
- [162] Ashby, MF and Gibson, LJ. “The mechanics of three-dimensional cellular materials”. In: *Proc. R. Soc. London Ser. A* 382 (1982), p. 43.
- [163] García-González, C.A., Alnaief, M., and Smirnova, I. “Polysaccharide-based aerogels—Promising biodegradable carriers for drug delivery systems”. In: *Carbohydrate Polymers* 86.4 (2011), pp. 1425–1438.
- [164] Capel, François, Nicolai, Taco, Durand, Dominique, Boulenguer, Patrick, and Langendorff, Virginie. “Calcium and acid induced gelation of (amidated) low methoxyl pectin”. In: *Food Hydrocolloids* 20.6 (2006), pp. 901–907.
- [165] Smirnova, Irina and Gurikov, Pavel. “Aerogels in chemical engineering: Strategies toward tailor-made aerogels”. In: *Annual review of chemical and biomolecular engineering* 8.1 (2017), pp. 307–334.
- [166] García-González, C.A., Jin, M., Gerth, J., Alvarez-Lorenzo, C., and Smirnova, I. “Polysaccharide-based aerogel microspheres for oral drug delivery”. In: *Carbohydrate Polymers* 117 (2015), pp. 797–806.
- [167] Schestakow, M., Muench, F., Reimuth, C., Ratke, L., and Ensinger, W. “Electroless synthesis of cellulose-metal aerogel composites”. In: *Applied Physics Letters* 108.21 (2016), p. 213108.

-
- [168] Mehling, T., Smirnova, I., Guenther, U., and Neubert, R.H.H. “Polysaccharide-based aerogels as drug carriers”. In: *Journal of Non-Crystalline Solids* 355.50 (2009), pp. 2472–2479.
 - [169] Rege, Ameya, Hillgärtner, Markus, and Itskov, Mikhail. “Mechanics of biopolymer aerogels based on microstructures generated from 2-d Voronoi tessellations”. In: *The Journal of Supercritical Fluids* 151 (2019), pp. 24–29.
 - [170] Chandrasekaran, Rajesh, Hillgärtner, Markus, Ganesan, Kathirvel, Milow, Barbara, Itskov, Mikhail, and Rege, Ameya. “Computational design of biopolymer aerogels and predictive modelling of their nanostructure and mechanical behaviour”. In: *Scientific Reports* 11.1 (2021), p. 10198.
 - [171] Chandrasekaran, Rajesh, Itskov, Mikhail, and Rege, Ameya. “Importance of geometric parameters in modeling of porous materials – a finite element study”. In: *PAMM* 23.3 (2023), e202300194.
 - [172] Williams, Jarrod C *et al.* “Highly porous, rigid-rod polyamide aerogels with superior mechanical properties and unusually high thermal conductivity”. In: *ACS Applied Materials & Interfaces* 9.2 (2017), pp. 1801–1809.
 - [173] Williams, Jarrod C, Meador, Mary Ann B, McCorkle, Linda, Mueller, Carl, and Wilmoth, Nathan. “Synthesis and properties of step-growth polyamide aerogels cross-linked with triacid chlorides”. In: *Chemistry of Materials* 26.14 (2014), pp. 4163–4171.
 - [174] Li, Mengmeng, Gan, Feng, Dong, Jie, Fang, Yuting, Zhao, Xin, and Zhang, Qinghua. “Facile Preparation of Continuous and Porous Polyimide Aerogel Fibers for Multifunctional Applications”. In: *ACS Applied Materials & Interfaces* 13.8 (2021), pp. 10416–10427.
 - [175] Moldován, Krisztián *et al.* “Mechanism of Hydration Induced Stiffening and Subsequent Plasticization of Polyamide Aerogel”. In: *Advanced Materials Interfaces* 10.17 (2023), p. 2300109.
 - [176] Guo, Haiquan *et al.* “Tailoring Properties of Cross-Linked Polyimide Aerogels for Better Moisture Resistance, Flexibility, and Strength”. In: *ACS Applied Materials & Interfaces* 4.10 (2012), pp. 5422–5429.
 - [177] Chaves, Eduardo WV. *Notes on continuum mechanics*. Springer Science & Business Media, 2013.
 - [178] Holland, Maria A. *The Hitchhiker’s Guide to Abaqus*. 2017.

A Introduction to Tensor Calculus

When I calculate and see a tiny insect that has flown on my paper then I feel something like Allah is Great and we are miserable dribblers with all our sciences glory.

A. EINSTEIN

This chapter summarizes the basic concepts of tensor algebra and analysis that form the foundation of this work. The notation used corresponds to that presented by Itskov [69]. A number of other books are recommended, including books by Bertram [67], Holzapfel [65] as well as Chaves [177].

Vectors

A vector space \mathbb{V} is defined as a set of elements that are called vectors, that satisfy the following eight axioms:

$$\text{Commutative in addition:} \quad \mathbf{x} + \mathbf{y} = \mathbf{y} + \mathbf{x}, \quad (\text{A.1})$$

$$\text{Associative in addition:} \quad \mathbf{x} + (\mathbf{y} + \mathbf{z}) = (\mathbf{x} + \mathbf{y}) + \mathbf{z}, \quad (\text{A.2})$$

$$\text{Zero element:} \quad \mathbf{x} + \mathbf{0} = \mathbf{0} + \mathbf{x} = \mathbf{x}, \quad (\text{A.3})$$

$$\text{Inverse element:} \quad \mathbf{x} + (-\mathbf{x}) = \mathbf{0}, \quad (\text{A.4})$$

$$\text{Associative in scalar multiplication:} \quad \alpha(\beta\mathbf{x}) = (\alpha\beta)\mathbf{x}, \quad (\text{A.5})$$

$$\text{Unit element of scalar multiplication:} \quad 1\mathbf{x} = \mathbf{x}, \quad (\text{A.6})$$

$$\text{Distributive in vector addition:} \quad \alpha(\mathbf{x} + \mathbf{y}) = \alpha\mathbf{x} + \alpha\mathbf{y}, \quad (\text{A.7})$$

$$\text{Distributive in scalar addition:} \quad (\alpha + \beta)\mathbf{x} = \alpha\mathbf{x} + \beta\mathbf{x}, \quad (\text{A.8})$$

where \mathbf{x} , \mathbf{y} and $\mathbf{0}$ are vectors of the given vector space \mathbb{V} and α , β and 1 are scalar real numbers.

An essential definition is that of linearly dependent vectors. A set of vectors $\{\mathbf{x}_1, \mathbf{x}_2, \dots, \mathbf{x}_n\}$ is said to be linearly dependent if there exists a set of real scalars $\{\alpha_1, \alpha_2, \dots, \alpha_n\}$ that are not all zero, such that

$$\sum_{i=1}^n \alpha_i \mathbf{x}_i = \mathbf{0}. \quad (\text{A.9})$$

Otherwise, the vectors $\{\mathbf{x}_1, \mathbf{x}_2, \dots, \mathbf{x}_n\}$ are said to be linearly independent. Any set of n linearly independent vectors $\mathcal{G} = \{\mathbf{g}_1, \mathbf{g}_2, \dots, \mathbf{g}_n\}$ in a n -

n -dimensional vector space \mathbb{V}^n can be combined linearly to form any vector in \mathbb{V}^n . This set is also called a basis $\mathcal{G} \subset \mathbb{V}^n$. Thus, any arbitrary vector \mathbf{x} can be expressed through the vectors $\{\mathbf{g}_1, \mathbf{g}_2, \dots, \mathbf{g}_n\}$ with

$$\mathbf{x} = \sum_{i=1}^n x^i \mathbf{g}_i = x^i \mathbf{g}_i, \quad \forall \mathbf{x} \in \mathbb{V}^n, \quad (\text{A.10})$$

where the Einstein summation convention is used.

The scalar product $\mathbf{x} \cdot \mathbf{y}$ is defined as a real-valued function between the two vectors \mathbf{x} and \mathbf{y} satisfying the following four conditions:

$$\text{Commutative:} \quad \mathbf{x} \cdot \mathbf{y} = \mathbf{y} \cdot \mathbf{x}, \quad (\text{A.11})$$

$$\text{Distributive in vector addition:} \quad \mathbf{x} \cdot (\mathbf{y} + \mathbf{z}) = \mathbf{x} \cdot \mathbf{z} + \mathbf{y} \cdot \mathbf{z}, \quad (\text{A.12})$$

$$\text{Associative in scalar multiplication:} \quad (\alpha \mathbf{x}) \cdot \mathbf{y} = \alpha(\mathbf{x} \cdot \mathbf{y}), \quad (\text{A.13})$$

$$\text{Positive-definite:} \quad \mathbf{x} \cdot \mathbf{x} \geq 0, \quad \mathbf{x} \cdot \mathbf{x} = 0 \text{ iff. } \mathbf{x} = \mathbf{0}. \quad (\text{A.14})$$

An n -dimensional vector space given these properties by the scalar product is called the Euclidean space \mathbb{E}^n . Thus, it is possible to define a norm of the vector \mathbf{x} with

$$\|\mathbf{x}\| = \sqrt{\mathbf{x} \cdot \mathbf{x}}. \quad (\text{A.15})$$

For a given basis $\mathcal{G} = \{\mathbf{g}_1, \mathbf{g}_2, \dots, \mathbf{g}_n\}$ in the n -dimensional Euclidean space, a basis $\mathcal{G}' = \{\mathbf{g}^1, \mathbf{g}^2, \dots, \mathbf{g}^n\}$ is referred to as dual if

$$\mathbf{g}_i \cdot \mathbf{g}^j = \delta_i^j, \quad i, j = 1, \dots, n, \quad (\text{A.16})$$

where δ_i^j is the Kronecker delta defined by

$$\delta_{ij} = \delta^{ij} = \delta_j^i = \delta_i^j = \begin{cases} 1 & \text{for } i = j \\ 0 & \text{for } i \neq j \end{cases}. \quad (\text{A.17})$$

It is possible to transform a basis \mathcal{G} into a basis \mathcal{G}' using the metric coefficients with

$$\mathbf{g}^i = g^{ij} \mathbf{g}_j \quad \text{or} \quad \mathbf{g}_i = g_{ij} \mathbf{g}^j, \quad \text{with} \quad g^{ij} = \mathbf{g}^i \cdot \mathbf{g}^j \quad \text{and} \quad g_{ij} = \mathbf{g}_i \cdot \mathbf{g}_j. \quad (\text{A.18})$$

Second Order Tensors

A second order tensor is defined as a linearly mapping between a vector \mathbf{x} and \mathbf{y} with

$$\mathbf{y} = \mathbf{A} \mathbf{x}, \quad \mathbf{A} \in \text{Lin}^n, \quad \mathbf{x}, \mathbf{y} \in \mathbb{E}^n, \quad (\text{A.19})$$

where \mathbf{A} is a second order tensor and \mathbf{Lin}^n are all possible linear mappings of one vector into another in Euclidean space \mathbb{E}^n . Here, the linearity is given through the distributive rule and the associative rule for the multiplication by a scalar with

$$\mathbf{A}(\mathbf{x} + \mathbf{y}) = \mathbf{A}\mathbf{x} + \mathbf{A}\mathbf{y}, \quad \forall \mathbf{x}, \mathbf{y} \in \mathbb{E}^n, \quad \forall \mathbf{A} \in \mathbf{Lin}^n, \quad (\text{A.20})$$

$$\mathbf{A}(\alpha \mathbf{x}) = \alpha(\mathbf{A}\mathbf{x}), \quad \forall \mathbf{x} \in \mathbb{E}^n, \quad \forall \mathbf{A} \in \mathbf{Lin}^n, \quad \forall \alpha \in \mathbb{R}. \quad (\text{A.21})$$

As for the axioms for vectors, a zero tensor $\mathbf{0}$, the identity tensor \mathbf{I} as well as the inverse element need to be defined with

$$\mathbf{I}\mathbf{x} = \mathbf{x}, \quad (\text{A.22})$$

$$\mathbf{0}\mathbf{x} = \mathbf{0}, \quad (\text{A.23})$$

$$\mathbf{A} + (-\mathbf{A}) = \mathbf{0}, \quad \forall \mathbf{x} \in \mathbb{E}^n, \quad \forall \mathbf{A} \in \mathbf{Lin}^n. \quad (\text{A.24})$$

Furthermore, it is possible to define the tensor product which can be used to construct a second-order tensor from two vectors \mathbf{a} and \mathbf{b} with

$$\mathbf{A} = \mathbf{a} \otimes \mathbf{b}, \quad \forall \mathbf{a}, \mathbf{b} \in \mathbb{E}^n, \quad \mathbf{A} \in \mathbf{Lin}^n, \quad (\text{A.25})$$

where the product is expressed through the symbol " \otimes ". Following properties need to be fulfilled:

$$(\mathbf{a} \otimes \mathbf{b})\mathbf{x} = \mathbf{a}(\mathbf{b} \cdot \mathbf{x}), \quad (\text{A.26})$$

$$\mathbf{a} \otimes \mathbf{b} \neq \mathbf{b} \otimes \mathbf{a}, \quad (\text{A.27})$$

$$\mathbf{x} \otimes (\mathbf{b} + \mathbf{a}) = \mathbf{x} \otimes \mathbf{b} + \mathbf{x} \otimes \mathbf{a}, \quad (\text{A.28})$$

$$(\alpha \mathbf{a}) \otimes \mathbf{b} = \mathbf{a} \otimes (\alpha \mathbf{b}). \quad (\text{A.29})$$

If the linear mapping $\mathbf{y} = \mathbf{A}\mathbf{x}$ is given, then a tensor is called invertible if there exists the inverse tensor $\mathbf{A}^{-1} \in \mathbf{Lin}^n$ such that

$$\mathbf{x} = \mathbf{A}^{-1}\mathbf{y} \quad \forall \mathbf{x} \in \mathbb{E}^n. \quad (\text{A.30})$$

The transpose tensor \mathbf{A}^T can be defined by

$$\mathbf{A}^T \mathbf{x} = \mathbf{x} \mathbf{A}. \quad (\text{A.31})$$

Fourth Order Tensors

It is possible to linearly map a second order \mathbf{A} into another second order tensor \mathbf{B} using the following mapping

$$\mathbf{B} = \mathbf{C} : \mathbf{A} \quad \mathbf{C} \in \mathbf{Lin}^n, \mathbf{X}, \mathbf{Y} \in \mathbf{Lin}^n, \quad (\text{A.32})$$

where \mathbb{C} is a fourth-order tensor and \mathbf{Lin}^n denotes all possible linear mappings of a second order tensor into another second order tensor in \mathbf{Lin}^n . The linearity of this mapping is given by

$$\mathbb{C} : (\mathbf{A} + \mathbf{B}) = \mathbb{C} : \mathbf{A} + \mathbb{C} : \mathbf{B}, \quad \forall \mathbf{A}, \mathbf{B} \in \mathbf{Lin}^n, \forall \mathbb{C} \in \mathbf{Lin}^n, \quad (\text{A.33})$$

$$\mathbb{C} : (\alpha \mathbf{X}) = \alpha (\mathbb{C} : \mathbf{X}), \quad \forall \alpha \in \mathbb{R}, \forall \mathbf{X} \in \mathbf{Lin}^n, \forall \mathbb{C} \in \mathbf{Lin}^n. \quad (\text{A.34})$$

The same axiomatic framework that applies to second-order tensors also applies to fourth-order tensors. Additionally, it is possible to define using the zero tensor \mathbf{O} and the identity tensor \mathbf{I} following rules:

$$\mathbf{I} : \mathbf{A} = \mathbf{A}, \quad (\text{A.35})$$

$$\mathbf{O} : \mathbf{A} = \mathbf{0}, \quad (\text{A.36})$$

$$\mathbf{A} + \mathbf{O} = \mathbf{A}, \quad \forall \mathbf{A} \in \mathbf{Lin}^n, \forall \mathbf{A} \in \mathbf{Lin}^n. \quad (\text{A.37})$$

Tensor Analysis

If a scalar-valued tensor function $f(\mathbf{A}) : \mathbf{Lin}^n \mapsto \mathbb{R}$ is given, it is differentiable in a neighborhood of \mathbf{A} if there exists a tensor $f(\mathbf{A})_{,\mathbf{A}} \in \mathbf{Lin}^n$, which fulfills

$$\left. \frac{d}{dt} f(\mathbf{A} + t\mathbf{X}) \right|_{t=0} = f(\mathbf{A})_{,\mathbf{A}} : \mathbf{X}, \quad \forall \mathbf{A} \in \mathbf{Lin}^n, \quad (\text{A.38})$$

where $f(\mathbf{A})_{,\mathbf{A}}$ is called the derivative of $f(\mathbf{A})$. An explicit representation in terms of a given basis can be derived as follows:

$$f(\mathbf{A})_{,\mathbf{A}} = \frac{\partial f}{\partial A_{ij}} \mathbf{g}_i \otimes \mathbf{g}_j = \frac{\partial f}{\partial A^{ij}} \mathbf{g}^i \otimes \mathbf{g}^j = \frac{\partial f}{\partial A_i^j} \mathbf{g}_i \otimes \mathbf{g}^j = \frac{\partial f}{\partial A_j^i} \mathbf{g}^i \otimes \mathbf{g}_j. \quad (\text{A.39})$$

The aforementioned formula can be utilized to derive the derivatives of tensor powers of traces, as expressed by the following equation:

$$\left(\text{tr } \mathbf{A}^k \right)_{,\mathbf{A}} = k \left(\mathbf{A}^{k-1} \right)^T. \quad (\text{A.40})$$

As the invariants of a second-order tensor $\mathbf{A} \in \mathbf{Lin}^3$ can be expressed in terms of traces, this in turn allows us to derive the derivatives of the invariants with respect to this tensor $\mathbf{A} \in \mathbf{Lin}^3$ by

$$(\text{I}_{\mathbf{A}})_{,\mathbf{A}} = \mathbf{I}, \quad (\text{II}_{\mathbf{A}})_{,\mathbf{A}} = \text{II}_{\mathbf{A}} \mathbf{I} - \mathbf{A}^T, \quad (\text{III}_{\mathbf{A}})_{,\mathbf{A}} = \text{III}_{\mathbf{A}} \mathbf{A}^{-T}. \quad (\text{A.41})$$

B Foundations of Continuum Mechanics

Whoever follows a path to seek knowledge, Allah will make the path to Jannah easy for them.

PROPHET MUHAMMAD ﷺ

In order to describe the relationship between material points and their time-dependent positions in space, it is essential to have a comprehensive understanding of the kinematic relations. To comprehend the manner in which motion and deformation give rise to interactions within the material, it is necessary to define the concept of stress. Moreover, it is essential to introduce the principles of balance, including the conservation of mass, momentum balance principles, and energy balance. These principles are universally applicable to any material and must be satisfied at all times. This section is primarily based on [65, 67, 69]. As the reader is presumed to possess a fundamental understanding of the aforementioned topics, comprehensive explanations will be omitted.

General Principles

The fundamental principles of kinematics and balance laws, as outlined in Appendix B, provide a comprehensive framework for understanding the arbitrary deformation of bodies within a universal context, irrespective of the specific material properties involved. However, it is crucial to integrate the effects of diverse material behavior into the existing theory. Accordingly, it is essential to establish constitutive equations (also referred to as material equations, material laws, functionals, or material models) that describe the various effects that influence material behavior. The objective of material theory is to identify common properties that are applicable to a range of materials, to develop general material equations, and to classify materials according to their characteristics. It is therefore possible to assume certain underlying principles that have been derived from experience, plausibility principles, and experimental investigations. These principles are frequently referred to as Noll's axioms [63]. This section provides a summary of the ideas

behind these general principles and builds on the discussions presented in [65–67].

Principle of Stress Determinism

In the field of mechanics, it is commonly accepted that a deterministic relationship exists between the stresses experienced by a body and the manner in which it moves. This assumption can be expressed in the *principle of determinism for the stress*, which states that the stresses that a material point is subjected to at a given moment depend on the motion of the body up to that moment, including both its present state and its past history, but not on any future motion. The earliest known reference to this principle can be attributed to Cauchy [63].

Principle of Local Action

Moreover, it has been empirically demonstrated that the stresses at a given material point are independent of the motion of other points, particularly if these points are sufficiently distant. This assumption can be expressed by the *principle of local action*, which states that the stresses at a point in the material are influenced only by the motion that occurs within a finite environment surrounding that point.

Principle of Material Objectivity

The *principle of material objectivity* states that observers in relative motion with respect to a given body should observe the same material properties and the same constitutive laws. This implies that the constitutive law remains unaltered in any reference frame and is not affected by EUCLIDEAN transformations. In general, a significant number of physical quantities are not indifferent to the observer. In consequence, these quantities are unsuitable for the formulation of material laws, as evidenced by a comparison of a physical quantity such as the deformation gradient in both frames. Accordingly, we consider a novel observer in motion and rotation relative to an initial observer whose observations were utilized to characterize the deforming body. In comparison to the original observer, the new observer experiences the rigid body motion as

$$\mathbf{x}^* = \mathbf{c}(t) + \mathbf{Q}(t)\mathbf{x}, \quad (\text{B.1})$$

where \mathbf{x} is the position in the current configuration for the initial observer, $\mathbf{c}(t)$ is the arbitrary time-dependent translational displacement, $\mathbf{Q}(t) \in \mathbf{Sorth}^3$ is a proper orthogonal tensor and \mathbf{x}^* is the position in the current configuration of the new observer. Using this relation the deformation gradient can be

determined with

$$\mathbf{F}^* = \frac{\partial \mathbf{x}^*}{\partial \mathbf{X}} = \frac{\partial \mathbf{x}^*}{\partial \mathbf{x}} \frac{\partial \mathbf{x}}{\partial \mathbf{X}} = \mathbf{QF}, \quad (\text{B.2})$$

where \mathbf{X} is the reference configuration. This comparison can also be done e.g. the relative volume change J , the right Cauchy-Green tensor \mathbf{C} or the stress power $\ell = \boldsymbol{\sigma} : \mathbf{d}$ which leads to

$$J^* = J, \quad \mathbf{C}^* = \mathbf{C} \quad \text{and} \quad \ell^* = \boldsymbol{\sigma}^* : \mathbf{d}^* = \boldsymbol{\sigma} : \mathbf{d} = \ell. \quad (\text{B.3})$$

It can be demonstrated that Lagrangian or material tensor and scalar fields are observer-independent, exhibiting no changes between different reference frames. Consequently, they are classified as objective or material frame-indifferent.

Kinematics

A body \mathcal{B}_0 is considered in the reference placement at time t_0 as depicted in Figure B.1. An arbitrary point P can be described by the position \mathbf{X} in the

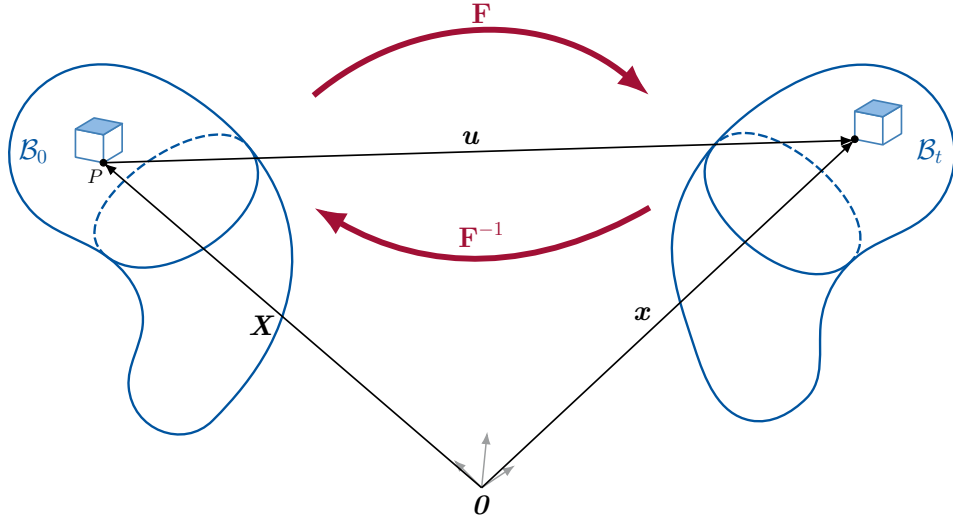


Fig. B.1: Mapping between reference \mathbf{X} and current configuration \mathbf{x} of a body \mathcal{B} .

reference configuration. After a time t , the body \mathcal{B}_t has changed its position and the placement of the same point P is $\mathbf{x}(\mathbf{X}, t) = \boldsymbol{\chi}(\mathbf{X}, t)$, where $\boldsymbol{\chi}(\mathbf{X}, t)$ represents the motion mapping. It is also possible to define a mapping \mathbf{u} describing the displacement between the position of a material point in the current and in the reference placement. Mathematically, this is done by

$$\mathbf{u}(\mathbf{X}, t) = \boldsymbol{\chi}(\mathbf{X}, t) - \mathbf{X} = \mathbf{x}(\mathbf{X}, t) - \mathbf{X}. \quad (\text{B.4})$$

The fields on \mathcal{B}_t are described by the Eulerian description (also known as or spatial description). The gradient with respect to the Lagrangian variables of the mapping χ and the displacement \mathbf{u} are defined by:

$$\mathbf{F} = \text{Grad}(\chi(\mathbf{X}, t)) = \frac{\partial \chi(\mathbf{X}, t)}{\partial \mathbf{X}} \quad (\text{B.5})$$

where \mathbf{F} is known as the deformation gradient. It is also possible to define the displacement gradient \mathbf{H} given by

$$\mathbf{H} = \text{Grad}(\mathbf{u}(\mathbf{X}, t)) = \frac{\partial \mathbf{u}(\mathbf{X}, t)}{\partial \mathbf{X}} = \mathbf{F} + \mathbf{1} . \quad (\text{B.6})$$

Since it is assumed that \mathbf{F} is invertible, the deformation gradient can multiplicatively decomposed into

$$\mathbf{F} = \mathbf{R}\mathbf{U} = \mathbf{V}\mathbf{R} . \quad (\text{B.7})$$

This is a polar decomposition with the rotation tensor \mathbf{R} , the right and left stretch tensors \mathbf{U} and \mathbf{V} , respectively. It should be noted that both tensors are positive-definite and symmetric. Furthermore, it is possible to define the right and left Cauchy-Green tensors \mathbf{C} and \mathbf{b}

$$\mathbf{C} = \mathbf{F}^T \mathbf{F} = \mathbf{U}^2 \quad \text{and} \quad \mathbf{b} = \mathbf{F} \mathbf{F}^T = \mathbf{V}^2 . \quad (\text{B.8})$$

Furthermore, it is possible to define the Green strain tensor with

$$\mathbf{E}_G := \frac{1}{2}(\mathbf{C} - \mathbf{1}) = \frac{1}{2}(\mathbf{F}^T \mathbf{F} - \mathbf{1}) . \quad (\text{B.9})$$

Stress Measures

If the body \mathcal{B}_t in its current configuration is subjected to external forces, it can be divided into two distinct parts by introducing a smooth surface passing through point P , see Figure B.2. The surface area surrounding point P is denoted as ΔA , with \mathbf{n} representing the outward normal unit vector, $\Delta \mathbf{f}$ a force and $\Delta \mathbf{m}$ a couple. The Cauchy stress vector \mathbf{t} , also known as the traction vector, can be defined as follows:

$$\mathbf{t} = \lim_{\Delta A \rightarrow 0} \frac{\Delta \mathbf{f}}{\Delta A} . \quad (\text{B.10})$$

It is additionally postulated that for the couple that

$$\lim_{\Delta A \rightarrow 0} \frac{\Delta \mathbf{m}}{\Delta A} = \mathbf{0} . \quad (\text{B.11})$$

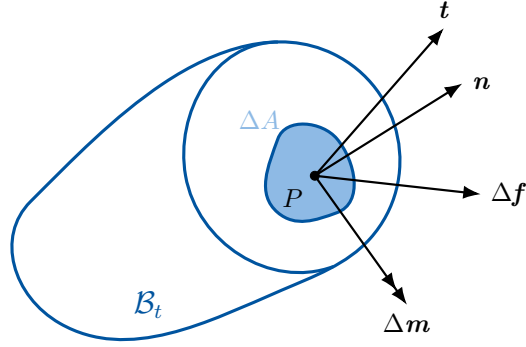


Fig. B.2: Visualization of cutting face through point P of body \mathcal{B}_t with the Cauchy stress vector \mathbf{t} , force vector $\Delta \mathbf{f}$, outward normal unit vector \mathbf{n} , couple $\Delta \mathbf{m}$ and surface area ΔA .

The Cauchy stress vector \mathbf{t} is dependent on the selected surface exclusively through the outward-pointing unit normal \mathbf{n} . The Cauchy theorem establishes a relationship between these quantities, which is expressed through the following linear mapping:

$$\mathbf{t} = \boldsymbol{\sigma} \mathbf{n}, \quad (\text{B.12})$$

where $\boldsymbol{\sigma}$ is the Cauchy stress tensor. This stress tensor is also referred to as the true stress, as it is defined with respect to the surface of the body in its current configuration. Nevertheless, for a multitude of engineering applications, it is beneficial to define stress in relation to the reference configuration. Accordingly, the first Piola-Kirchhoff stress tensor, also designated as the engineering stress or nominal stress, is given by

$$\mathbf{P} = J \boldsymbol{\sigma} \mathbf{F}^{-\text{T}}. \quad (\text{B.13})$$

It should be noted that the first Piola-Kirchhoff stress tensor is not symmetric. A variety of other stress tensors can be defined, including the second Piola-Kirchhoff stress tensor \mathbf{S} and the Kirchhoff stress tensor $\boldsymbol{\tau}$. These can be defined through the following relationships:

$$\mathbf{S} = \mathbf{F}^{-1} \mathbf{P} \quad \text{and} \quad \boldsymbol{\tau} = J \boldsymbol{\sigma}. \quad (\text{B.14})$$

Tangent Tensor

For numerical simulations employing the finite element method, it is crucial to compute a tangent tensor. A variety of different tangent tensors exist. The material tangent tensor \mathbf{C} can be formulated as the derivative of the second Piola-Kirchhoff stress or directly as the second-order derivative of the strain

energy function with respect to the right Cauchy-Green tensor \mathbf{C} with

$$\mathbb{C} = 4 \frac{\partial^2 \Psi(\mathbf{C})}{\partial \mathbf{C}^2} = 2 \frac{\partial \mathbf{S}}{\partial \mathbf{C}} = 2 \frac{\partial \bar{\mathbf{S}}}{\partial \mathbf{C}} + 2 \frac{\partial \hat{\mathbf{S}}}{\partial \mathbf{C}} = \bar{\mathbb{C}} + \hat{\mathbb{C}}. \quad (\text{B.15})$$

The material tangent tensor \mathbb{C} can further be decomposed into an isochoric contribution $\bar{\mathbb{C}}$ and a volumetric contribution $\hat{\mathbb{C}}$. The isochoric part $\bar{\mathbb{C}}$ can be determined by

$$\begin{aligned} \bar{\mathbb{C}} = \bar{\mathbb{P}}^T : \left(4 \frac{\partial^2 \bar{\Psi}(\bar{\mathbf{C}})}{\partial \bar{\mathbf{C}}^2} \right) : \bar{\mathbb{P}}^T + \frac{2}{3} (\bar{\mathbf{S}} : \bar{\mathbf{C}}) \bar{\mathbb{P}} \\ - \frac{2}{3} J^{-2/3} (\bar{\mathbf{S}} \odot \mathbf{C}^{-1} + \mathbf{C}^{-1} \odot \bar{\mathbf{S}}), \end{aligned} \quad (\text{B.16})$$

where the projection tensor $\tilde{\mathbb{P}}$ is given by

$$\tilde{\mathbb{P}} = (\mathbf{C}^{-1} \otimes \mathbf{C}^{-1})^S + \frac{1}{3} \mathbf{C}^{-1} \odot \mathbf{C}^{-1}. \quad (\text{B.17})$$

Moreover, it is possible to derive the second derivative of the strain energy function with respect to the isochoric contribution $\bar{\mathbf{C}}$ as follows:

$$\frac{\partial^2 \bar{\Psi}(\bar{\mathbf{C}})}{\partial \bar{\mathbf{C}}^2} = \frac{\partial \tilde{\mathbf{S}}}{\partial \bar{\mathbf{C}}} = \alpha_1 \mathbf{C} \odot \bar{\mathbf{C}} + \alpha_2 (\mathbf{C} \odot \mathbf{I} + \mathbf{I} \odot \bar{\mathbf{C}}) + \alpha_3 \mathbb{J} + \alpha_4 \mathbf{I} \odot \mathbf{I}, \quad (\text{B.18})$$

where \mathbb{J} is the fourth-order identity tensor and the coefficients α_1 , α_2 , α_3 and α_4 are given with

$$\alpha_1 = 2 \frac{\partial^2 \bar{\Psi}}{\partial \Pi_{\bar{\mathbf{C}}}^2}, \quad \alpha_2 = -2 \left(\frac{\partial^2 \bar{\Psi}}{\partial \mathbf{I}_{\bar{\mathbf{C}}} \partial \Pi_{\bar{\mathbf{C}}}} + \mathbf{I}_{\bar{\mathbf{C}}} \frac{\partial^2 \bar{\Psi}}{\partial \Pi_{\bar{\mathbf{C}}}^2} \right), \quad (\text{B.19})$$

$$\alpha_3 = -2 \frac{\partial \bar{\Psi}}{\partial \Pi_{\bar{\mathbf{C}}}}, \quad \alpha_4 = 2 \left(\frac{\partial^2 \bar{\Psi}}{\partial \mathbf{I}_{\bar{\mathbf{C}}}^2} + 2 \mathbf{I}_{\bar{\mathbf{C}}} \frac{\partial^2 \bar{\Psi}}{\partial \mathbf{I}_{\bar{\mathbf{C}}} \partial \Pi_{\bar{\mathbf{C}}}} + \frac{\partial \bar{\Psi}}{\partial \Pi_{\bar{\mathbf{C}}}} + \mathbf{I}_{\bar{\mathbf{C}}}^2 \frac{\partial^2 \bar{\Psi}}{\partial \Pi_{\bar{\mathbf{C}}}^2} \right). \quad (\text{B.20})$$

The volumetric part $\hat{\mathbb{C}}$ can be calculated using the following formula:

$$\hat{\mathbb{C}} = \left(J^2 \frac{d^2 U}{dJ^2} + J \frac{dU}{dJ} \right) \mathbf{C}^{-1} \odot \mathbf{C}^{-1} - 2J \frac{dU}{dJ} (\mathbf{C}^{-1} \otimes \mathbf{C}^{-1})^S. \quad (\text{B.21})$$

In the context of FE applications, it is essential to provide the spatial tangent tensor. This tensor can be obtained through a push-forward operation given with

$$_{ijkl} = \frac{1}{J} \mathbf{C}_{IJKL} \mathbf{F}_{iI} \mathbf{F}_{jJ} \mathbf{F}_{kK} \mathbf{F}_{lL}. \quad (\text{B.22})$$

In the case of ABAQUS, the tangent tensor relates the volume-normalized Jaumann rate of the Kirchhoff stress to the symmetric rate of the deformation

tensor, see [178] for further details. The ABAQUS tangent Abq is given with

$$\text{Abq} = {}_{ijkl} + {}'_{ijkl}. \quad (\text{B.23})$$

Here, the fourth-order tensor $'_{ijkl}$, also known as the geometric tangent, can be reduced to purely kinematic terms, given by

$$'_{ijkl} = \frac{1}{2} (\delta_{ik} \boldsymbol{\sigma}_{jl} + \delta_{il} \boldsymbol{\sigma}_{jk} + \delta_{jk} \boldsymbol{\sigma}_{il} + \delta_{jl} \boldsymbol{\sigma}_{ik}), \quad (\text{B.24})$$

where δ_{ij} is the Kronecker delta.

Balance Laws

Based on [66], all fundamental balance laws can be encapsulated within a master balance principle in the global formulation, expressed as follows:

$$\frac{d}{dt} \int_{\mathcal{P}_t} \psi \, dv = \int_{\partial \mathcal{P}_t} \Phi_\psi \mathbf{n} \, da + \int_{\mathcal{P}_t} \sigma_\psi \, dv. \quad (\text{B.25})$$

Here, \mathcal{P} denotes any bounded regular subregion of the body \mathcal{B} , with \mathcal{P}_t representing its current configuration. The vector \mathbf{n} is the outward unit normal to the boundary of the region \mathcal{P}_t . The quantities ψ and σ_ψ are given as tensor fields of order m , while Φ_ψ is a tensor field of order $m + 1$. For instance, if $m = 0$, then ψ is a scalar quantity and Φ_ψ is a vector quantity. If $m = 1$, then ψ is a vector quantity and Φ_ψ is a second-order tensor. A comprehensive list of potential quantities for ψ , Φ_ψ and σ_ψ relevant to the balance laws of mass, linear momentum, angular momentum, and energy are provided in Table B.1. Note that for this representation an additional exterior product between \mathbf{x} and \mathbf{y} , is defined given by

$$\mathbf{x} \wedge \mathbf{y} = \mathbf{x} \otimes \mathbf{y} + \mathbf{y} \otimes \mathbf{x}. \quad (\text{B.26})$$

In the given table the quantity ρ is the mass density in the current configuration, \mathbf{b} is the body force density, \mathbf{x}_o is a specific reference location for the momentum, ε is the specific internal energy density, \mathbf{q} is the heat flux vector, and r is the energy supply density.

The local forms of the integral balance can also be determined at a point within the region \mathcal{B}_t . The derivation of these local forms relies on specific assumptions regarding the smoothness of the tensor fields ψ , Φ_ψ , and σ_ψ . This analysis encompasses both regular points, where all tensor fields are smooth, and singular points, where they may exhibit jump discontinuities. At a regular

point \mathbf{x} , the general balance equation in Equation B.25 simplifies to:

$$\frac{\partial \psi}{\partial t} + \operatorname{div}(\psi \otimes \dot{\mathbf{x}} - \Phi_\psi) - \sigma_\psi = 0 \quad (\text{B.27})$$

In this context, the term $\psi \otimes \dot{\mathbf{x}}$ is referred to as the convective flux of ψ . When ψ is a scalar quantity, this notation should be interpreted as $\psi \dot{\mathbf{x}}$.

Tab. B.1: List of quantities for ψ , Φ_ψ and σ_ψ relevant to the balance equations of mass, linear momentum, angular momentum, and energy.

Balance Law	ψ	Φ_ψ	σ_ψ
Mass	ρ	0	0
Linear Momentum	$\rho \dot{\mathbf{x}}$	$\boldsymbol{\sigma}$	$\rho \mathbf{b}$
Angular Momentum	$(\mathbf{x} - \mathbf{x}_o) \wedge \rho \dot{\mathbf{x}}$	$(\mathbf{x} - \mathbf{x}_o) \wedge \boldsymbol{\sigma}$	$(\mathbf{x} - \mathbf{x}_o) \wedge \rho \mathbf{b}$
Energy	$\rho \varepsilon + \frac{1}{2} \rho \dot{\mathbf{x}} \cdot \dot{\mathbf{x}}$	$-\mathbf{q} + \boldsymbol{\sigma} \dot{\mathbf{x}}$	$\rho r + \rho \dot{\mathbf{x}} \cdot \mathbf{b}$